National Library of Canada
Bibliothèque nationale du Canada

Canadian Theses Service
Service des thèses canadiennes

Ottawa, Canada
K1A 0N4

NOTICE

The quality of this microform is heavily dependent upon the quality of the original thesis submitted for microfilming. Every effort has been made to ensure the highest quality of reproduction possible.

If pages are missing, contact the university which granted the degree.

Some pages may have indistinct print especially if the original pages were typed with a poor typewriter ribbon or if the university sent us an inferior photocopy.

Previously copyrighted materials (journal articles, published tests, etc.) are not filmed.

Reproduction in full or in part of this microform is governed by the Canadian Copyright Act, R.S.C. 1970, c. C-30.

AVIS

La qualité de cette microforme dépend grandement de la qualité de la thèse soumise au microfilmage. Nous avons tout fait pour assurer une qualité supérieure de reproduction.

S'il manque des pages, veuillez communiquer avec l'université qui a conféré le grade.

La qualité d'impression de certaines pages peut laisser à désirer, surtout si les pages originales ont été dactylographiées à l'aide d'un ruban usé ou si l'université nous a fait parvenir une photocopie de qualité inférieure.

Les documents qui font déjà l'objet d'un droit d'auteur (articles de revue, tests publiés, etc.) ne sont pas microfilmés.

La reproduction, même partielle, de cette microforme est soumise à la Loi canadienne sur le droit d'auteur, SRC 1970, c. C-30.

NL-339 (r. 88/04)

Canada

THE UNIVERSITY OF ALBERTA

ATOMIC LIFETIME MEASUREMENTS USING THE BEAM-LASER TECHNIQUE

BY

ROBERT NELSON GOSSELIN

A THESIS

SUBMITTED TO THE FACULTY OF GRADUATE STUDIES AND RESEARCH IN PARTIAL FULFILMENT OF THE REQUIREMENTS FOR THE DEGREE OF DOCTOR OF PHILOSOPHY

IN

ASTROPHYSICS

DEPARTMENT OF PHYSICS

EDMONTON, ALBERTA

SPRING 1988

Permission has been granted to the National Library of Canada to microfilm this thesis and to lend or sell copies of the film.

The author (copyright owner) has reserved other publication rights, and neither the thesis nor extensive extracts from it may be printed or otherwise reproduced without his/her written permission.

L'autorisation a été accordée à la Bibliothèque nationale du Canada de microfilmer cette thèse et de prêter ou de vendre des exemplaires du film.

L'auteur (titulaire du droit d'auteur) se réserve les autres droits de publication; ni la thèse ni de longs extraits de celle-ci ne doivent être imprimés ou autrement reproduits sans son autorisation écrite.

ISBN 0-315-42763-9

THE UNIVERSITY OF ALBERTA

RELEASE FORM

NAME OF AUTHOR: **ROBERT NELSON GOSSELIN**

TITLE OF THESIS: **ATOMIC LIFETIME MEASUREMENTS USING THE BEAM-LASER TECHNIQUE**

DEGREE: **DOCTOR OF PHILOSOPHY**

YEAR THIS DEGREE GRANTED: **1988**

Permission is hereby granted to THE UNIVERSITY OF ALBERTA LIBRARY to reproduce single copies of this thesis and to lend or sell such copies for private, scholarly or scientific research purposes only.

The author reserves other publication rights, and neither the thesis nor extensive extracts from it may be printed or otherwise reproduced without the author's written permission.

Robert Gosselin

(Student's signature)

Physics Department

University of Alberta

Edmonton, Alberta T6G 2J1

(Student's permanent address)

Date: April 11, 1988

THE UNIVERSITY OF ALBERTA

FACULTY OF GRADUATE STUDIES AND RESEARCH

The undersigned certify that they have read, and recommend to the Faculty of Graduate Studies and Research for acceptance, a thesis entitled ATOMIC LIFETIME MEASUREMENTS USING THE BEAM-LASER TECHNIQUE submitted by ROBERT NELSON GOSSELIN in partial fulfilment of the requirements for the degree of DOCTOR OF PHILOSOPHY in PHYSICS (ASTROPHYSICS).

E.H. Pinnington

Dr. E.H. Pinnington (Supervisor)

Dr. H.G. Berry

Robert Fedosejevs

Dr. R. Fedosejevs

Frank L. Weichman

Dr. F.L. Weichman

J.A. Kernahan

Dr. J.A. Kernahan

Date: April 11, 1988

FOR DOROTHY AND ADRIAN

ABSTRACT

The beam-laser technique is used to obtain cascade-free lifetimes for levels in singly-ionized titanium, calcium and sodium. The estimated uncertainties in the lifetimes obtained are between 1 and 1.5%. The essence of this technique is to selectively excite the level of interest by crossing a fast ion-beam with a laser beam of the appropriate wavelength. In the present work, high-power excimer and excimer-pumped dye lasers are used to populate the levels of interest. These experiments demonstrate some possible variations of the beam laser method. In particular, the sodium experiment involves a two-stage excitation process, utilizing a gas cell to populate a metastable level before the laser excitation. The target chamber used in the experiments has been designed so as to minimize scattered laser-light. The effects of systematic errors due to fluctuations in laser power, Zeeman quantum beats, zero-field quantum beats, collisional de-excitation, single-photon counting saturation correction and ion-beam path/detection system misalignment are discussed. The results of these experiments are compared with previous experiments and theory.

ACKNOWLEDGEMENTS

I would like to thank my supervisor, Dr. Eric Pinnington for his help and guidance during my years as a graduate student. I would also like to thank Dr. Will Ansbacher for both his technical assistance in setting up the experiments and the many helpful discussions about various aspects of the experiments. My thanks to Ron Gardner and Larry Coulson of the Radiation Research Laboratory for teaching me the basics of TEX, AUTOCAD and GRAPHER, the computer programs used to typeset the text and equations, draw the figures and plot the graphs presented in this thesis.

TABLE OF CONTENTS

CHAPTER ONE: INTRODUCTION 1
1.1 The Beam-Laser Technique—A Brief Outline 1
CHAPTER TWO: THE EXCITATION PROCESS 14
2.1 Feasability—An Order of Magnitude Calculation 14
2.2 Variations in the Excited State Population 17
2.3 The Excitation Process—The Excimer Laser 18
2.4 The Excitation Process—The Dye-Laser Beam 25
2.5 The Effect of Zeeman Quantum Beats on Decay Curves 30
CHAPTER THREE: THE TARGET CHAMBER 33
3.1 Scattered Light 34
3.2 Doppler Tuning 40
3.3 Detection System Optics 44
3.4 Ion Beam–Optics Alignment 46
3.4.1 Initial Alignment Procedure 53
3.5 Laser Beam Optimization 54
CHAPTER FOUR: ION-BEAM PRODUCTION 58
4.1 Titanium Beam 58
4.2 Calcium Beam 59
4.3 Sodium Beam 60
4.4 Velocity Calibration 62
CHAPTER FIVE: DATA COLLECTION AND ANALYSIS 65
5.1 Data Collection 65
5.1.1 Background Signals and Gating 66
5.1.2 Normalization 67
5.2 Data Analysis 68
5.2.1 Single-Photon Counting Pile-up Correction 68
5.2.2 The Single-Exponential Decay Signal 73
5.2.3 Fitting the Decay Curve 73
5.3 Estimation of the Uncertainty in the Lifetime 75
5.3.1 Random Sources of Error and the Estimated Error 75
5.3.2 Systematic Sources of Error 76
CHAPTER SIX: DISCUSSION OF RESULTS 79
6.1 The Titanium Experiment 79

6.2 The Calcium Experiments 81
6.2.1 The [Ca] Experiment—$^2P_{1/2}$ 82
6.2.2 The [Ca] Experiment—$^2P_{3/2}$ 83
6.2.3 The [IR-Ca] Experiments—$^2P_{1/2,3/2}$ 84
6.3 The Sodium Experiment 88
6.4 CONCLUSIONS 89
REFERENCES 93
APPENDIX I: QUANTUM BEAT CALCULATION 95
A1.1 Quantum Beats — General 96
A1.2 Quantum Beats — J=1/2 Level 98
A1.3 Quantum Beats — J=3/2 Level 99
A1.3.1 The $I_{\Delta m=0}$ Component 102
A1.3.2 The $I_{\Delta m=1}$ Component 103
A1.3.3 The $I_{\Delta m=2}$ Component 103
APPENDIX II: LENS ALIGNMENT PROCEDURE 105
APPENDIX III: ZERO-FIELD QUANTUM BEATS 108

LIST OF TABLES

Table 1.1 Summary of the experimental parameters for all the experiments presented in this thesis.....8

Table 5.1 Maximum effects of systematic errors on the lifetime.....77

Table 6.1 The lifetime of the $z\ ^4D^o_{5/2}$ level of Ti^+ as determined from individual runs.....80

Table 6.2 Systematic effects on the observed titanium lifetime.....81

Table 6.3 Comparison of the results of different fitting procedures for the [Ca] $^2P_{3/2}$ series of experiments.....84

Table 6.4 Systematic effects on the observed calcium lifetime ([IR-Ca] series of experiments).....85

Table 6.5 Lifetimes(ns) obtained from single-exponential fits for the [IR-Ca] experiments.....86

Table 6.6 Systematic effects on the observed sodium lifetime.....88

Table 6.7 The lifetime of the $2p^5(^2P^o_{3/2})3p[5/2]_{J=3}$ level of Na^+ as determined from individual runs and summed data sets.....90

Table A3.1 Hyperfine structure of $2p$ levels of ^{21}Ne.....108

LIST OF FIGURES

Fig. 1.1 Generalized energy-level diagram and experimental configuration for a beam-laser experiment.....2

Fig. 1.2. Partial energy level diagram for Ti^+ showing the excitation and decay (monitored) transitions.....5

Fig. 1.3. Partial energy level diagram for Ca^+ showing the excitation and decay (monitored) transitions.....6

Fig. 1.4. Partial energy level diagram for Na^+ showing the excitation and decay (monitored) transitions.....7

Fig. 1.5 Sample intensity decay curve for the Ti^+ experiment.....9

Fig. 1.6 Sample intensity decay curve (summed data) for the [Ca] experiment for the J=3/2 level.....10

Fig. 1.7 Sample intensity decay curve (summed data) for the [IR-Ca] experiment for the J=3/2 level.....11

Fig. 1.8 Sample intensity decay curve (summed data) for the [Na] experiment.12

Fig. 2.1. Schematic of laser interaction with the ion beam showing the state of the ions in relation to the time since the arrival of the laser pulse....15

Fig. 2.2. a) Excimer line profile (without Doppler broadening) compared to the power broadened atomic line profile. b)Excimer modes without Doppler broadening. c)Excimer modes with Doppler broadening combine to form an essentially horizontal profile over the power broadened atomic linewidth.....21

Fig. 2.3. Fractional population, $\eta(t)$, versus time in the radiation field for the titanium experiment.....26

Fig. 2.4. Effective fractional population, η^*, versus the intensity of the radiation field for the titanium experiment.....27

Fig. 2.5. Fractional population, $\eta(t)$, versus time in the radiation field for the sodium experiment.....28

Fig. 2.6. Effective fractional population, η^*, versus the intensity of the radiation field for the sodium experiment.....29

Fig. 3.1 Isometric schematic of the target chamber.....36

Fig. 3.2 Cross-section of the target chamber.....37

Fig. 3.3 Illustration of the effect of various ion and laser beam geometries in relation to slit orientations.....41

Fig. 3.4 Target chamber laser optical paths.....43
Fig. 3.5 Data for adjusting focusing of detection system optics.....45
Fig. 3.6 Ray tracing of detection system optics.....47
Fig. 3.7 Ray tracing of detection system optics with ion beam to lens distance equal to the back focal length, f_b.....48
Fig. 3.8 Ray tracing of detection system optics with ion beam to lens distance equal to $f_b - 4mm$.....49
Fig. 3.9.1 Variation of the ungated beam background (UBB) normalized to beam current as a function of distance from the interaction region.....51
Fig. 3.9.2 Variation of the ungated beam background (UBB) normalized to beam current as a function of distance from the interaction region.....52
Fig. 3.10 Schematic of the excimer laser beam delivery system.....55
Fig. 4.1 Illustration of the gas cell used for the sodium experiment.....61
Fig. 4.2 Energy calibration curves for 350keV accelerator.....63
Fig. 5.1 Gating sequence of data accumulation.....66
Fig. 6.1 Lifetimes(ns) of the $Ca^+ 4p^2 P^o_{1/2,3/2}$ levels obtained from this work as well as previous measurements and theoretical estimates.....87
Fig. 6.2 Lifetimes(ns) of the Na^+ $2p(^2P^o_{3/2})3p[5/2]_{J=3}$ level obtained from this work as well as previous measurements and theoretical estimates.....90
Fig. A2.1 Schematic for alignment of the interior and exterior optical systems.106
Fig. A3.1 Hyperfine structure of the $2p_9$ level in Na^+.....109

CHAPTER ONE

INTRODUCTION

Atomic lifetimes are often used to place relative f-value measurements on an absolute scale. In his article "Accurate Atomic Data and Solar Photospheric Spectroscopy" [Gr84], Grevesse notes that "solar and stellar spectroscopists urgently need transition probabilities of high accuracy for once ionized elements of the iron group". In many cases the estimated accuracy of the relative values is roughly an order of magnitude better than that of the lifetimes. The extensive work of Roberts et. al. [RAS73] in 1973, which used the beam-foil technique to determine lifetimes of over 40 levels in Ti I–II, has provided the absolute scale for many of the titanium f-value measurements since then (*e.g.* [RVC75],[DK80],[BMP82] and [BMPS82]). However, most of these lifetimes have uncertainties of 10–15%, mainly due to the well known problem of cascading in beam-foil measurements, while in [BMP82] and [BMPS82] the relative f-values are known to ±0.5%. The cascading problem can be avoided by using a laser beam rather than a foil to populate the level of interest. This has the additional advantage of avoiding possible line blending and velocity straggling at the foil, both of which may contribute significantly to the uncertainty of lifetimes determined using beam-foil excitation. Using this beam-laser technique one can obtain lifetimes with estimated uncertainties of about one percent or better. Some workers [GKA82] have obtained uncertainties of less than ±0.2% in experimentally favorable circumstances (*e.g.* resonance transitions from the ground state with wavelengths greater than 5000Å).

1.1 The Beam-Laser Technique—a brief outline

As implied above, the essence of the technique is to selectively excite the level of interest by crossing an ion beam with a laser beam of the appropriate wavelength. A generalized experimental situation is shown in Fig. 1.1.

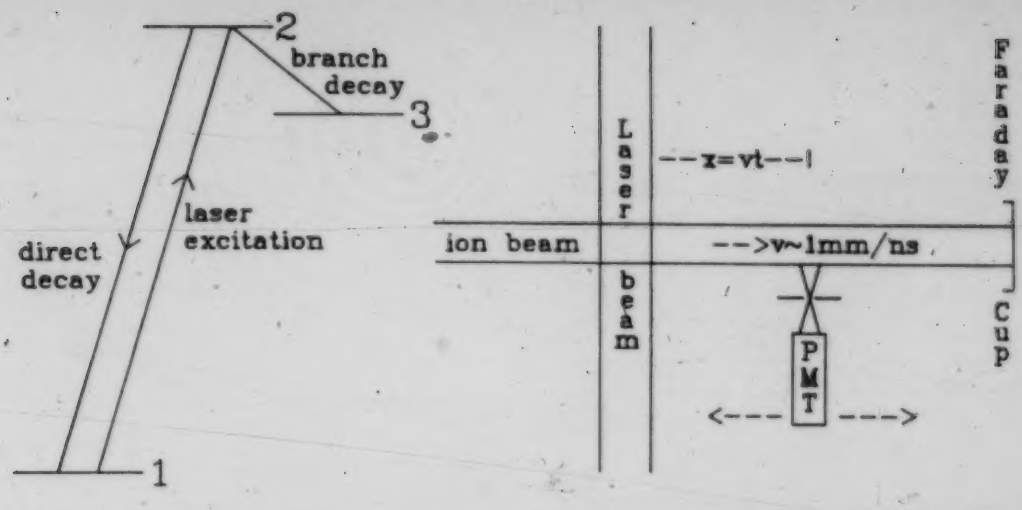

Fig. 1.1 Generalized energy-level diagram and experimental configuration for a beam-laser experiment. The decay of the excited state is measured by observation of a branch transition ($2 \rightarrow 3$) or the "direct" transition ($2 \rightarrow 1$). Variations in the ion-beam current can be accounted for by normalizing the signal according to the current as measured by the Faraday cup.

The speed of the ion beam, typically about $1 mm/ns$, provides the time resolution required to measure lifetimes greater than about two nanoseconds. The low density of the ion beam and target chamber residual gas avoids the problems of radiative trapping and collisional de-excitation. After leaving the interaction region the number of ions in the excited state (level 2) decays exponentially with time:

$$N_2(t) = N_2(0)\exp(-t/\tau).$$

The corresponding single-exponential decay in the intensity of the monitored transition(s) ($2 \rightarrow 3$ or $2 \rightarrow 1$) with increasing distance of the detector from the interaction can be analyzed by a simple two-parameter least-squares fit to obtain the mean lifetime, τ.

This apparently ideal experimental situation is complicated by the presence of background signals due to the scattered laser light and ion-beam background (due to collisions of ions in the beam with the residual gas molecules).

To obtain a reasonable signal-to-noise ratio one must have a sufficiently large ion-beam current and adequately populate the upper state, as well as minimizing the scattered laser light and ion-beam background. The choice of whether to use a CW or pulsed laser depends on the level(s) one wants to study. The high-power pulsed excimer or excimer-pumped dye lasers used for this research are the only ones that provide sufficient power at the higher frequencies required for single-step excitation of ionized species. CW lasers are more limited in their application, being useful for some neutral species with resonance lines in the visible region (*e.g.* [GKA82]). The details of the excitation process are discussed in more detail in Chapter Two.

The intensity decay curves were accumulated by summing several (usually 10–20) successive "sweeps", each sweep being composed of from twenty to thirty data points corresponding to detector positions separated by 0.5–1.0mm. This multi-scaling technique reduces the effect of systematic errors (such as a slow drift of laser frequency or power) since each sweep lasts a short time (about 5 minutes) compared to the overall collection time for the whole decay curve. A further refinement of the multi-scaling technique was used in the last experiment: alternate sweeps along the ion beam were made in opposite directions, the sweeps made moving downstream from the excitation region being summed and analyzed independently of those made moving upstream towards it. The advantages of this forwards and backwards sweeping are discussed in Chapter Five along with the details of the data analysis and collection procedures.

Prior to starting this project an initial measurement here at the University of Alberta was made for levels in singly-ionized calcium, using a modified beam-foil target chamber [AIP85]. The resulting lifetimes had estimated uncertainties of about 5%. This large uncertainty (for a beam-laser experiment) was

primarily due to the large laser background levels. A major portion of this work involved designing a target chamber so as to minimize this background. This and other methods used to reduce the laser background are discussed in Chapter 3.

The experiments described in this thesis illustrate some possible variations of the beam-laser technique:

[Ti] Populate the upper level (see Fig. 1.2) by transition from the ground configuration by Doppler tuning a (fixed frequency) excimer laser. Monitor the decay of a branch transition.

[Ca] Populate the upper level (see Fig. 1.3) by transition from a ground state by using a tunable dye laser. Monitor the decay of the same transition.

[Na] Populate the upper level (see Fig. 1.4) by transition from a metastable level (populated using a gas cell) by Doppler tuning an excimer laser. Monitor the decay of the same transition.

[IR-Ca] Populate the upper level (see Fig. 1.3) by transition from the ground configuration by using a tunable dye laser. Monitor the decay of a branch transition.

For convenience of comparison between the experiments and since much of the same information will be used in the subsequent chapters, Table 1.1 summarizes most of the experimental parameters for each of the experiments. Also sample decay curves for each of the experiments are presented in Figs. 1.5–1.8 in order to make it easier to compare the relative intensities of the background and decay signals for the different experiments.

Another major component of the time spent on this work was in the production of an adequate ion-beam current for both the titanium and sodium experiments. In both of these cases only a fraction of the total beam current is useable. For the [Ti] experiment this is due to only a fraction of the ground state

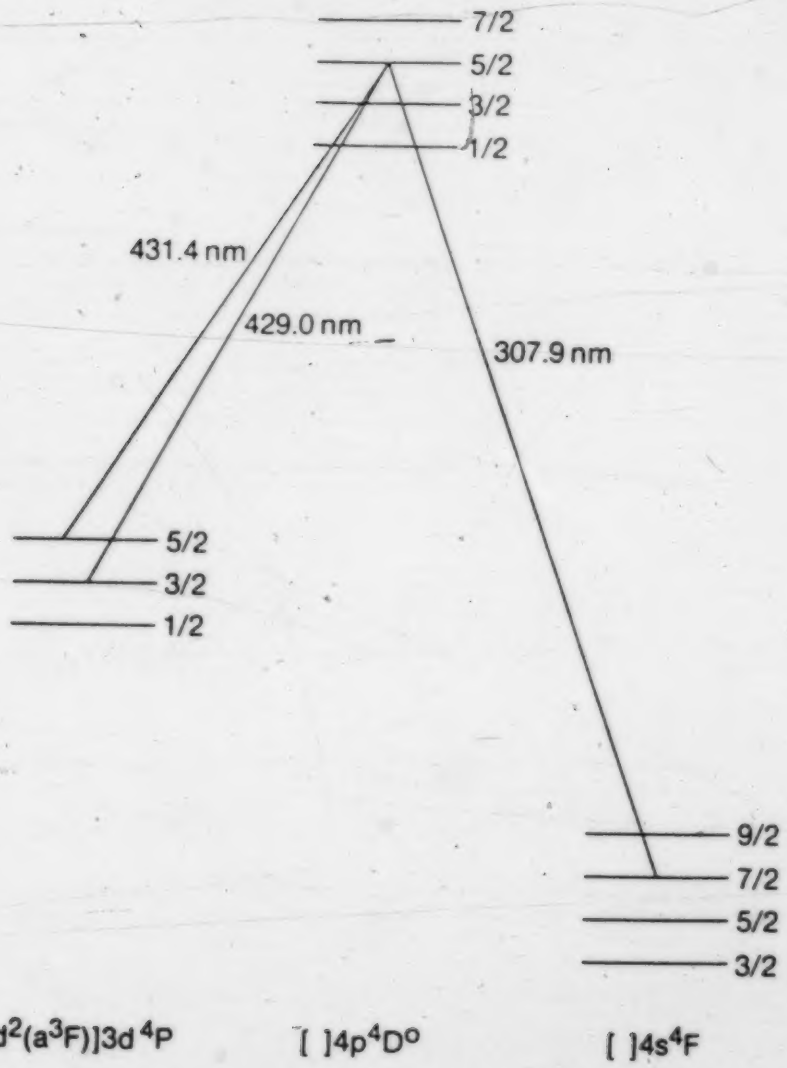

Fig. 1.2. Partial energy level diagram for Ti^+ showing the excitation and decay (monitored) transitions.

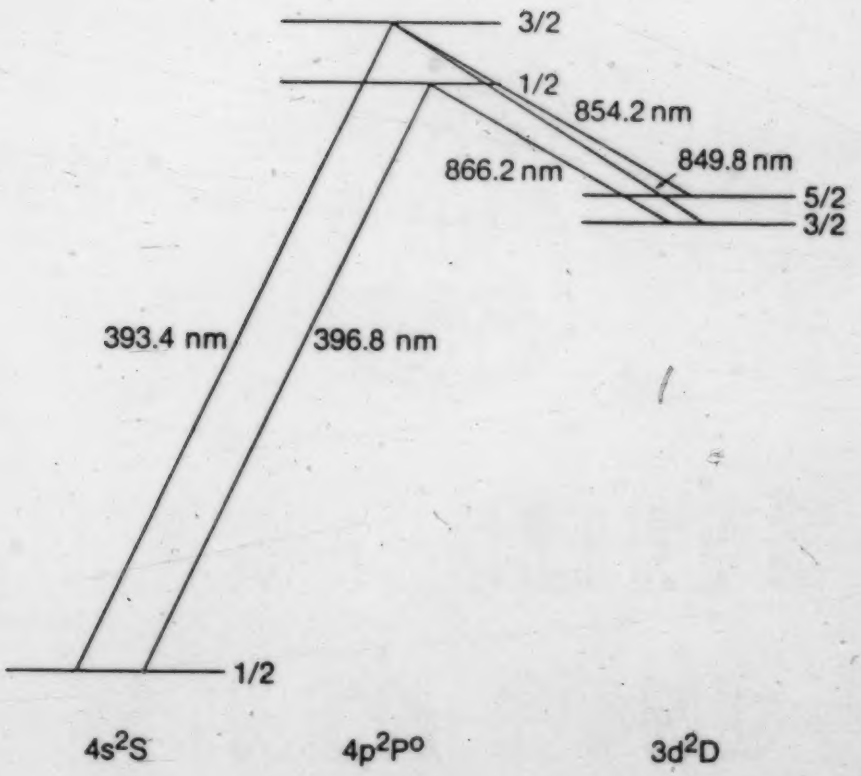

Fig. 1.3. Partial energy level diagram for Ca^+ showing the excitation and decay (monitored) transitions.

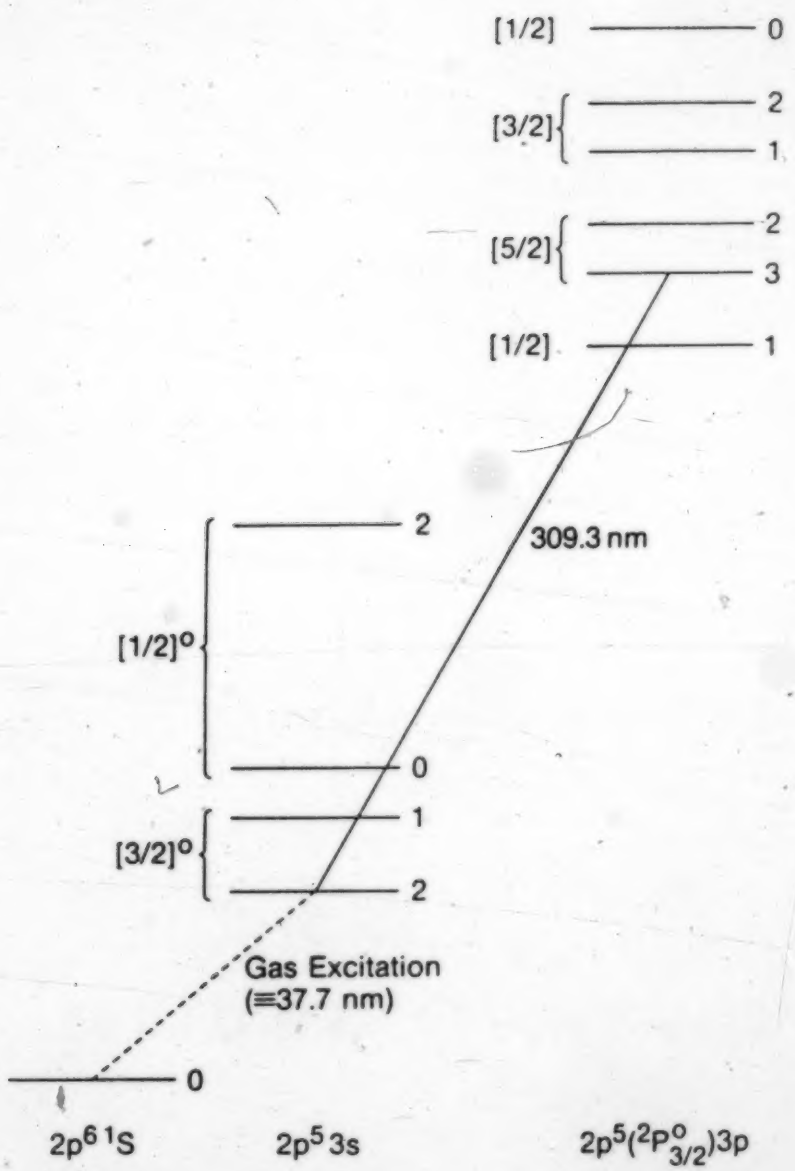

Fig. 1.4. Partial energy level diagram for Na^+ showing the excitation and decay (monitored) transitions.

EXPERIMENTAL PARAMETERS

EXPERIMENT:	[Ti]	$[Ca]_{J=1/2}$ {[IR-Ca]}	$[Ca]_{J=3/2}$ {[IR-Ca]}	[Na]
Ion-Beam Energy(keV)	238.3	250.0	250.0	279.6
-velocity(mm/ns)	0.979	1.099	1.099	1.531
-current(μA)	2–4	1–10{10}	13–14{5}	8–12
-dimensions(mm)	5	5{$3h \times 4w$}	5{$3h \times 4w$}	4
Transition $\lambda_T(nm)$	307.87	396.84	393.37	309.27
Laser $\lambda_L(nm)$	308.16	395.81	394.39	308.16
-(FWHM) linewidth(nm)	0.05	0.003	0.003	0.05
-pulse rate(pps)	300.0	200.0	200.0	200.0
-pulse duration(ns)	8	5	5	8
-mean intensity(mW/cm^2)	50	8.3{200}	8.3{200}	13
-peak intensity(kW/cm^2)	21	8.3{200}	8.3{200}	8.1
Ion/Laser Beam Angle(°)	107	45	135	45
Monitored (λ_M)	428.02	396.84	393.37	309.27
wavelength(s) (nm)	432.29	{866.2}	{854.2}	
-filter center $\lambda_f(nm)$	430	402{870}	391{850}	313
-transmission @λ_M	40%	20%{30%}	10%{20%}	6%
Quantum efficiency@λ_M	19%	22%{5%}	22%{8%}	22%
Normalization	I	I	UBB{I}	UBB
Special Gating		delayed		
Lifetime(ns)	4.01 ± 0.06	$\{7.07 \pm 0.07\}$	$\{6.87 \pm 0.06\}$	4.80 ± 0.06

Normalization: I=beam current normalization; UBB=ungated beam background.

All but the [IR-Ca] experiment were done with an EMI 9789QB PMT, the IR-experiments were done with a Hamamatsu R943-02 PMT.

Table 1.1 Summary of the experimental parameters for all the experiments presented in this thesis.

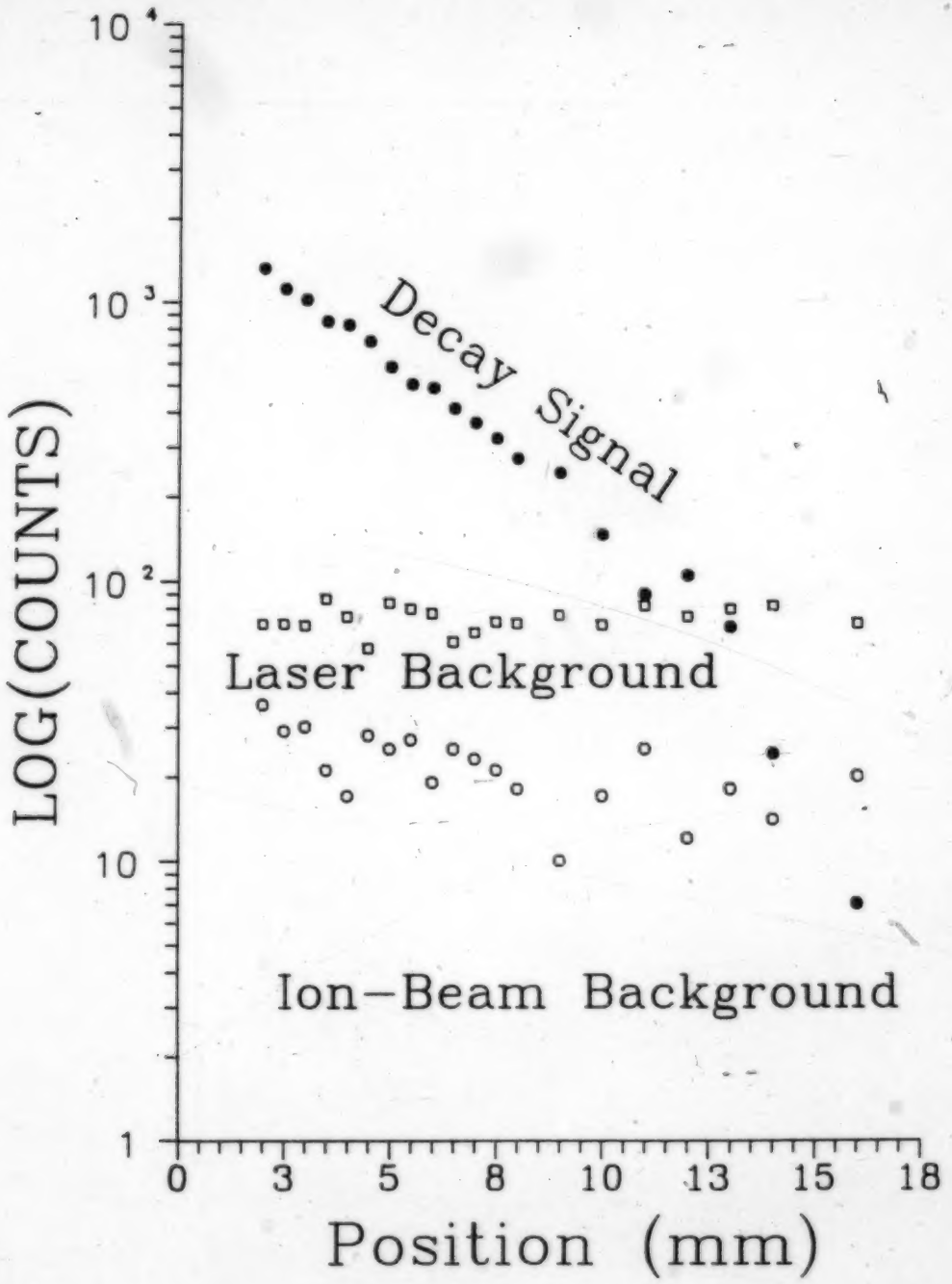

Fig. 1.5 Sample intensity decay curve for the Ti^+ experiment.

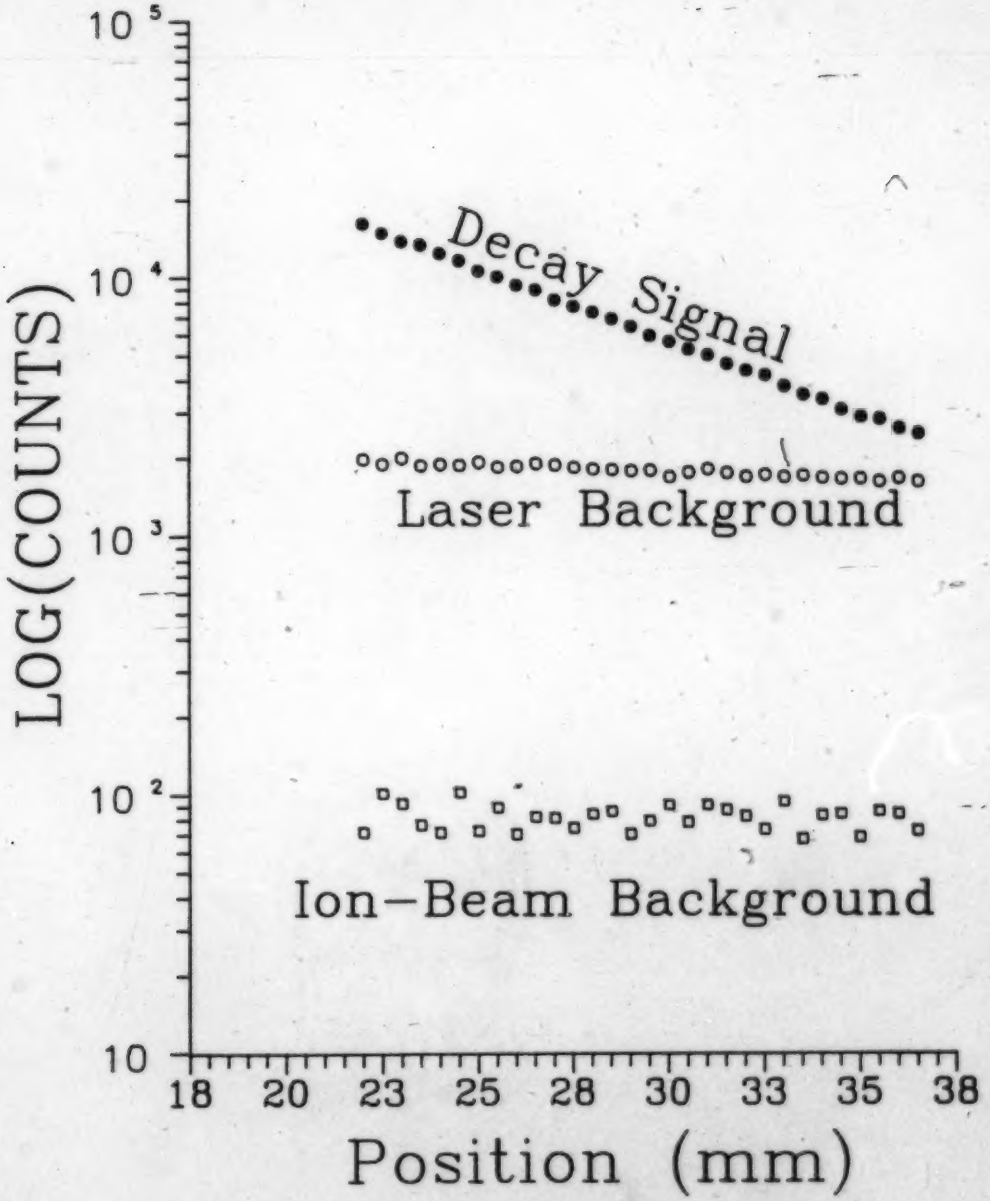

Fig. 1.6 Sample intensity decay curve (summed data) for the [Ca] experiment for the J=3/2 level.

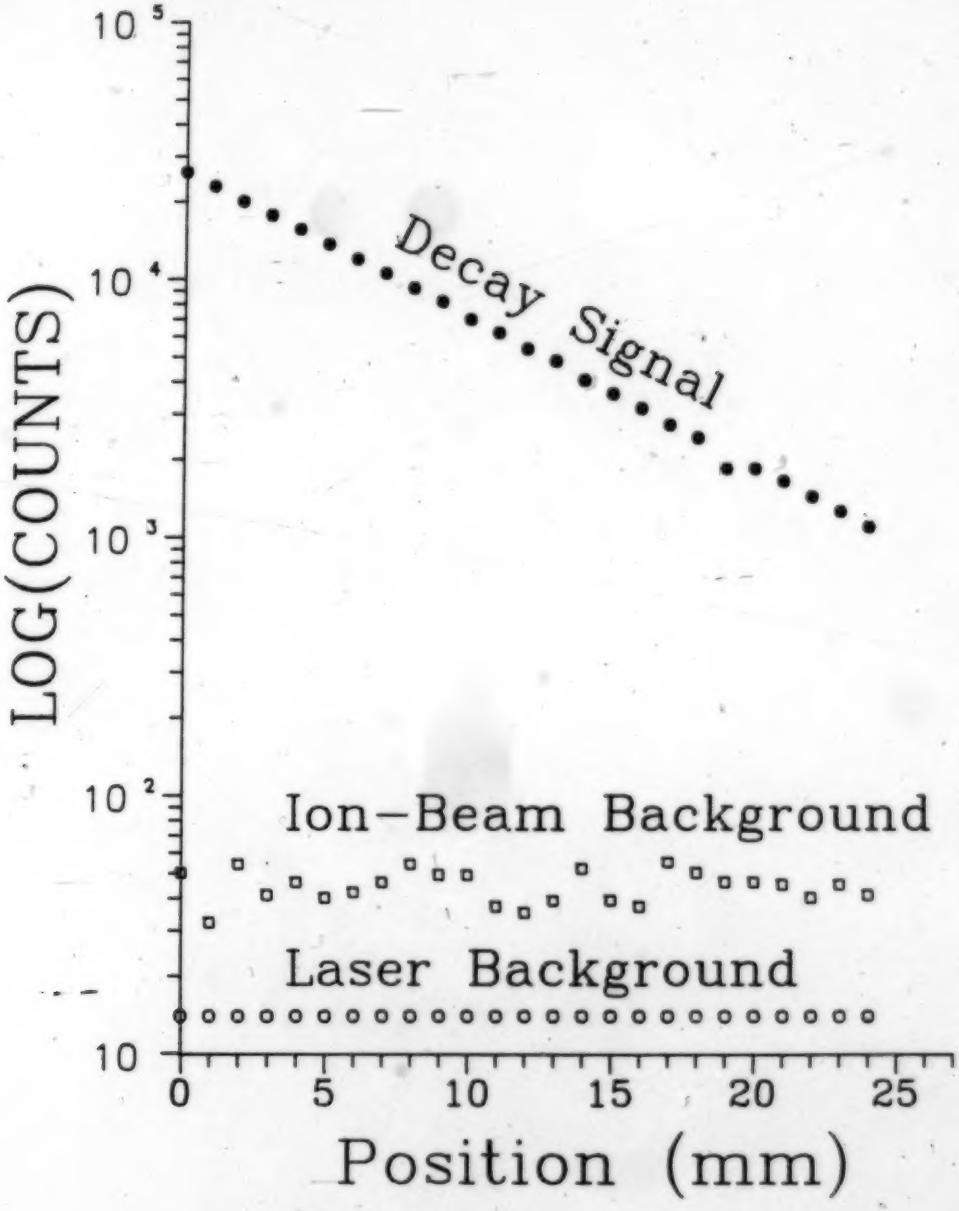

Fig. 1.7 Sample intensity decay curve (summed data) for the [IR-Ca] experiment for the J=3/2 level.

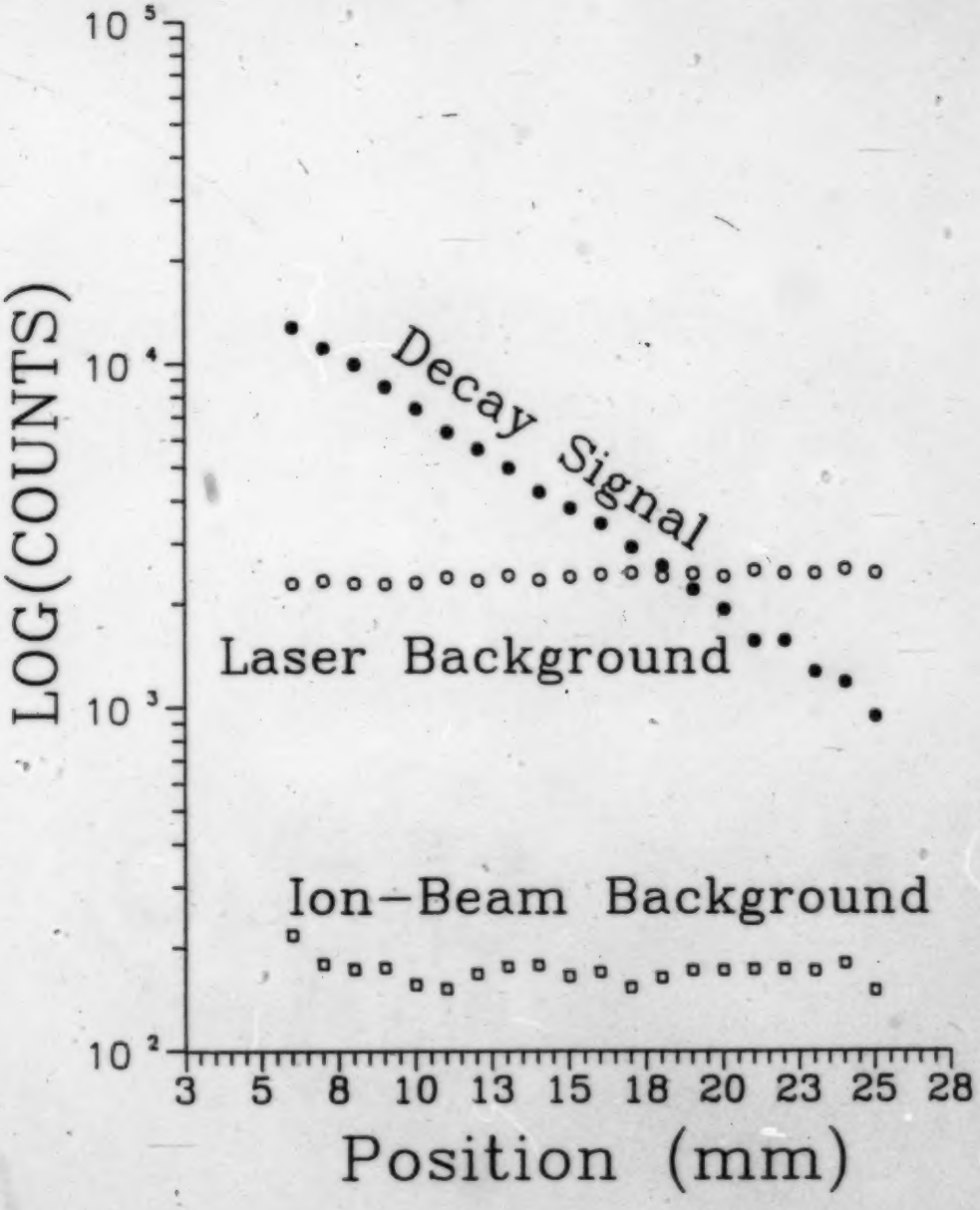

Fig. 1.8 Sample intensity decay curve (summed data) for the sodium experiment.

population being in the $J = 7/2$ level. For the [Na] case, only a fraction of the ions are excited by the gas cell to the meta-stable level (*i.e.* the lower level of the laser-excited transition). Ion-beam production is discussed in more detail in Chapter Four.

The [Ca] experiment was done more to develop techniques for the more difficult [Na] experiment than as the best way to measure the calcium levels involved. The calcium lifetimes were more accurately determined in the [IR-Ca] experiment where monitoring the branch transitions essentially eliminated the laser background. However, doing the calcium measurements both ways did reveal an unsuspected, albeit quite small, systematic error associated with the UBB(ungated beam background) normalization used in the [Na] and [Ca] experiments. This and other systematic sources of error are discussed in Chapter Five.

The results of the experiments as well as comparison with the theoretical and experimental results of others are discussed in Chapter Six.

CHAPTER TWO

THE EXCITATION PROCESS

The feasibility of the type of experiment outlined in the previous chapter depends on several interrelated factors. These include the (maximum) useable beam current(I), the overall collection efficiency($\mathcal{E}$), the signal to noise ratio(S/N) and how many ions are in the excited state as they leave the interaction region. The number of observed (decay) photons per laser pulse(CPP) will determine whether one should integrate photo-current($CPP >> 1$), count photons($CPP < 1$) or not do the experiment at all($CPP << BACKGROUND$). The first section of this chapter provides an order of magnitude calculation for the expected decay signal. The rest of the chapter examines the excitation process in more detail. In particular, possible systematic effects such as the dependence of the decay signal on laser intensity and Zeeman quantum beats induced by stray magnetic fields.

2.1 Feasability—An Order of Magnitude Calculation

The effect of the laser pulse on the ion beam is shown diagrammatically in Fig. 2.1. For simplicity it is assumed that the laser pulse duration(ϵ) is greater than the time an atom spends in the interaction region(L/v). The cross-hatched areas represent atoms being excited by the laser. The other shaded areas represent atoms which have ceased their interaction with the laser pulse, either because the pulse has ended or because they left the interaction region during the laser pulse.

The portion of the ion beam affected by the laser pulse will be referred to as the *burst* of ions. The length of the burst is $(v\epsilon + L)$ and a small transverse slice of the burst has length dy. The position of the slice within the burst is measured using the variable y, where $-v\epsilon \leq y \leq L$. If the laser pulse is sufficiently intense, the transition will be saturated essentially instantaneously. That is, the fraction, η, of ions in the upper state is given by $\frac{g_2}{(g_1+g_2)}$, where the g_i are the statistical

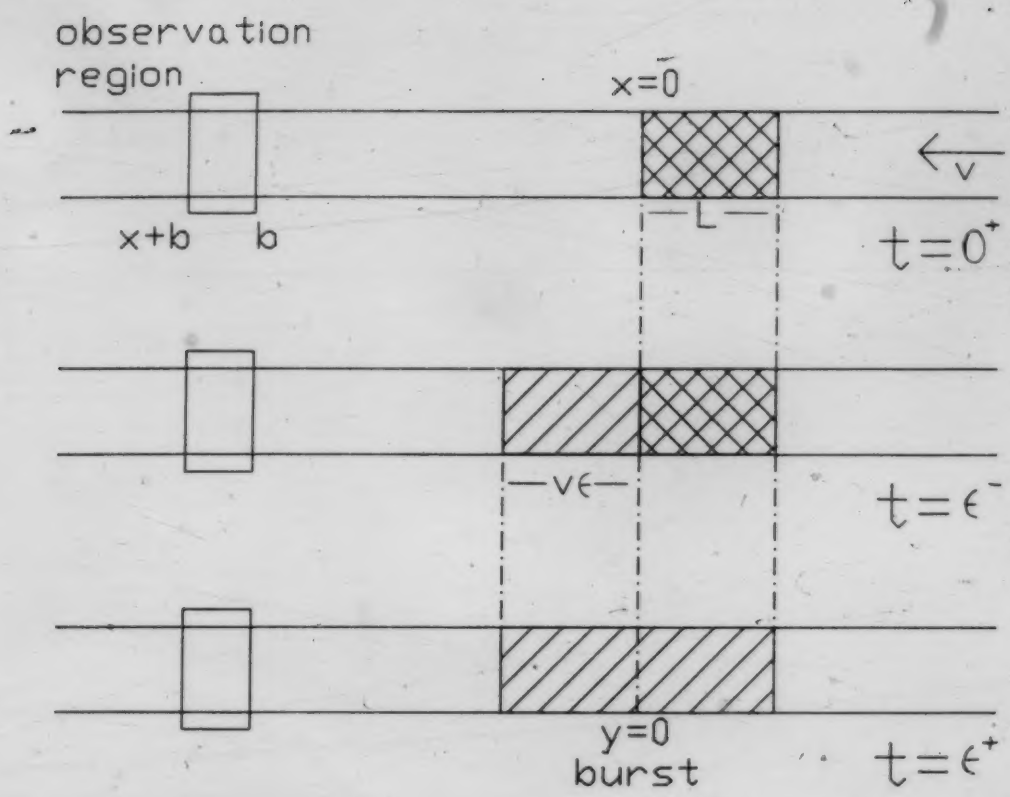

v =ion beam velocity
ρ =number of ions per unit length = I/ve
L = (effective) width of laser beam, typically $4mm$
b = observation length along the beam, typically $1mm$
ϵ = pulse duration of the laser
τ = lifetime of upper level
$l = v\tau$ = decay length

Fig. 2.1. Schematic of laser interaction with the ion beam showing the state of the ions in relation to the time since the arrival of the laser puise at $t = 0$.

weights of the two levels. Denoting the number of atoms in the slice y by $dN_y(x)$, where x is the distance from the downstream edge of the interaction region, one can write

$$dN_y(x) = \begin{cases} (\eta\rho dy)\exp\left(\frac{-(x+y)}{v\tau}\right), & \text{if } y \geq 0; \\ (\eta\rho dy)\exp\left(\frac{-x}{v\tau}\right), & \text{if } y \leq 0. \end{cases} \qquad (2.1.1)$$

Then letting $l = v\tau$ and A be the (summed) transition probability of the observed line(s), one finds that the contribution of slice y to the total observed counts is given by

$$\Delta N_y(x) = -\int_{t(x)}^{t(x+b)} \mathcal{E}\frac{d}{dt'}[dN_y(t')]dt' = \mathcal{E}Av^{-1}\int_x^{x+b}[dN_y(x')]dx'.$$

$$\text{Therefore,} \quad \Delta N_y = \mathcal{E}A\eta\rho l v^{-1}[1-e^{-b/l}]e^{-x/l} \times \begin{cases} e^{-y/l} & \text{if } y \geq 0; \\ 1 & \text{if } y \leq 0. \end{cases} \qquad (2.1.2)$$

Integrating over all the contributing slices one obtains:

$$\Delta N = \int_{-ve}^{L} \Delta N_y dy = \mathcal{E}A\eta\rho l v^{-1}[1-e^{-b/l}][l(1-e^{L/l}) + ve]e^{-x/l};$$

$$\text{or,} \quad CPP = [\mathcal{E}A\eta I\tau^2/e][1-e^{-b/l}][(1+\tfrac{e}{\tau}) - e^{-L/l}]e^{-x/l}. \qquad (2.1.3)$$

At this point is useful to note that it would be possible to increase the observed signal by increasing the observation length (*i.e.* slit width), b. Unlike beam-foil experiments where the decay curve is a multi-exponential, there would be no loss of information about the lifetime by using a longer averaging length. However, the background will increase faster than the signal does with increasing b. Also, the observation window profile is not perfectly rectangular as assumed in the calculation. Increasing the slit width would change the slope of the edge of the window function. This would mean starting the decay curve further downstream than for smaller values of b. Thus the detection system optics and the size of the lifetime being measured will in practice limit how large the observation length can

be made. There is nothing to be gained by making b larger than about half the lifetime. In the rest of this chapter the calculations for the expected signal use a conservative value of $b = 1mm$.

A rough estimate of the efficiency of the detection system can be made assuming an $f/2$ optical system (*i.e.* a solid angle $4\pi \times 0.016$), six optical interfaces to be traversed by the signal ($0.96^6 = 0.78$), the quantum efficiency of the photo-multiplier tube to be about 10% and the transmission of the filter to be about 10% at the wavelength of the observed transition(s). This yields a value for the detection efficiency of about $10^{-4}(0.01\%)$.

Using the values of $I = 1\mu A$, $\tau = 7ns$, $A = 1/7ns$, $\eta = 1/2$, $\epsilon = 5ns$, $L = 4mm$, $l = 7mm$ and $b = 1mm$ in eqn. 2.1.3, one obtains a value for CPP of about 0.3 counts per second(cps) at $x = 0$. Thus, acknowledging that this is an order of magnitude calculation, one expects at least 0.03 counts per laser pulse. At a laser pulse rate of $200pps$, this would produce a 25 point decay curve with 5,000 counts in the peak in about twelve hours of actual run time.

The above calculation indicates that this type of experiment is quite feasible provided the assumptions implied above hold. Also implicit in this analysis is the assumption that the population of the upper state produced by the laser does not vary systematically with time, at least on time scales comparable to the time to record one sweep of the decay curve. The next section examines the validity of this assumption.

2.2 Variations in the Excited State Population

A major concern in obtaining a reliable precision lifetime is the degree to which the excited state population, which is proportional to ηI, can be kept constant and an allowance made if it varies over one sweep. The ion-beam current fluctuations can be easily and accurately represented by scaling the decay signal

according to the digitized beam current integrated over the accumulation time. A data point on a typical decay curve had an uncertainty of less than about $\pm 0.2\%$ in the integrated beam current. In addition, the scaling typically produces changes in the decay signal of less than 5%.

The functional dependence of η on the laser intensity($\mathcal{I}$) is not known. The laser intensity had variations of the order of 2% over periods ranging from a few seconds to several minutes, but declines systematically by about 40% over four hours of continuous use. However, the typical sweep lasts for less than ten minutes giving a decline of less than about 3%. Since $\eta(\mathcal{I})$ is not known, it is not possible to scale the decay curve by measuring the laser intensity. Knowing the beam current it would be possible (in effect) to measure η directly by monitoring the decay intensity using a separate detection system at some fixed position downstream from the interaction region. The number of counts would be of the same order of magnitude as the peak signal. This would typically result in an uncertainty of greater than 3% in the correction. However it would be preferable not to have to make the correction at all since adding another detection system able to look near the interaction region would needlessly complicate the target chamber design if the correction itself were small. The next section calculates the expected order of magnitude of this correction.

2.3 The Excitation Process—The Excimer Laser

The excimer laser radiation is not coherent in the same sense as a single-mode CW laser. It can be regarded as a multi-mode (frequency, phase and polarization), high-intensity beam. As will be shown below, from the point of view of any atom in the ion beam, it is essentially a broad-band radiation source. Thus, one can use the Einstein A and B coefficients in a simple rate equation model for the excited state population evolution to estimate the effect of the systematic

decline in laser intensity during a sweep. Note that the simple rate equations do not necessarily accurately reflect the time evolution since the intensity is so large that the rate equation approximation is not valid. However, a sufficiently large intensity brings us into the regime where Rabi-oscillations would occur for a single-mode acting on the ion. Due to the presence of the multiple modes and the different amount of time each atom spends in the radiation field, the net effect of any Rabi-oscillations will be averaged out within a burst of ions to produce effective saturation of the upper level.

The excimer cavity length of $\simeq 1m$ produces modes about

$$\pi c/l = 1Grad/s \equiv \omega_q$$

apart. Over the total excimer linewidth(FWHM=$\Delta\omega_E$) of $1000Grad/sec(0.5\mathring{A})$, this implies about 1000 modes. The width of each mode will be given by

$$\Delta\omega_q \simeq (c/l)\frac{1-R}{\sqrt{R}} = 0.4Grad/s, \quad \text{assuming } R = \sqrt{R_1 R_2} = \sqrt{1}\sqrt{1-.96^2},$$

R_1 and R_2 being the reflectivity of the two ends of the excimer cavity. The power broadened atomic linewidth is given by (Lo83, Chapter Two)

$$\Delta\omega = \tau^{-1}\sqrt{1+2(\omega_R\tau)^2}, \quad \text{where } \omega_R^2 = \mathcal{I}\,\frac{A_{21}}{\omega^3}\,\frac{g_2}{g_1}\left[\frac{12\pi c^2}{\hbar}\right] \tag{2.3.1}$$

Using typical values for the titanium experiment:

$$\tau = 4.01ns,\ A_{21} = 0.137ns^{-1},\ \omega = 6.12\times 10^{15}rad/s,\ g_1 = 8,\ g_2 = 6,$$

and $\mathcal{I} = 210MW/m^2$ gives $\omega_R = 55Grad/s$ and $\Delta\omega = 310(1/\tau) = 78Grad/s$.

Thus, the excimer linewidth is sufficiently greater than the power broadened atomic linewidth ($\Delta\omega_E > 10\Delta\omega$) that all of the mode profiles are the same within

the atomic linewidth. Since the mode spacing is about twice the linewidth, one might initially expect the intensity profile across $\Delta\omega$ to be very non-uniform. However up to this point we have neglected any Doppler broadening due to the divergence of the laser beam. Although the laser beam was reasonably well collimated, a residual divergence of the order of $0.1 mrad$ remains. This divergence is sufficient to remove any non-uniformities in the excimer mode spectrum as seen by any particular atom:

$$d\theta \simeq 0.1 mrad \rightarrow \Delta\omega_D \simeq (v/c)\cos 17^\circ \, d\theta \times \omega = 2 Grad/s \simeq 2 * \omega_q.$$

Fig. 2.2 illustrates this situation. Thus, for the titanium and sodium experiments, we are justified in treating the excimer radiation as broad-band thermal radiation. The simple rate equation model can be used to provide an estimate of the maximum possible effect due to declining laser intensity.

We now develop the rate equation model (Co77, Chapter Nine) for the three-level atomic systems under consideration (see Fig. 1.1). The rate of change of population of the upper state is given by

$$\dot{N}_2(t) = B_{12}^{\rho}\rho N_1 - [A_{21} + A_{23} + B_{21}^{\rho}\rho]N_2(t).$$

The A_{ij} and B_{ij}^{ρ} are the usual Einstein coefficients. The ρ is the energy density per unit bandwidth which is a constant over the atomic line profile. Since we are interested in probabilities, it is convenient to set the total number of atoms equal to one. Also, since for the time scales under consideration there is no significant repopulation of level 1 via level 3, one can set $A_{31} = 0$. Therefore

$$N_3(t) = \int_0^t A_{23} N_2(t')\, dt'.$$

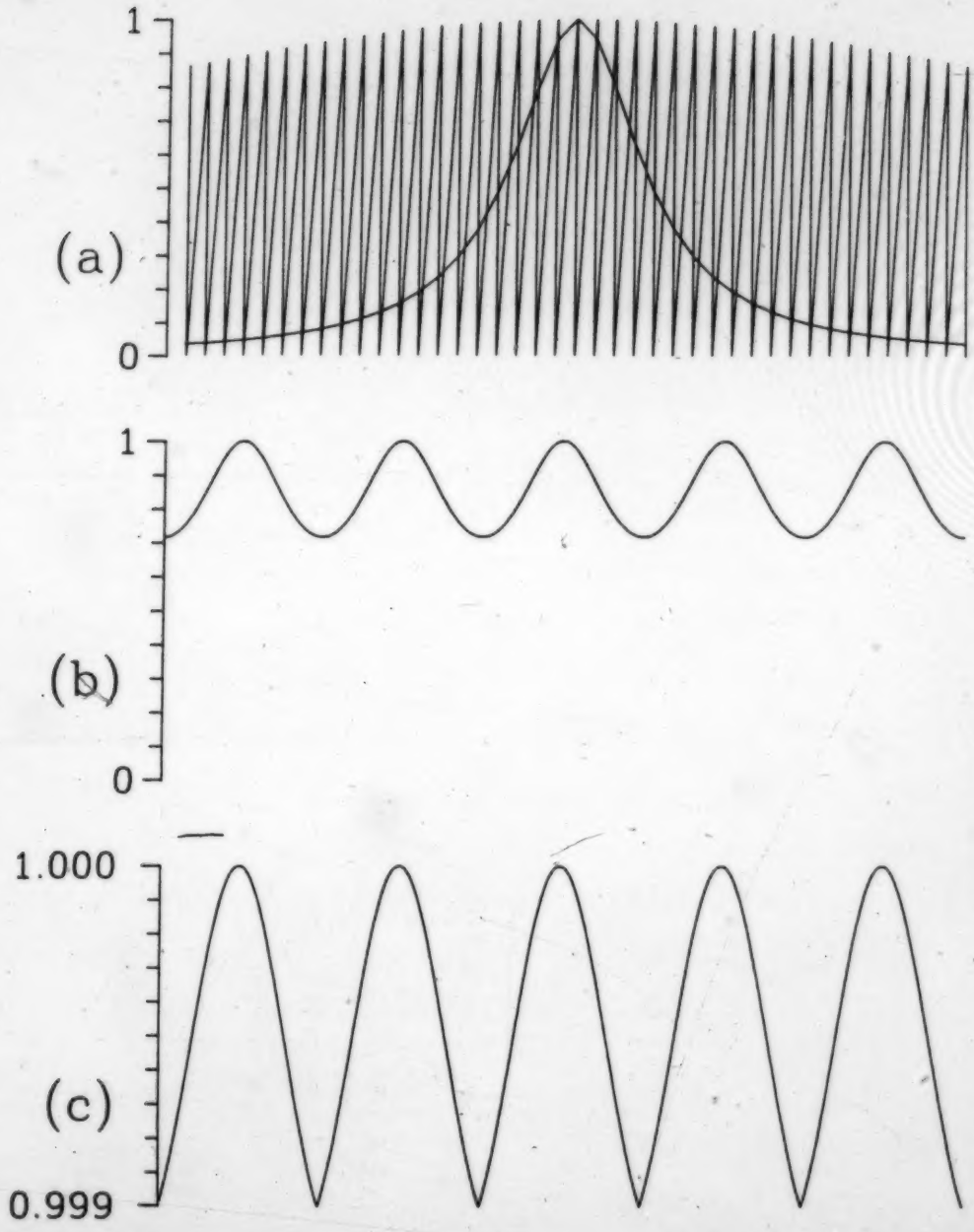

Fig. 2.2. a) Excimer line envelope (mode frequencies not to scale) compared to the power broadened atomic line profile (FWHM=12GHz). b)Excimer modes (60MHz apart) without Doppler broadening. c)Excimer modes with Doppler broadening combine to form an essentially horizontal profile over the power broadened atomic linewidth.

Using $B_{21}^{\rho} = \frac{g_1}{g_2} B_{12}^{\rho}$ and $A_{21} + A_{23} = \tau^{-1}$ one obtains

$$\dot{N}_2(t) = B_{12}^{\rho}\rho \left(1 - \int_0^t A_{23} N_2(t')\, dt'\right) - \left[\tau^{-1} + (1 + g_1/g_2) B_{12}^{\rho}\rho\right] N_2(t).$$

This equation can be written as

$$\dot{N}_2(t) = \beta \left(1 - \int_0^t A_{23} N_2(t')\, dt'\right) - \alpha N_2(t), \tag{2.3.2}$$

where $\beta = B_{12}^{\rho}\rho$ and $\alpha = \tau^{-1} + (1 + g_1/g_2))\beta$. The two quantities, α and β, are constant as long as ρ (*i.e.* laser intensity) is constant.

$$\beta = \left[\frac{g_2}{g_1}\left(\frac{\pi^2 c^3}{\hbar\omega^3}\right) A_{21}\right]\left[\frac{\mathcal{I}}{c\,\Delta\omega_E}\right] = \left(\frac{g_2}{g_1}\right)\frac{\lambda_{21}^5 A_{21}\mathcal{I}}{8\pi h c^2 \Delta\lambda_E} \tag{2.3.3}$$

which, for convenience in calculation, can be written as

$$\beta(ns^{-1}) = 6.681 \times 10^{-19}\left(A_{21}\lambda_{21}^5 g_2/g_1\right)\mathcal{I}/\Delta\lambda_E \tag{2.3.4}$$

where in the latter equation the units are in ns^{-1}, Åand kW/cm^2 where appropriate. If $A_{23} = 0$, eqn. 2.3.2 can easily be solved to yield

$$N_2(t) = \frac{\beta}{\alpha}(1 - e^{-\alpha\tau}).$$

The integro-differential equation 2.3.2 is most conveniently solved numerically on a computer. The program EXCITE was written to perform the required calculations. One inputs the maximum laser intensity $\mathcal{I}_{max}$, g_1, g_2, A_{21}, τ, λ_{21}, $\Delta\lambda_E$ and v. The program prints and graphs the *effective* fractional population at the end of the interaction region(η^*) versus the intensity down to 60% of the maximum intensity. It will also plot the actual fractional population as a function of time in the radiation field for the maximum and minimum values of the intensity.

Before examining the details of how the variation of η^* with laser intensity can affect the measured lifetime, we first check whether the calculated value of η^* for the titanium experiment corresponds to the observed value of CPP. Using the values for the titanium experiment of $\mathcal{I}_{max} = 24kW/cm^2$, $g_1 = 8$, $g_2 = 6$, $A_{21} = 0.137ns^{-1}$, $\tau = 4.01ns$, $\lambda_{21} = 3979\mathring{A}$, $\Delta\lambda_E = 0.5\mathring{A}$ and $v = 0.979mm/ns$ one obtains $\eta^* = 0.28$ from the program EXCITE.

To calculate the expected signal one proceeds as in section 2.1 except η^* replaces $\eta \exp(-y/v\tau)$:

$$\Delta N_y = -\int_x^{x+b} \frac{d}{dt}(dN_y)\,dt = \mathcal{E}A\eta^*\rho l v^{-1}[1 - e^{-b/l}]e^{-x/l}\,dy$$

$$\text{therefore} \qquad \Delta N = \mathcal{E}A\eta^*\rho l v^{-1}[1 - e^{-b/l}][L + v\epsilon]e^{-x/l}$$

$$\text{or,} \qquad CPP = [\mathcal{E}A\eta^* I^* \tau^2/e][1 - e^{-b/l}][L/l + \epsilon/\tau]e^{-x/l} \qquad (2.3.5).$$

For convenience we rewrite this in terms of experimental units (*i.e.* ns, mm and μA) as well as factoring out the assumed filter efficienc $(F_{\%})$ of 10%:

$$CPP = \{0.624F_{\%}/10\%\}\,[A\eta^* I^* \tau^2][1 - e^{-b/l}][L/l + \epsilon/\tau]e^{-x/l} \qquad (2.3.5).$$

The transmission of the filter used in the titanium experiment was about 40% for the two observed transitions. The summed transition probability(A) for these two transitions is about $0.0086ns^{-1}$ as obtained by correcting the (RAS) relative f-value results with our measured lifetime. A particular experimental run gave $CPP = 0.031$ at $x = 2mm$ with a mean beam current of $4\mu A$. The I^* in equation 2.3.5 is the effective beam current since all the ions contributing to the measured beam current are not in the $J = 7/2$ level of the lowest multiplet and thus cannot be excited by the excimer radiation. Assuming that the distribution of ions follow a Boltzmann distribution with a temperature of about $300°K$, one expects about

a quarter of the ions to be in the $J = 7/2$ level (*i.e.* $I^* \simeq I/4$). Using the above values and $L = 4mm$ and $\epsilon = 8ns$ in equation 2.3.5, one obtains an expected value of CPP of $0.037cps$. The experimental and observed values are suprisingly close considering the approximate nature of the values used in the calculation (especially the efficiency, $\mathcal{E}$).

The time development of the excitation probability for titanium is shown in Fig. 2.3. The significant decline in population starting at about $2ns$ is caused by the relatively large value of A_{23}/A_{21}. However, Fig. 2.4 shows that η^* varies quite slowly with intensity. A typical 3% drop in $\mathcal{I}$ over one sweep of the decay curve corresponds to about a 0.4% drop in η^*. The effect of this decline on the measured lifetime is estimated by regarding it as a small time dependent change in the amplitude of the decay curve:

$$N(t) = C(1 + \xi t)\exp(-t/\tau)$$

If, over the typical decay curve of three lifetimes, the effective amplitude changes by a factor $(1 + q)$, this implies that $3\tau\xi = q$, or, $\xi = q/3\tau$. Therefore,

$$N(t) \simeq C\exp\left(\frac{-t}{\tau(1 + q/3)}\right).$$

Thus the 0.4% decline in η^* corresponds to about a 0.1% decrease in the measured lifetime. This is a very small effect when compared to the minimum uncertainty in the lifetime caused by the 0.5% uncertainty in the velocity. Also, the preceding calculation assumed that the rate equations were valid in this high-intensity regime and thus over-estimated the effect of declining laser intensity. This effect, as well as any other small *real-time* dependent effect on the effective amplitude, could essentially be eliminated by recording successive sweeps of the decay curve in opposite directions.

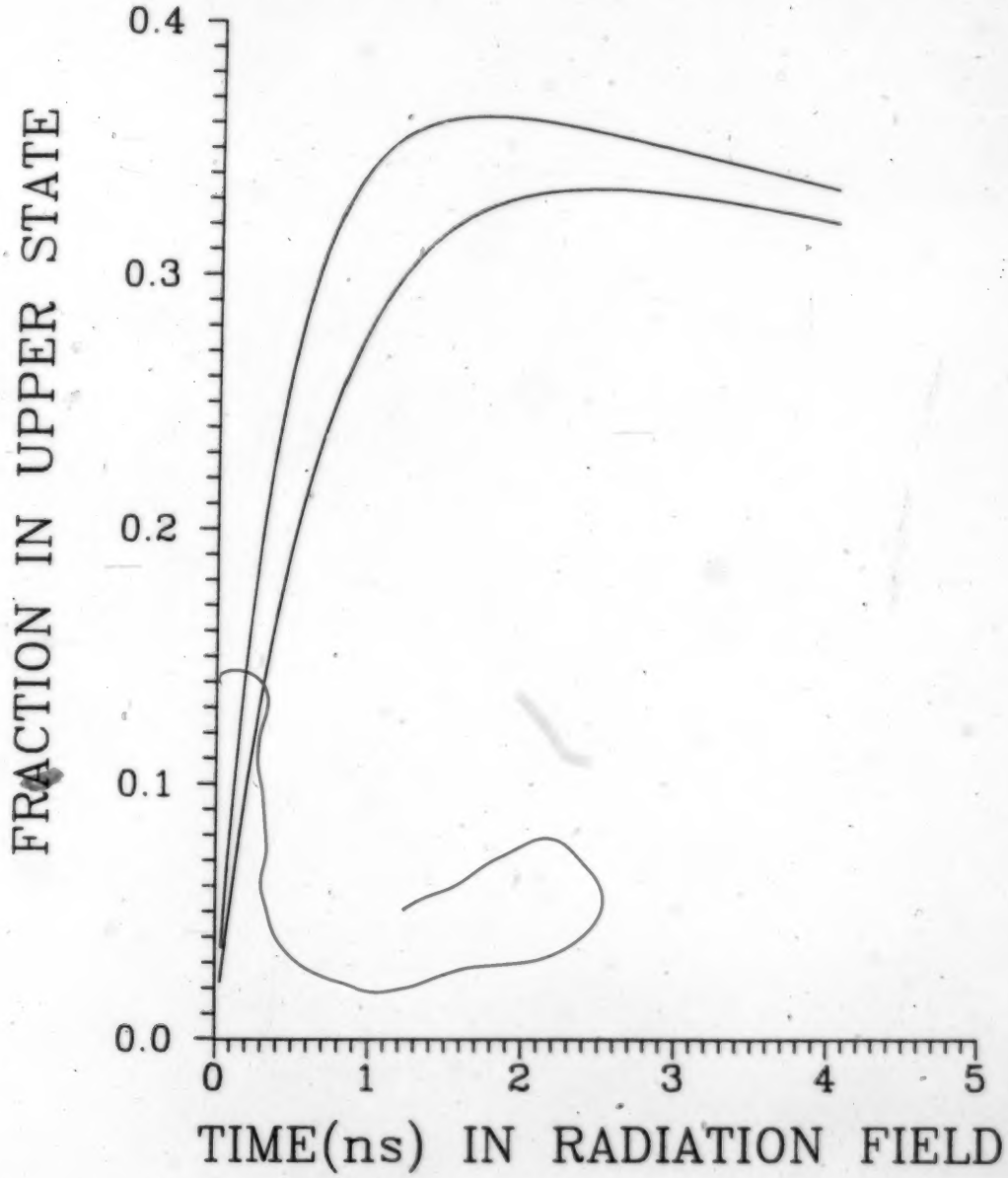

Fig. 2.3. Fractional population, $\eta(t)$, versus time in the radiation field for the titanium experiment. The upper curve is at maximum intensity and the lower curve is at 60% of the maximum.

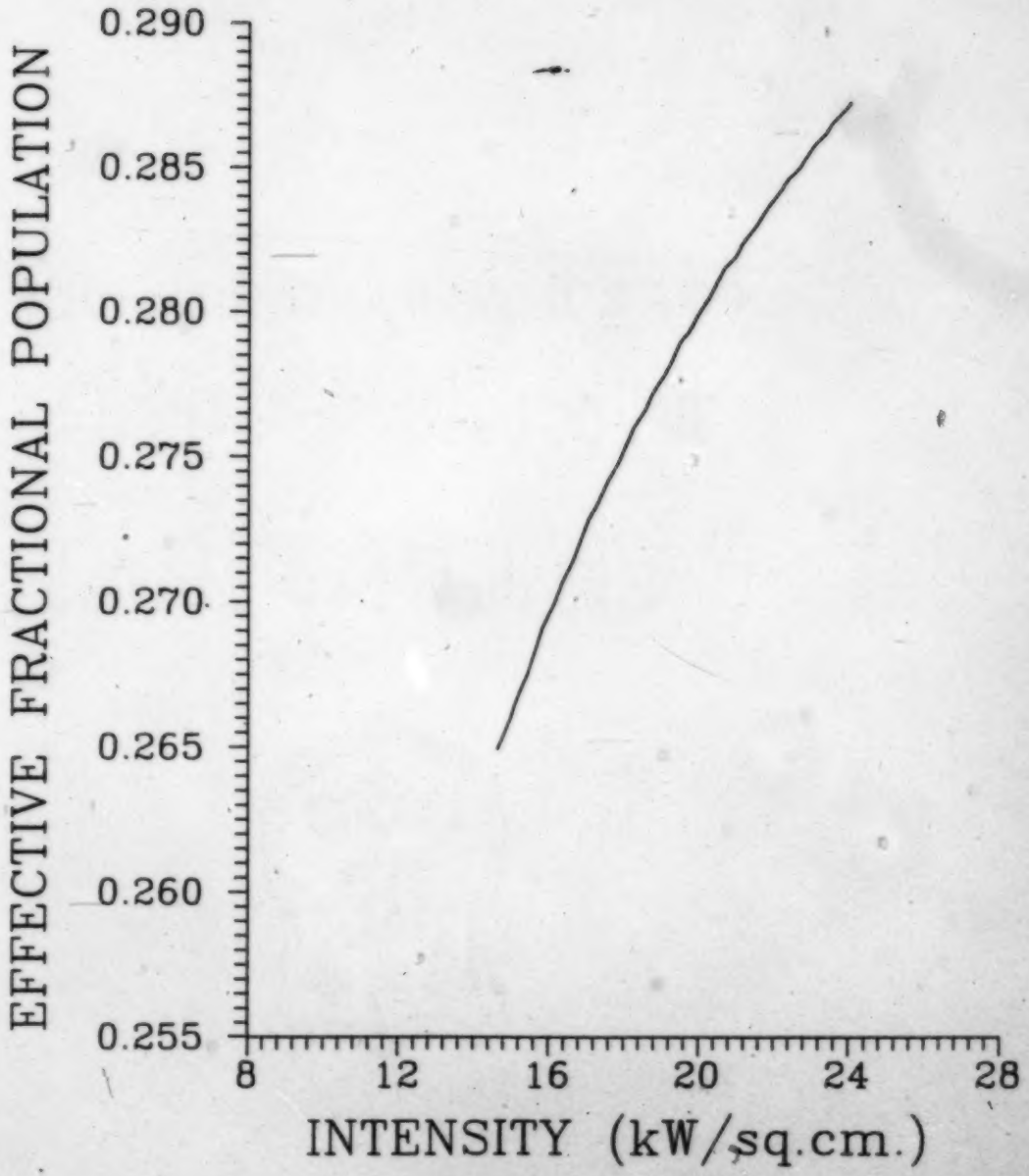

Fig. 2.4. Effective fractional population, η^*, versus the intensity of the radiation field for the titanium experiment.

The nature of the laser excitation process for the sodium experiment is essentially the same as for the titanium experiment. The change in the effective fractional excited state population with declining laser intensity, as given by the rate equation approximation and shown in Figs. 2.5 and 2.6, will cause the measured lifetime, τ^*, to be at most 0.2% too small.

The excitation process for the sodium experiment also involved using a gas cell (see §4.3) to populate the metastable level. The efficiency of the cell, in effect I^*/I, can be estimated using the observed value of CPP and the calculated value for η^*. With $I \simeq 10\mu A$. Using the sodium parameters from Table 1.1 and equation 2.3.5, one obtains $I^*/I \simeq 0.08$, an 8% efficiency for the gas cell.

2.4 The Excitation Process—The Dye-Laser Beam

The principal differences between the dye and excimer beams used in these experiments are the much smaller dye-laser beam total linewidth ($0.03\mathring{A}$ versus $0.5\mathring{A}$) and the greater than 96% vertical polarization of the dye beam.

The power-broadened atomic linewidth at the intensity used in the calcium experiments can be calculated using equation 2.3.1 and the following values for the parameters:

$$\omega = 4.75 \times 10^{15} rad/s \; \mathcal{I} = 80 MW/m^2 \; A_{21} = 0.13 ns^{-1} \; \tau \simeq 7 ns \; \frac{g_2}{g_1} = 1.$$

$$\text{Therefore,} \qquad \omega_R = 60 Grad/s \simeq 400(1/\tau) \quad \text{and} \quad \Delta\omega = 600(1/\tau).$$

Converting to wavelength one obtains $\Delta\lambda \simeq 0.07\mathring{A}$. Thus the whole laser line is contained within the power broadened atomic linewidth. The Rabi frequency corresponds to a period of $0.1ns$ which is much less than the typical interaction time between an ion and the radiation field. Atoms spend anywhere up to about $4ns$ in the radiation field, so observing the radiation emitted by the burst is in

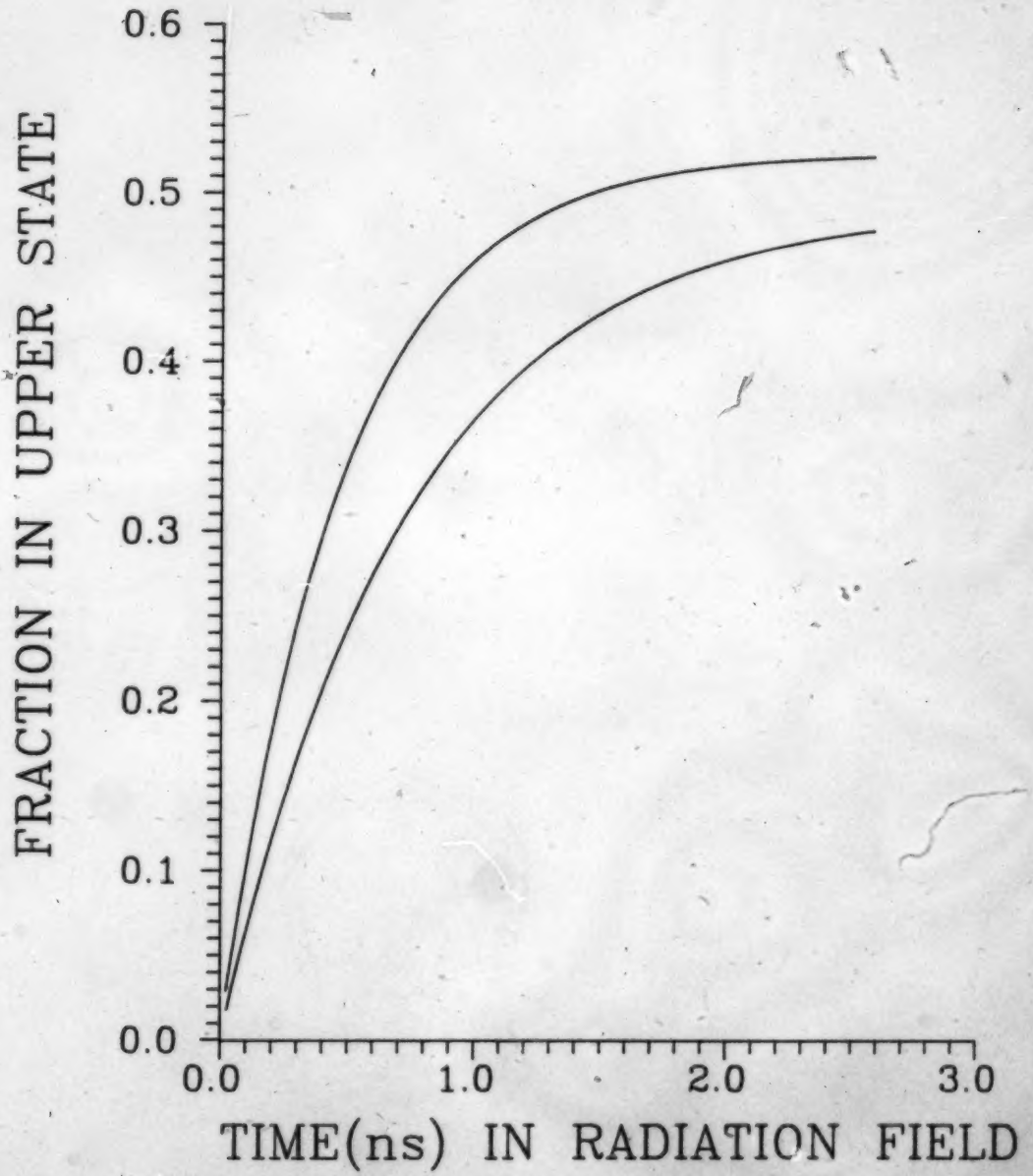

Fig. 2.5. Fractional population, $\eta(t)$, versus time in the radiation field for the sodium experiment. The upper curve is at maximum intensity and the lower curve is at 60% of the maximum.

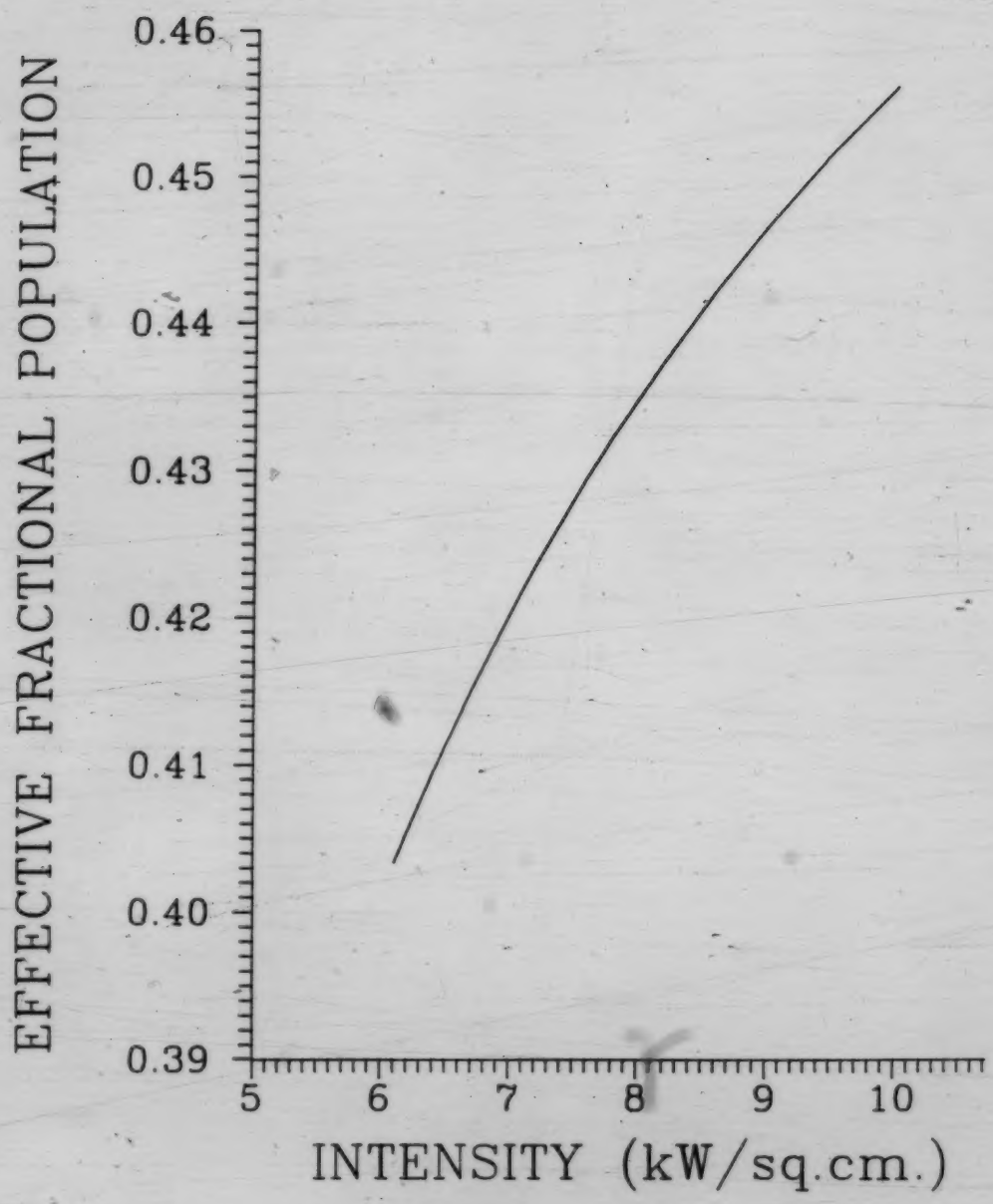

Fig. 2.6. Effective fractional population, η^*, versus the intensity of the radiation field for the sodium experiment.

effect averaging over many Rabi oscillations . This produces an effective saturation of the transition with $\eta = g_2/(g_1+g_2)$ in the upper state. Even if the laser intensity drops by a factor of two there is still enough power to saturate the transition.

For a particular calcium run (3968#8) with $I \simeq 10\mu A$ and $x = 35mm$, one observes $CPP \simeq 0.10cps$. Using equation 2.1.3 with $\eta = 1/2$, $\tau = 7ns$, $A_{21} = 1/\tau$, $v = 1.1mm/ns$ and $\mathcal{E} = 2 \times 10^{-4}$ (20% filter) one obtains an expected $CPP = 0.06cps$. Again, the difference between the two values can be attributed to the order of magnitude nature of the calculation.

2.5 The Effect of Zeeman Quantum Beats on Decay Curves

The experiments were done initially without any consideration of the possible effects of the earth's magnetic field (or any other stray magnetic fields) on the decay curves. The magnetic field (about $0.06mT$) causes the upper energy to split into magnetic substates separated by the Larmour frequency

$$\nu_L = (\mu_B/h)\, B\, g_J \qquad \text{where } g_J \text{ is the Landé g-factor.}$$

For the singly-ionized calcium $^2P_{3/2}$ level the Landé g-factor is $\frac{4}{5}$ so that one obtains

$$\nu_L = (1.4 \times 10^4)(0.6 \times 10^{-4})\, g_J\, (MHz/T) \simeq 1MHz.$$

This splitting of the upper magnetic substates allows the possibility of coherent excitation (in the sense described in detail in Appendix I) and decay of pairs of upper substates separated by $\omega = \omega_L$ or $2\omega_L$ (*i.e.* states whose magnetic quantum number differ by one or two units). As a result the decay signal may have components which correspond to interference (beating) between two magnetic substates as they decay to a common lower state. Thus the general expression for the decay curve is no longer a simple single-exponential but has the form

$$N(t) = [C + D_1 \cos(\omega_L t + \phi_1) + D_2 \cos(2\omega_L t + \phi_2)] \exp(-t/\tau). \qquad (2.5.1)$$

The relative values of the coefficients depend on the excitation and observation geometry and polarization in relation to the axis of quantization defined by the direction of the magnetic field.

The beat frequency present in the calcium experiments, which corresponds to a minimum period of about $500ns$, is too small to see any quantum beats in the decay curves (less than $30ns$ long). However, if D_1 and/or D_2 were large enough, there could be a significant effect on the measured (or apparent) lifetime. This occurs if, as described in the previous section, the amplitude varies to first order in time. This can occur in this situation as well since one can write

$$\cos(\omega_L t - \phi_1) = \cos\omega_L t \cos\phi_1 - \sin\phi_1 \sin\omega_L t \simeq \omega_L t \sin\phi_1, \quad \text{for } \omega_L t << 1.$$

For example, if one assumes $D_2 = 0$ one obtains

$$N(t) \simeq (A + D_1 \cos\phi_1)(1 + \xi t)\exp(-t/\tau), \qquad \xi = \frac{-\omega_L \sin\phi_1}{A + D_1 \cos\phi_1}.$$

A detailed calculation of the coefficients and phase angles was done for the calcium experiments in which no attempt was made to cancel the residual field. The details of this calculation are given in Appendix I. The results show that there is ***no possibility*** of quantum beats for the $^2P_{1/2}$ level and an expected 0.004% decrease in the lifetime for the $^2P_{3/2}$ level. Thus the presence of quantum beats had a very small effect on the results (the effect on the titanium experiment is expected to be of the same order of magnitude or less). This small effect can be included as another source of error when estimating the uncertainty of the lifetimes. Note that here the time dependence is manifested as an intensity variation that is a function of position along the ion beam, and hence effects due to quantum beats can not be corrected by alternating forward and backward sweeps along the ion beam.

The possible effects of zero-field quantum beats are considered in Appendix III. These only affect the [Na] experiment and, in contrast to the Zeeman quantum beats discussed above, the beat frequencies are too *large* to have a measurable effect on the observed lifetime (less than 0.02%).

CHAPTER THREE

THE TARGET CHAMBER

This chapter outlines the various considerations that were involved in the design of the target chamber. The extremely high scattered laser-light levels (comparable to the peak signal) obtained here at the University of Alberta by Ansbacher *et.al.*, (AIP85) using a modified beam-foil target chamber, made reduction of this background signal a primary objective. These high background levels were obtained even though the laser light was discriminated against using a narrow bandpass filter in the infrared while the laser radiation was below $400nm$. The reduction in laser background radiation had to be achieved within the constraints imposed by other factors, such as flexibility to use the target chamber for more than one particular experiment (e.g. to allow for Doppler tuning of the excimer laser), limitations on size in regards to pumping requirements for an adequate vacuum, relative ease of set-up alignment and operation, and, of course, overall cost.

The design of the target chamber was an iterative process which is difficult to describe in a linear step-by-step fashion. Although an attempt has been made to divide this chapter into sections dealing with particular aspects of the design, the divisions are not as clear cut as the section heading might imply. Also, since the goal was simply to reduce the laser scattered light to acceptable levels and not to determine the ideal configuration precisely or the relative importance of each source of laser scattered light, any figures quoted below giving reductions in laser scattered light upon doing such and such should be taken only as as rough indications as to the order of magnitude of the effect.

The last section is on laser beam production. It does not deal with the target chamber *per se*, but was included in this chapter since the quality of the laser beam is closely linked to the problem of scattered laser-light.

3.1 Scattered Light

The first step in minimizing the scattered laser-light was to ask what are its principal sources. The sheer number of photons, greater than about 10^{13} in a laser pulse, is enough to make even the air traversed by the beam before entering the target chamber a significant source of scattered light if the target chamber is not properly designed. Other important sources are the beam-steering mirror(s), the entrance and exit windows, amplified spontaneous emission from the laser and possibly the beam dump. Radiation scattered from the walls of the target chamber itself can also become important once the other sources have been reduced.

One might also ask how much scattered laser-light is too much. Clearly, if one expects peak decay signals of about $0.1cpp$; then, assuming an overall detection efficiency of about 10^{-4}, a thousand photons scattered into 4π steradians is too large. This is about one out of ten billion of the number of photons in the laser pulse.

The simplest step that one can take to reduce the scattered laser-light is to remove all scattering surfaces as far away as possible from the neighborhood of the interaction region and the laser beam. Of course, one wants to be able to observe as close to the interaction region as possible to maximize collection efficiency and to start the decay curve with as high a count rate as possible. This implies that one must place at least one lens close to the interaction region.

The collection lens was placed inside the target chamber so as to maintain a reasonable detection efficiency while placing the walls at least $10cm$ away from the interaction region. Obviously, the detection system should be optically isolated from the primary sources of scattered laser-light. That is, light from these sources should have to strike at least one, and preferably more, intermediate surface before entering the detection system. The target chamber design is such that that there are at least two such intermediate surfaces.

This was done by shielding the collection lens and mounting the entrance and exit windows at the ends of long (about $20cm$) baffled tubes (see Figs. 3.1 and 3.2). The tubes, as well as the target chamber were made from anodized black aluminum and the baffles of blackened copper to minimize multiple reflections of the scattered laser-light. However, the blackening process was found to severely dull the inside knife-edges of the baffles. These were resharperned and then blackened using lampblack (i.e. carbon) from a smouldering candle. The anodized aluminum of the tubes was also quite shiny, especially at grazing angles, so the interior of both of the tubes were also lamp-blacked. Contrary to expectations, this lamp-blacking of a significant portion of the interior surface area of the target chamber did not noticeably affect the time required to evacuate the target chamber (except for the first time after application) or the ultimate pressure achieved. Application of the lampblacking reduced the scattered laser-light by about 20%.

The baffled tubes were designed, in effect, to collimate the scattered light from the primary sources but *not* the laser beam itself. The clear aperture of the baffles ($15mm$ diameter) was chosen to be about twice the maximum desired laser spot dimension ($8mm$), so as to ensure that they did not themselves become primary sources of scattered laser-light.

The entrance and exit windows, hereafter referred to as the Brewster windows, were oriented at the Brewster angle for transmitting vertically polarized light. The use of this angle was primarily to accommodate the dye laser beam which is greater than 96% vertically polarized. However, angling of the *exit* window at some angle about 45° is desirable in any case so as to prevent direct reflection of the laser beam back into the target chamber. It was thought that one could also vertically polarize the excimer beam before the final steering mirror so that subsequent, and presumably partially depolarized, scattered light would

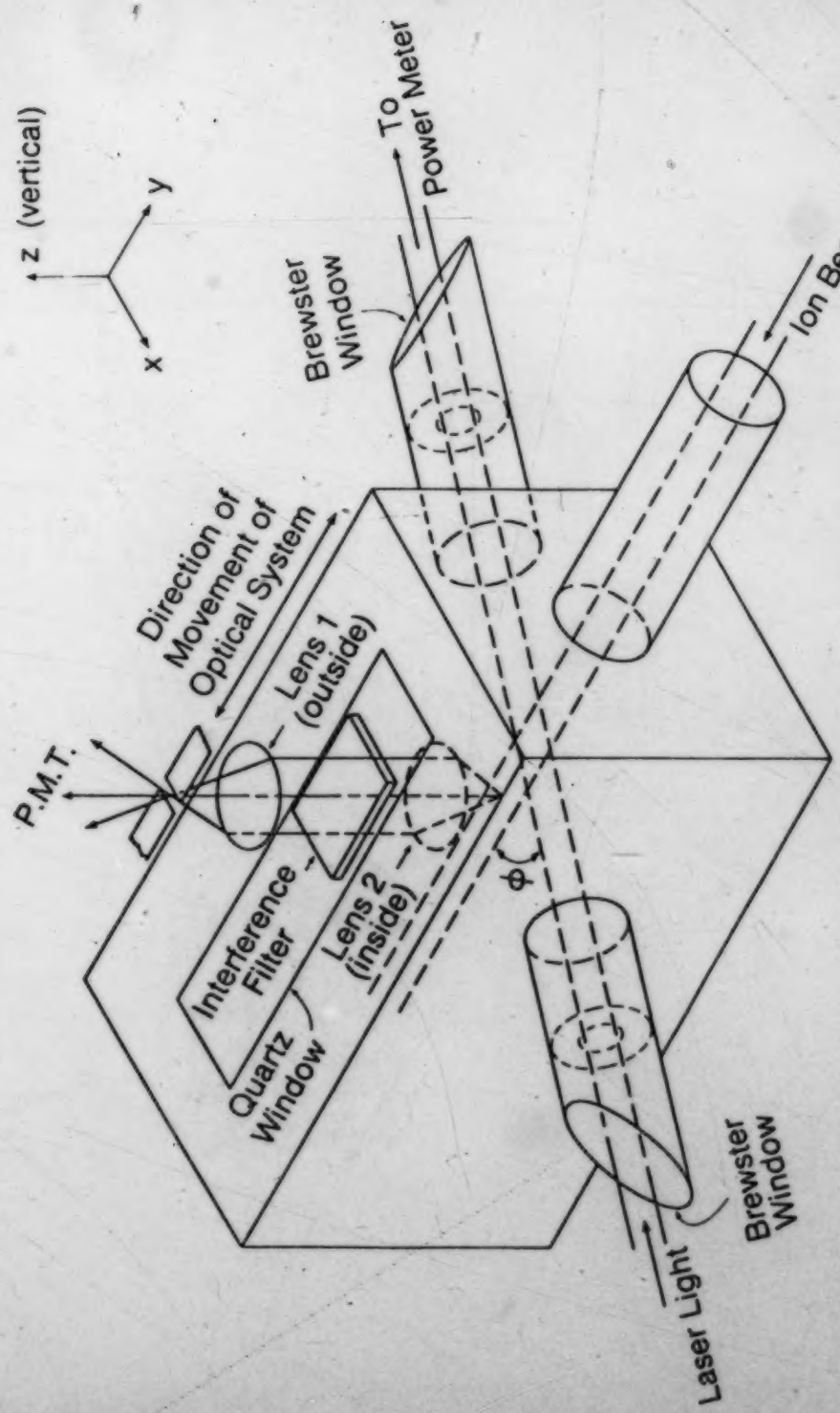

Fig. 3.1 Isometric schematic of the target chamber (not exactly to scale but about 1/4 actual size).

Fig. 3.2 Cross-section of the target chamber illustrating the optical isolation of the detection system from the Brewster windows and the other primary sources of scattered laser-light.

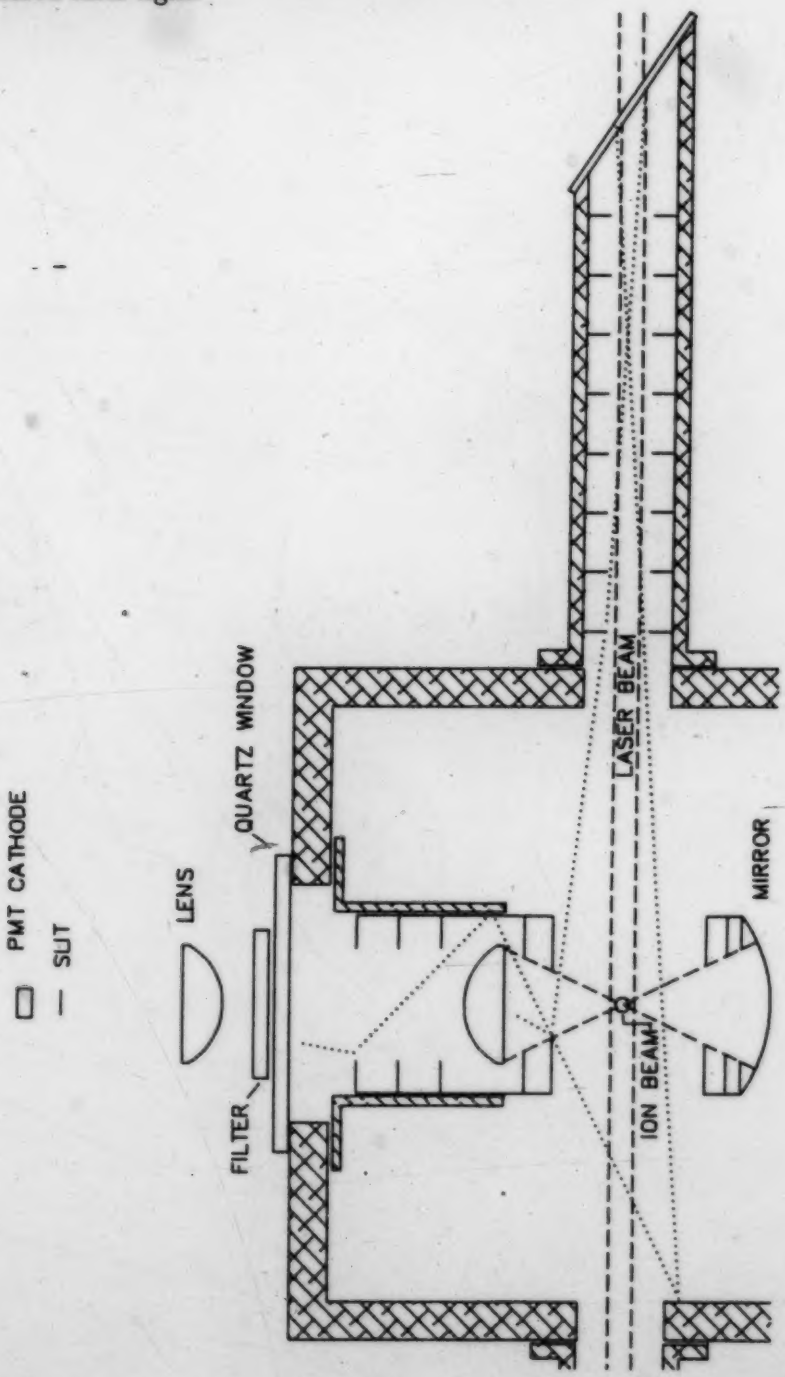

be reduced by passing through the Brewster window. Tests showed that this was not the case. The scattered light declined only in proportion to the reduction in intensity caused by the polarizer.

The Brewster windows were made from the highest quality (Suprasil 1 equivalent) synthetic fused silica, polished to a scratch-dig of better than 5–10. This ensured that the scattered laser-light due to the primary source closest to the detection system was at a minimum. The effect of using lower quality windows was not tested. However, the importance of the windows as a source of scattered laser-light was shown by the factor of ten reduction obtained by properly cleaning (single wipe with lens paper wetted with methanol) the apparently clean (to the human eye) windows.

Another indication of the relative importance of the entrance Brewster window, at least with the target chamber as designed, was the observation that removing the final steering mirror (which was thought to be a likely source of scattered laser-light) from about $10cm$ away from the Brewster window to $200cm$ away only resulted in a 5% reduction in the scattered laser-light.

It is also of interest to examine the role of air molecules as a source of scattered light. For example, for the sodium experimental configuration (i.e. observing very near the laser wavelength) a target chamber pressure of about $10torr$ resulted in greater than about $1cpp$ of scattered laser-light. This implies (with $\mathcal{E} \simeq 0.6 \times 10^{-5}$) about 20,000 photons from a laser pulse (2×10^{13} photons) over the approximately $1cm$ length defined by the slit height. At atmospheric pressure this corresponds to 2×10^{6} photons scattered per centimeter, or, 10^{-4}% per centimeter. This would have been a problem if it were not optically isolated from the detection system.

At the typical pressures inside the target chamber, about $10^{-6}torr$, the total scattered laser-light per laser pulse within the observation length is about

$10^{-5}cpp$, far less than the observed scattered laser-light. Thus, although the pressure inside the target chamber does set a lower bound on the scattered laser-light, in practice this is so low that other sources of scattered laser-light dominate.

The use of a narrow-bandpass interference filter in the detection system significantly reduces the scattered laser-light if the observed transition is more than a few filter half-widths away from the laser transition. The reduction is typically between a factor of 10 and 100, whereas the rejection ratio of the filters is about 1000. This indicates, as one might expect, a significant amount of scattered light due to fluorescence. This was the case for the titanium and IR–calcium experiments where the laser background was of the order of $10^{-3}cpp$. For the other experiments, the filter does not have as great an effect in reducing the scattered laser-light. However, a narrow-bandpass filter was needed to reduce the other major source of background signal: the ion-beam background.

The ion-beam background is caused by the excitation of all levels of the ions by the residual gas in the target chamber and vice-versa. Even with an appropriate filter in place, the ion-beam background was typically of $1000cps$ (ungated) for a $1\mu A$ beam at $10^{-6}torr$, except for the IR–calcium experiment where it was about one-tenth this value.

The ion-beam background can be reduced by lowering the target chamber pressure. For the titanium experiment a two-inch diffusion pump was mounted on the target chamber. This allowed an operating pressure of about $6 \times 10^{-6}torr$. Subsequently, a four-inch pump was acquired to reduce the pressure further and to provide the anticipated increased pumping speed required for the sodium experiment, which used a gas cell to populate the metastable level. The ion-beam background was also reduced by gating the detection system to as short a time as possible (see Chapter Five on data collection).

Laser beam optimization, which is discussed in the last section of this chapter reduces the scattered laser-light by about a factor of two.

3.2 Doppler Tuning

In order to use the fixed-frequency excimer radiation one has to allow for the possibility of Doppler tuning the laser frequency to the desired atomic transition. Having one small fixed angle, ϕ, between the ion beam and the laser beam optical path will give an adequate tuning range. However, an experiment which requires only a small Doppler shift to achieve resonance would then require that one uses a correspondingly small ion-beam velocity. This could result in a significant loss of time resolution and/or require one to use an accelerating voltage outside the optimal range for a particular accelerator. For example, if the titanium experiment had to be done at 45°, the required beam velocity would have been reduced by 60%. Thus it is desirable to have a range of angles available,

In this discussion it is assumed that, as indicated in the previous section, the target chamber is designed so as to allow the possibility of travel in either direction along the laser beam optical path. The minimum practical angle is about 45° since one wants to be able to start a decay curve as close to the interaction region as possible. An angle of 45° maintains a relatively well-defined interaction region along the ion-beam direction while still having a reasonably large Doppler shift. The design of the optical system is such that the slit defining the observation length and height can be rotated about the optical axis so that the slit is parallel to the laser beam (Fig. 3.3a). This allows one to start a decay curve immediately after the interaction region without the loss in signal that would result if the slit were perpendicular to the ion beam as is usually the case (Fig. 3.3b).

Rotating the slit as described also allows the equations used in Chapter Two to be used without any modification except to increase b to $b/\cos\phi$. Note

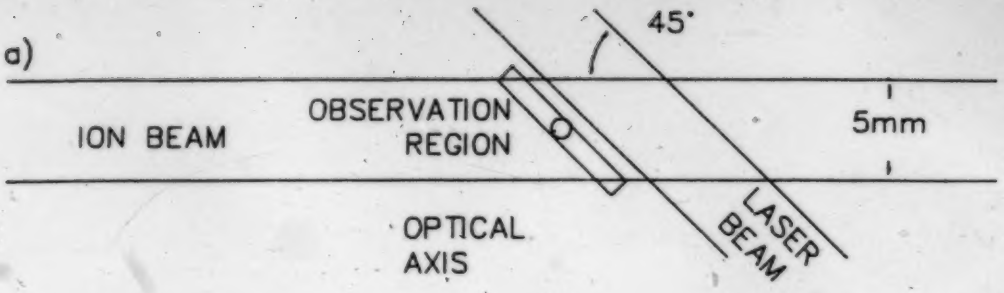

Slit rotated about the optical axis so as to be parallel to the laser beam.

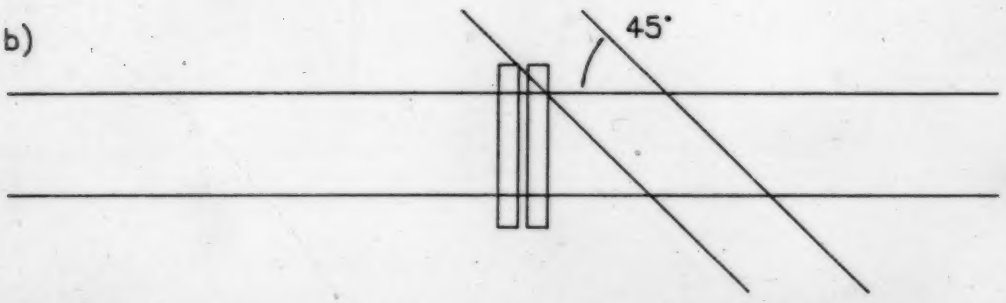

Slit perpendicular to the ion beam. The single-exponential decay curve starts further downstream than when the slit is rotated. Possible increase in laser scattered light unless slit displaced so as not to see laser path.

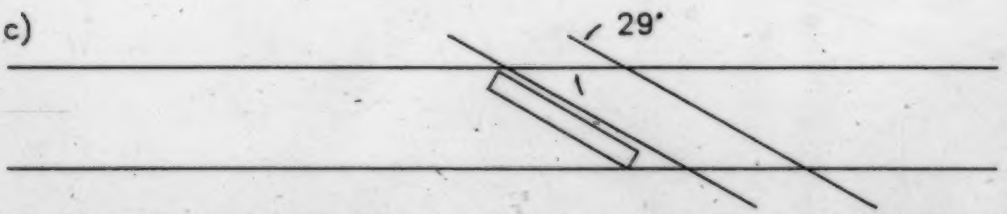

Angle between ion and laser beams too small to orient slit parallel to the laser beam.

Fig. 3.3 Illustration of the effect of various ion and laser beam geometries in relation to slit orientation.

that rotating the slit still does not allow ϕ to be made smaller than 45° (Fig. 3.3c). This is because the maximum useful slit height of less than $1cm$ is limited by the size($< 1cm$) and placement of the photomultiplier photo-cathode. The resulting observation region must easily encompass the whole ion beam ($\leq 5mm$ diameter) to avoid possible vignetting due to the inevitable misalignment of the optical system with the ion beam. At 45° the ion beam already fills almost 100% of the observation window.

Some consideration was given to designing a laser beam optical path with a continuously variable angle. However, this was judged to be more complicated than it was worth. Actually, since the XeCl excimer laser "line" consists of two very wide ($0.05nm$ FWHM), roughly equal intensity lines spaced $0.24nm$ apart, a continuously variable angle is not necessary. A reasonable compromise is to have three fixed optical paths (i.e. six ports) at 45°, 73° and 87° to the ion beam (Fig. 3.4). Only two baffled tubes are necessary and are bolted on to the appropriate ports while blanking off the unused ports.

The maximum angle of 87° was chosen to give the minimum Doppler shift required, about $0.12nm$, at the maximum velocity likely to be used for life-time measurements with our $350keV$ accelerator, about $3mm/ns$ for Li^+. The intermediate angle of 73° gives a Doppler shift roughly halfway between these two extremes.

Although Doppler tuning is not necessary when using the dye laser beam, it is convenient since it allows one to stay closer to the peak intensity of a given dye's tuning range. It also allows the possibility of using a filter or spectrometer to discriminate against scattered laser-light.

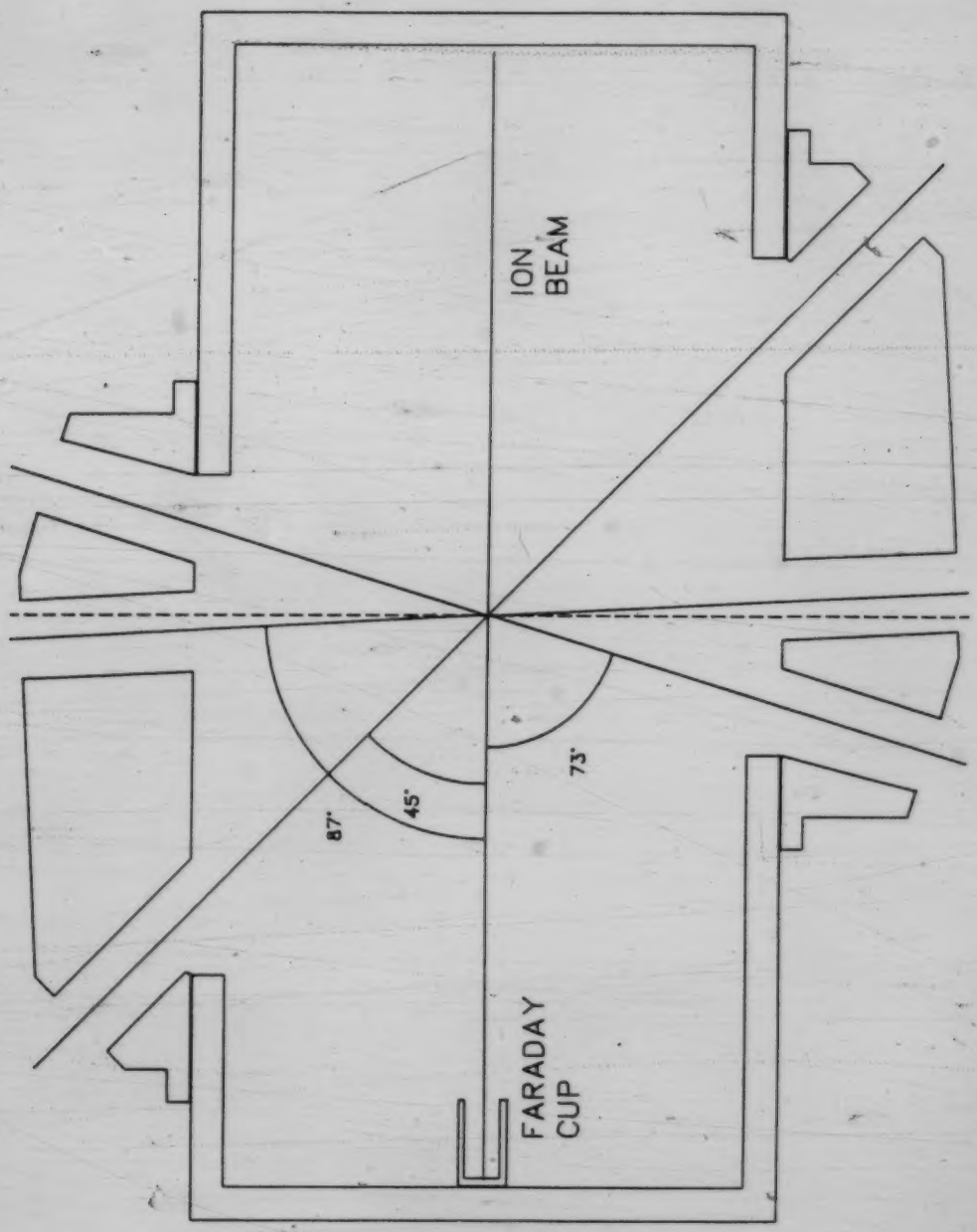

Fig. 3.4 Target chamber laser optical paths.

3.3 Detection System Optics

The main features of the detection system optics are shown in Fig. 3.2. The optical axis of the detection system is oriented perpendicular to the plane containing the laser and ion beams. Radiation from the ion beam is collimated by a plano-convex lens and leaves the target chamber via a large rectangular window (*cf.* Fig. 3.1). It then passes through an interference filter and is focussed by a second lens onto a $1mm$ wide slit oriented parallel to the laser beam and placed before the photomultiplier tube. The two lenses have equal focal lengths and thus this system defines a $1mm/\cos\phi$ observation width along the ion beam.

The spherical mirror shown in Fig. 3.2 can, in principle, almost double the collection efficiency. However, as it is another object near the laser beam path and reflects scattered light into the detection system, it causes a disproportionate increase in the laser scattered light. While some very low light situations might warrant a reduced signal-to-noise ratio, the mirror was not needed for any of the experiments described here. Instead it was replaced by a flat, black surface to serve as a constant backdrop for the ion beam as the optical system was moved along the ion beam direction. The large size of the baffled tube design made it very impractical to move the interaction region in order to obtain a decay curve. This does have some disadvantages which are discussed in the next section.

The window and the two lenses are of optical quality synthetic fused silica having a useful operating range from about $240nm$ to $2,000nm$. Experiments at shorter wavelengths would require replacing these with UV-grade synthetic fused silica. The distance from the flat surface of a lens to the slit (outside) or the ion beam (inside) can be adjusted by rotating the lens cell in its holder. The back focal length, i.e. distance from flat surface to the paraxial focus, as a function of wavelength is shown in Fig. 3.5. Also shown are specifications useful in adjusting the lens position for a chosen wavelength.

INSIDE LENS: flat surface sits 17.6mm from the bottom surface of the cell; beam line is 95mm from the bottom (inside) of the target chamber; thread of assembly is $24TPI = 0.94rev/mm$.

OUTSIDE LENS: when screwed all the way in, the flat surface is 32.2mm from the slit; thread pitch is $32TPI = 1.26rev/mm$.

MIRROR: has 50mm radius of curvature.

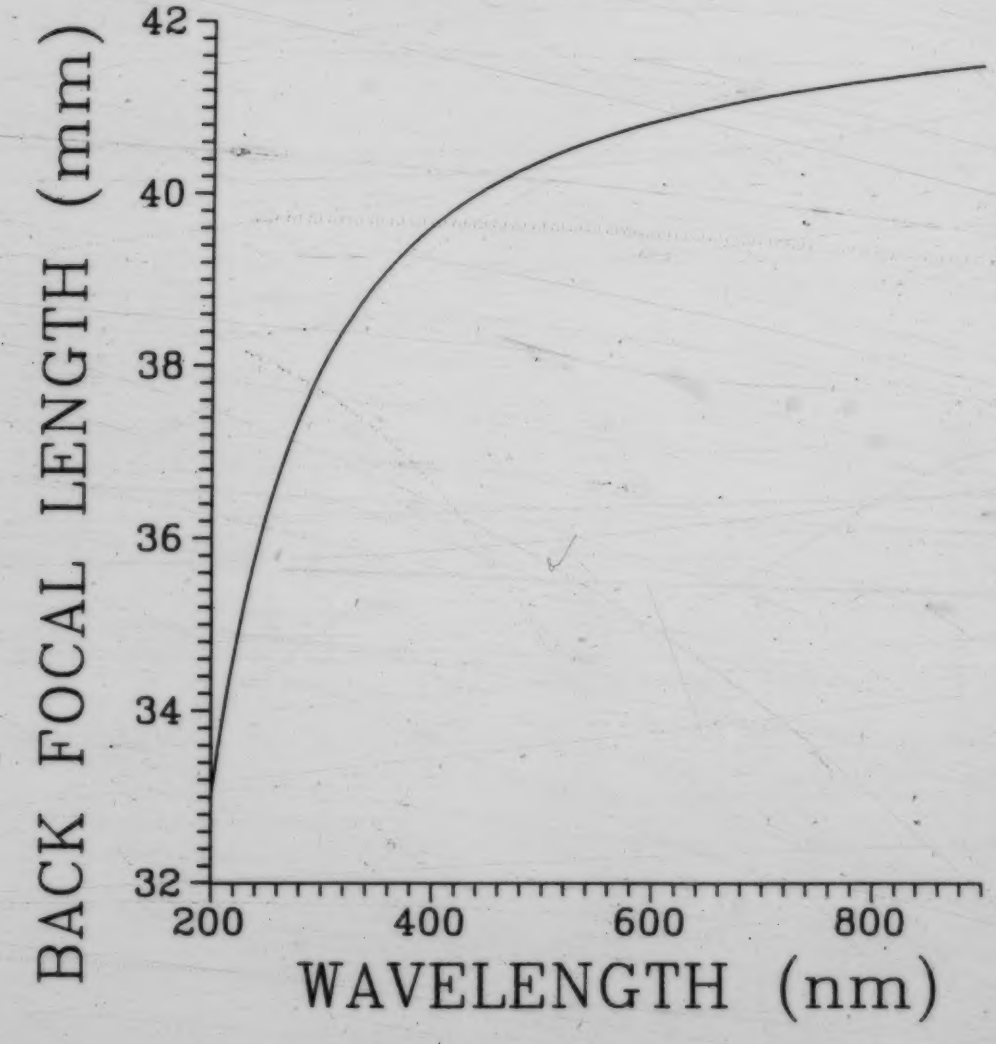

Fig. 3.5 Data for adjusting focusing of detection system optics.

The focussing properties of the optical system were modeled using a simple ray tracing technique: linear propagation plus Snell's Law at interfaces. This was done primarily to determine the actual effective aperture of the detection system. Once the effective aperture was determined, an aperture of corresponding size (14mm) was put in place so as to reduce scattered light further (see Fig. 3.6). The effective f-stop for the system at $430nm$ was $f/2$.

The model also indicated that a significant improvement in efficiency, about 20% overall, could be achieved by placing the inside lens $4mm$ closer to the ion beam than the value for the back focal length, f_b would indicate. This can be seen by comparing Figs. 3.7 and 3.8. One sees a 40% increase in the number of rays striking the photo-cathode in the latter case. This effect is due to using the lens system for optimal light collection rather than optimal image formation. The actual increase in detection efficiency was not measured.

3.4 Ion Beam–Optics Alignment

The movement of the detection system to obtain a decay curve does have some drawbacks. The first is the possibility of misalignment between the internal and the external drive screws. That is, although both are driven by the same stepping motor through an appropriate arrangement of gears and thus will travel the same distance, they may not be travelling in the exactly the same direction. Second, even if these two are parallel, they may not be parallel to the direction of the ion beam. Finally, the ion beam diverges slightly, on the order of tenths of a degree, as it travels down the target chamber. All of these imply that the inevitable variations in detection efficiency over the observation region of the detection system will result in some systematic change in *measured* intensity with changing position along the ion beam even if the actual total signal is constant.

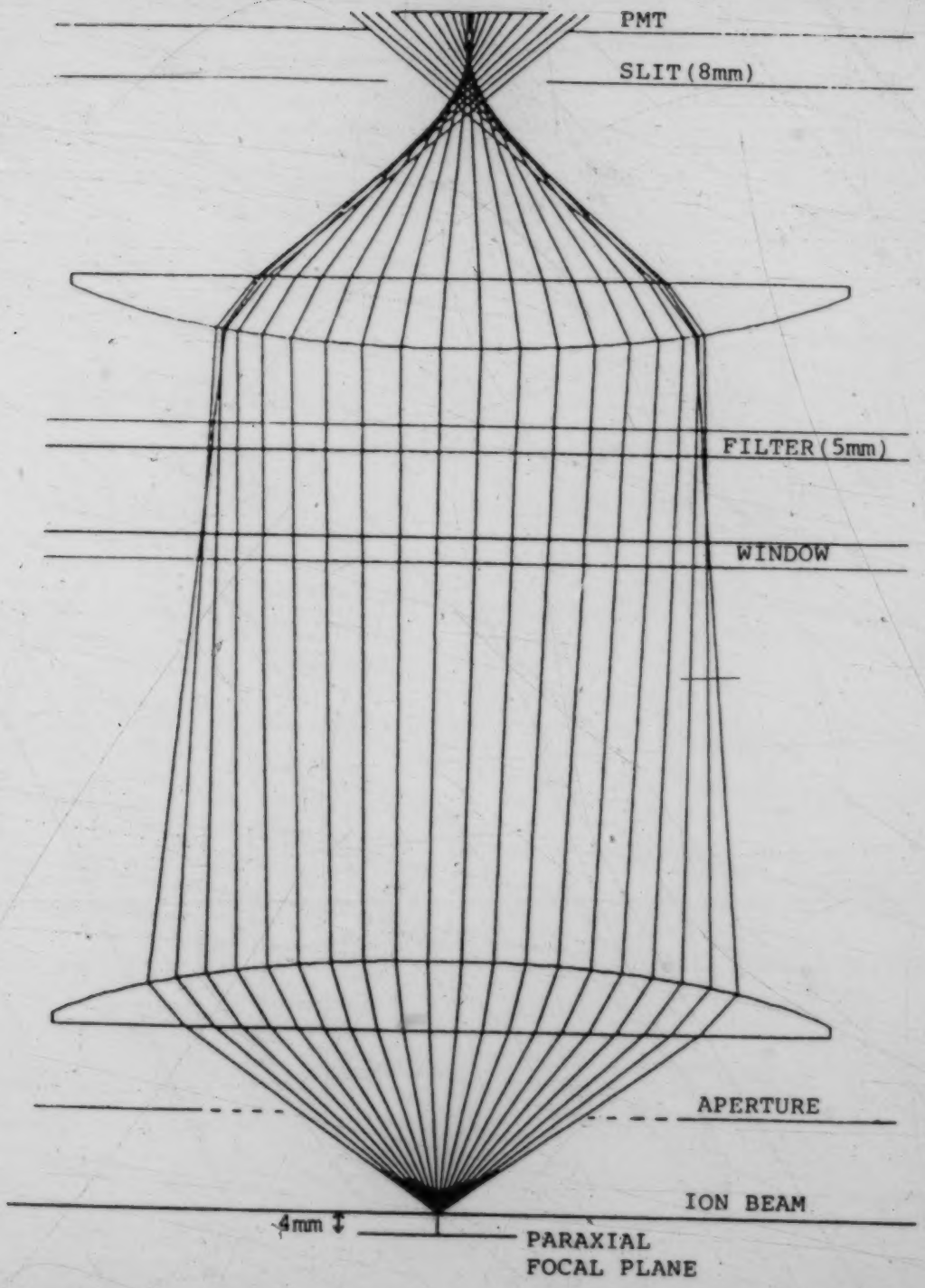

Fig. 3.6 Ray tracing of detection system optics. Note that vertical and horizontal scales are different. Dotted line shows the effective aperture of the system.

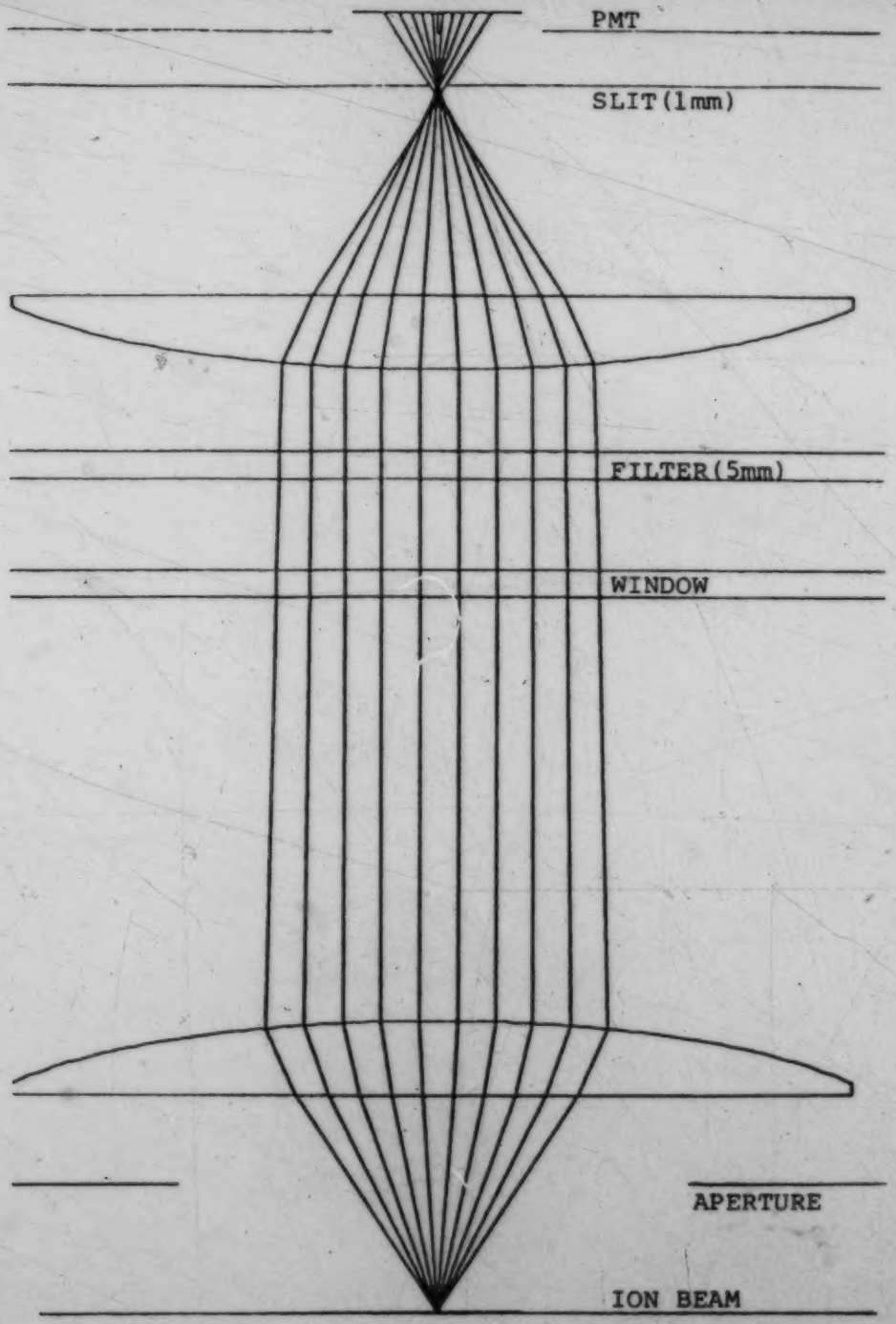

Fig. 3.7 Ray tracing of detection system optics with ion beam to lens distance equal to the back focal length, f_b. Note that vertical and horizontal scales are different.

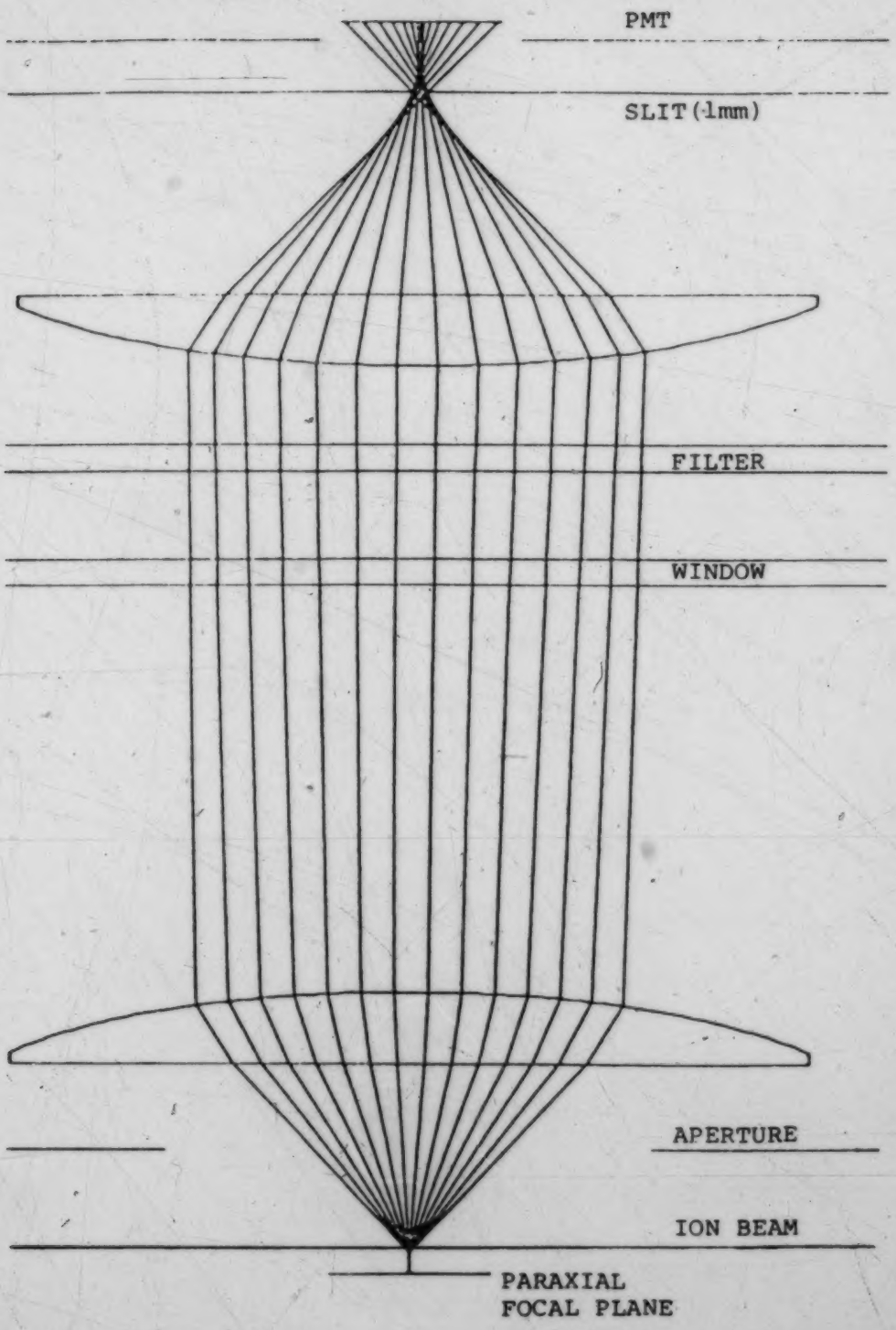

Fig. 3.8 Ray tracing of detection system optics with ion beam to lens distance equal to $f_b - 4mm$. Note that vertical and horizontal scales are different.

After aligning the system as described in Appendix II, the actual overall alignment can be tested operationally by measuring the ungated ion-beam background, normalized to the ion-beam current, as a function of distance from the interaction region. After the titanium experiment, a test using residual gas excitation of N_2^+ beam over $70mm$ showed no systematic variation at about the 0.2% level (see Fig 3.9.1a). This implies no worse than a $\pm 0.02\%$ variation over one titanium lifetime, $4ns$. More precise measurements over $12mm$ showed essentially no systematic variation, to better than $\pm 0.03\%$ over $12mm$, *if* the beam current was maximized by *both* moving the end of the target chamber and using the steering magnet. With the target chamber displaced until significant resistance was met and maximizing the beam current using the steering magnet only, a systematic decrease of at most 0.8% over $12mm$ (see Fig. 3.9.2c,d). This would correspond to at most a 0.3% apparent reduction in the titanium lifetime. This could be included as one of the sources of error for the lifetime.

The above alignment results were taken to indicate that when beam current was maximized by varying both the orientation of the target chamber *and* the steering magnet, the target chamber was more than adequately aligned with the ion beam. However, this proved to be true only at the 73° orientation for the slit as used in the titanium experiment. After doing the 3968 calcium experiment, a large systematic decline of 2% over $14mm$ was found. This was also the minimum systematic decline that could be obtained by varying the orientation of the target chamber. The cause of this apparent loss of alignment was later attributed to the fact that the ion beam, when viewed through the slit oriented at 45° "fills" the entire observation region. A small misalignment will have a very much greater effect in this case than for a beam that only "half-fills" the observation region.

Divergence of the ion beam of about 0.4° FWHM would cause a 0.6% decrease in intensity over $14mm$ if the observation region were filled. The uncertainty

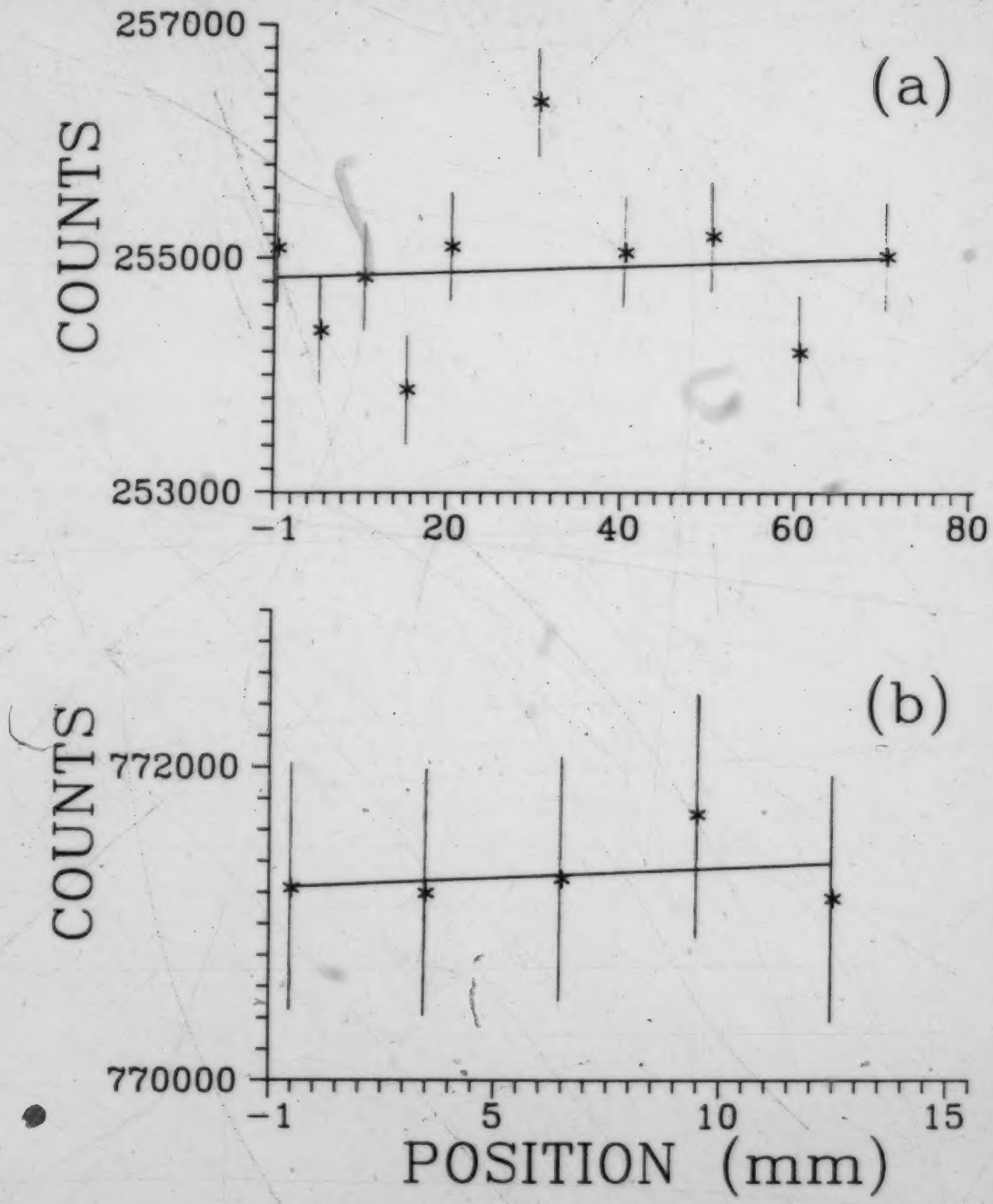

Fig. 3.9.1 Variation of the ungated beam background (UBB) normalized to beam current as a function of distance from the interaction region. (a) done with target chamber in same position as titanium experiment and (b) done with optimized alignment.

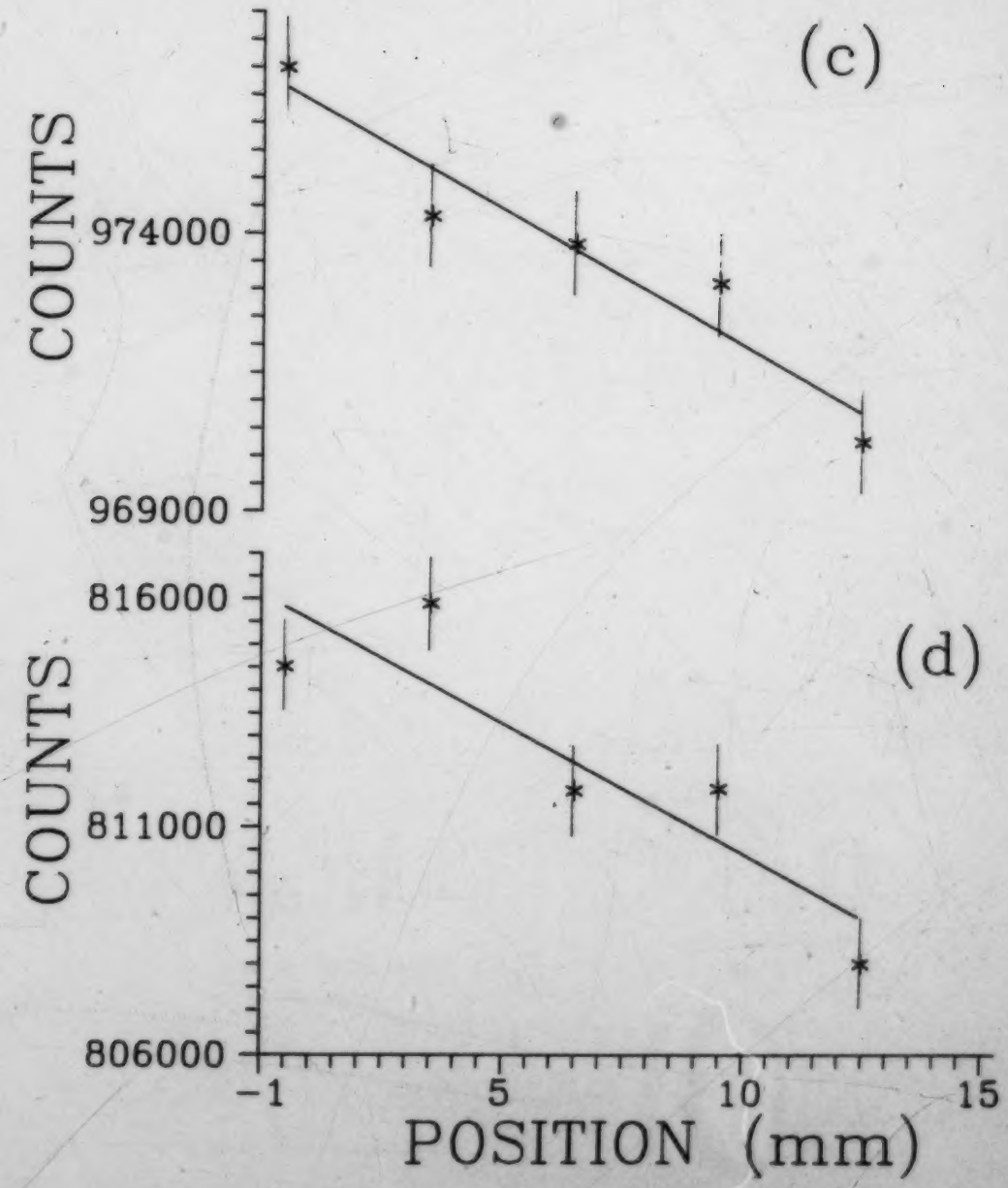

Fig. 3.9.2 Variation of the ungated beam background (UBB) normalized to beam current as a function of distance from the interaction region. (c) and (d) done with end of target chamber displaced a few millimeters.

in the alignment procedure followed in §3.4.1 was accurate to only about $\pm 1mm$ over $200mm$. This alone could cause a maximum of 1.8% decrease over $14mm$. These two effects combined easily account for the observed "misalignment". The problem could be compensated for by using the ungated beam background (UBB) rather than the integrated beam current to provide the necessary normalization of the observed signal to the number of ions viewed by the detection system.

The cause of the apparent "misalignment" problem was not determined until after the calcium experiments were done. Although the calcium experiment did not have to be done with the slit oriented at 45° to the ion beam, the sodium experiment used the UBB scaling technique (see Chapter Five). Thus it was advantageous to do the calcium experiment with the UBB scaling as well so as to have a possible means of judging the merits of this scaling method. It is also worth noting again that, although it would have been relatively easy to increase the slit height to $1cm$, this would not have completely solved the problem since the slit–PMT distance and the use of a one-inch filter have essentially the same effect on the height of the observation region as having an $8mm$ slit. This was especially true for the IR-calcium experiments where the PMT photo-cathode was about $4cm$ away from the slit (although a third lens was placed between the slit and the PMT to reduce the light loss).

3.4.1 Initial Alignment Procedure

All parts of the detection system and drive mechanism are attached to the removable target chamber lid. The laser entrance and exit tubes are attached to the sides walls and the vacuum pump to the bottom of the chamber. The shielded Faraday cup and ion-beam entrance aperture (4 or 5 mm in diameter), which define the ion-beam path in the target chamber, are attached to the front and back walls of the target chamber. The interior optical system is bolted onto

a monolithic slab on wheels which is driven along two tracks by the interior drive screw. The exterior optical system, including the photomultiplier tube, is mounted on a wheeled cart which is driven along two tracks by the external drive screw. Both drive screws are driven by the same stepping motor. A procedure for carrying out the alignment of the interior and exterior optical systems is suggested in Appendix II.

3.5 Laser Beam Optimization

This section describes the laser beam delivery system and the methods used to optimize the laser beam so as to produce the minimum scattered light possible. All that was needed for the IR-calcium experiment, where the observation wavelength was over $400nm$ from the excitation wavelength, was to place a defining aperture (about $4 \times 6mm$) before the last steering mirror. This simple arrangement produced very low levels of scattered light, almost negligible compared with the decay signal obtained with the $10\mu A$ calcium beam. However, experiments where the observation wavelength is near the laser wavelength and/or small effective ion beam currents must be used, the quality of the laser beam is more critical. The beam delivery system used for the excimer laser experiments is shown in Fig. 3.10.

The laser spot size was determined by placing a defining aperture (about $3 \times 6mm$) before a primitive spatial filtering system. Two plano-convex lenses collimate the beam while a small pinhole (about $250\mu m$ diameter), placed at their mutual focal point, partially filters scattered light from the defining aperture. Any subsequent apertures do not touch the laser spot. They serve only to reduce any remaining flare or halo surrounding the spot. The reduction of the flare and halo surrounding the spot is very pronounced when compared to the same situation with the spatial filtering system removed. The measured scattered light with the

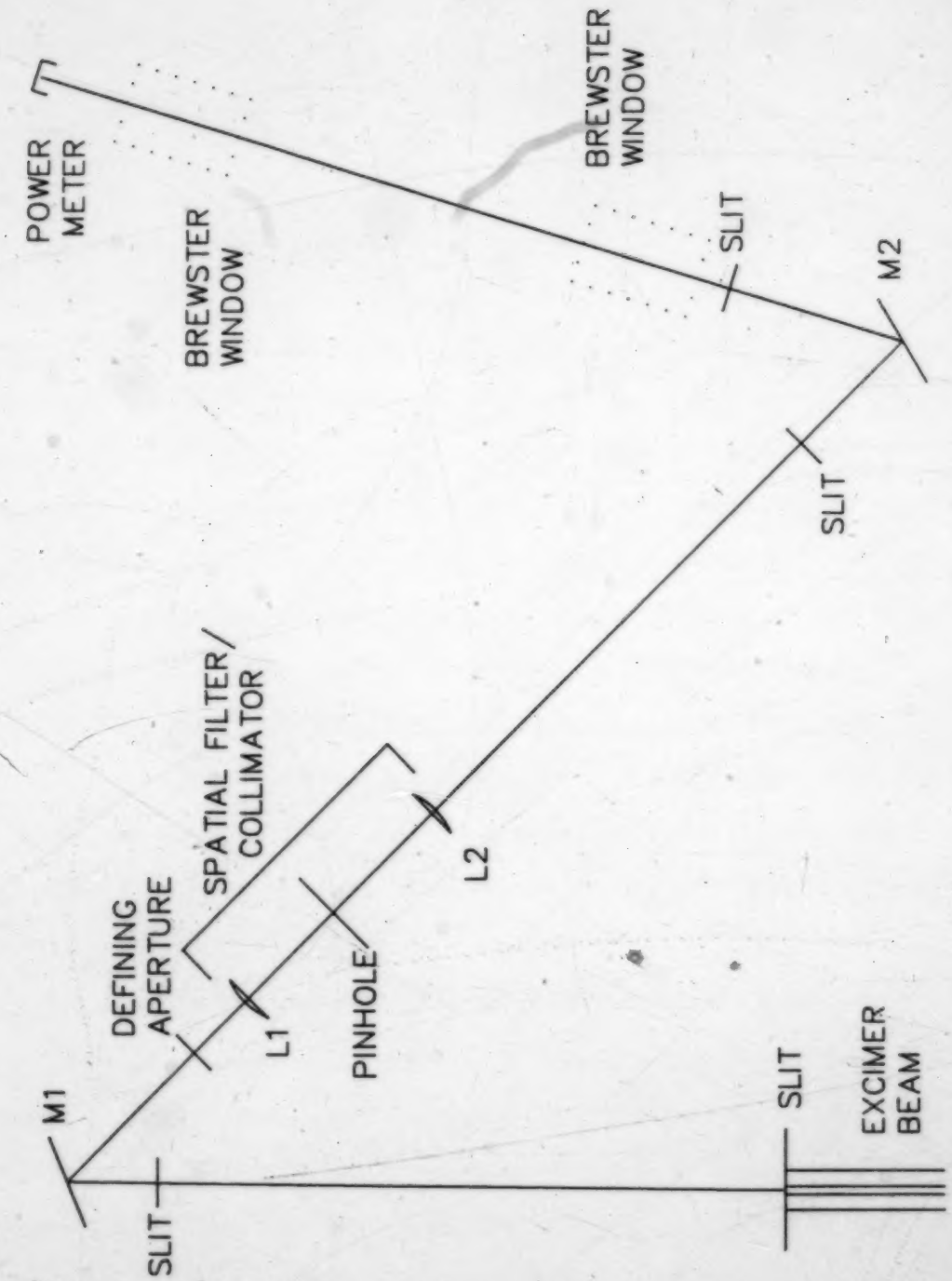

Fig. 3.10 Schematic of the excimer laser beam delivery system.

detection system looking at the interaction region was reduced by about about a factor of two using the filtering system.

There is about a 20% loss in power in the beam, as measured after going through the target chamber, due to the presence of the pinhole. The laser spot was a very sharply defined rectangle with the pinhole in place and a very fuzzy one without it. Note that the power loss going from excimer port to the interaction region is quite substantial, only about 1% of the initial beam power reaches the power meter after passing through the target chamber. The primary source of loss ($> 90\%$) is due to the defining slits before the collimating system. Most of the remainder is due to the large divergence of the excimer beam ($6 \times 2.5mR$) before the defining slit and reflection of 30% of the horizontally polarized component of the beam at the Brewster window. As discussed in the previous chapter, this power was adequate to saturate the transition and since the scattered laser light is proportional to the power in the beam, this low efficiency delivery system was appropriate for these experiments using the excimer laser.

The excimer laser used for these experiments was a Lumonics TE-860 operated on XeCl. The quality of the excimer laser beam deteriorated significantly near the end of the excimer fill cycle. This was shown by an increase (typically more than 20%) in the mean scattered laser-light level when the laser power dropped to less than half its peak value. The half-power point of the laser occurred after about two million pulses or about three hours of operation at $200pps$. For all but the IR-calcium experiments, the excimer was refilled at least every four hours of operation. For the IR-calcium experiment, the low scattered laser-light levels combined with the high initial power levels allowed running for up to ten hours without a refill.

The excimer-pumped dye laser, Lumonics EPD-330, used in the calcium experiment was operated at $200pps$ using a PBBO dye solution. Tuning the dye

laser to the desired wavelength for the calcium experiments was facilitated by the use of a spectrometer with a linear optical diode array replacing the exit slit. Light from the dye laser beam and a neon lamp were directed onto the spectrometer entrance slit. The output of the diode array electronics to an oscilloscope enabled one to view a complete spectrum over about 80Å (in first order) for any particular spectrometer setting. The separations between several neon lines about 7943Åwere measured on the oscilloscope (in milliseconds) to obtain a calibration curve to convert between milliseconds and Ångströms. With the dye beam (about 395nm) viewed in second order, the wavelength could be set to about $\pm 0.005nm$. Fine tuning of the dye wavelength to the atomic resonance was done by maximizing the signal obtained using the calcium atomic beam. The observed width of the resonance was typically about 0.008nm (FWHM).

CHAPTER FOUR

ION-BEAM PRODUCTION

This chapter outlines the methods used to produce the ion beam required for each of the three experiments. The ion beam was produced using a $350keV$ accelerator equipped with a Danfysik 911A hollow cathode ion source. Good alignment of the the ion source with the extraction electrode of the accelerator column was required to obtain an adequate beam current. This was not easy to do consistently as the alignment was sensitive to how the ion source was reassembled after replacement of the filament and cleaning of the components. Although this alignment could be visually checked without running an ion beam by use of a telescope focussed on the source aperture, this could only be done once the filament was hot.

The temperature of the ion source oven is controlled by the proximity of the oven to the filament. In order to obtain a stable, long-lived ion beam it was necessary to push the oven in very slowly until the desired beam current was reached. Both argon and krypton were used as carrier gases.

The beam line within the target chamber was defined by the $8mm$ diameter aperture of the Faraday cup and $5mm$ diameter aperture (or smaller, see below for details) at the entrance to the chamber.

4.1 Titanium Beam

The Ti^+ beam ($v = 0.979mm/ns$) was typically $3\mu A$ over a $5mm$ area, measured at the shielded Faraday cup at the end of the target chamber. This unusually large beam current for a low energy Ti^+ beam was obtained by using $TiCl_3$, m.p.=440°C, b.p.=660°C, in the ion source oven. Using argon as a carrier gas worked better than krypton, but a 4:1 Ar:Kr mix produced the stablest and highest current ion beam.

The use of $TiCl_3$ presented a couple of difficulties. First, the beam current was found to be extremely sensitive to the temperature (as well as the physical and chemical condition) of the material in the oven. The position of the oven had to be continually adjusted in order to maintain a stable beam current. $TiCl_3$ is extremely hygroscopic and will decompose within minutes on exposure to room air. This necessitated filling of the oven under a dry atmosphere and rapid transfer of the filled oven to the ion source vacuum. Despite the precautions of opening the bottle of $TiCl_3$ in a dry atmosphere and storing it in an airtight container, it became contaminated by water vapor over a couple of months. After contamination it was impossible to obtain a beam current of greater than $1\mu A$.

Second, the chlorine rapidly deactivated the filament and the titanium and its chlorine compounds coated the ion source parts causing short circuits to occur. The ion source components usually had to be replaced or refurbished after about six hours of operation. This made obtaining a titanium beam a very time consuming operation due to the difficulty of aligning the ion source with the extraction electrode as mentioned above. These problems were outweighed by the intensity and stability of the titanium beam achieved.

4.2 Calcium Beam

The Ca^+ beam ($v = 1.099mm/ns$) used was typically between 10 and $15\mu A$ although beams of up to $20\mu A$ were obtained. This was done with calcium metal in the oven with krypton as a carrier gas. Most of the runs were done with a $5mm$ diameter ion beam; however, after the source of the "misaligment" problem was determined, the aperture at the entrance of the target chamber was replaced with a $3 \times 4mm$ rectangular aperture. This reduced the typical beam current to about $9\mu A$.

4.3 Sodium Beam

As mentioned in Chapters 1 and 2, the sodium experiment was more difficult than the others in that a two stage excitation process was required. The first stage of excitation was the population of the metastable level (see Fig.1.4) by means of a gas cell. A schematic of the gas cell is shown in Fig. 4.1. Since only a small fraction of the ions leaving the gas cell were expected to be in the appropriate metastable level, it was essential to achieve the maximum possible beam current. However, the gas cell itself makes it difficult to obtain large beam currents at the Faraday cup. This is due to the series of small apertures (two 4mm and one 5mm) within the gas cell, in addition to the 5mm aperture in the target chamber. The presence of the gas cell in the beam line reduced the maximum obtainable Kr^+ beam from over $20\mu A$ to about $4\mu A$. This situation was considerably improved by a re-alignment of the ion-beam line after the steering magnet. The realignment of the beam line resulted in a factor of three improvement in the krypton ion-beam current.

The Na^+ beam ($v = 1.531 mm/ns$) used was typically about $10\mu A$ with the gas cell in operation, although a maximum of $15\mu A$ was obtained. It was produced using sodium chloride in the oven and krypton as the carrier gas. The pressure in the gas cell was typically about $0.5 \times 10^{-3} torr$. The operational pressure of the gas cell was determined by increasing the pressure (by opening the leak valve) until the ungated beam background stopped increasing. This peaking of the UBB with increasing pressure was due to the increasing population of the metastable level being counteracted by a significant decrease in the Na^+ beam current as a greater fraction of the ion beam was neutralized by the gas cell. Spectroscopic analysis of the beam background within the passband of the interference filter used in the experiment showed that it was entirely due to transitions to the

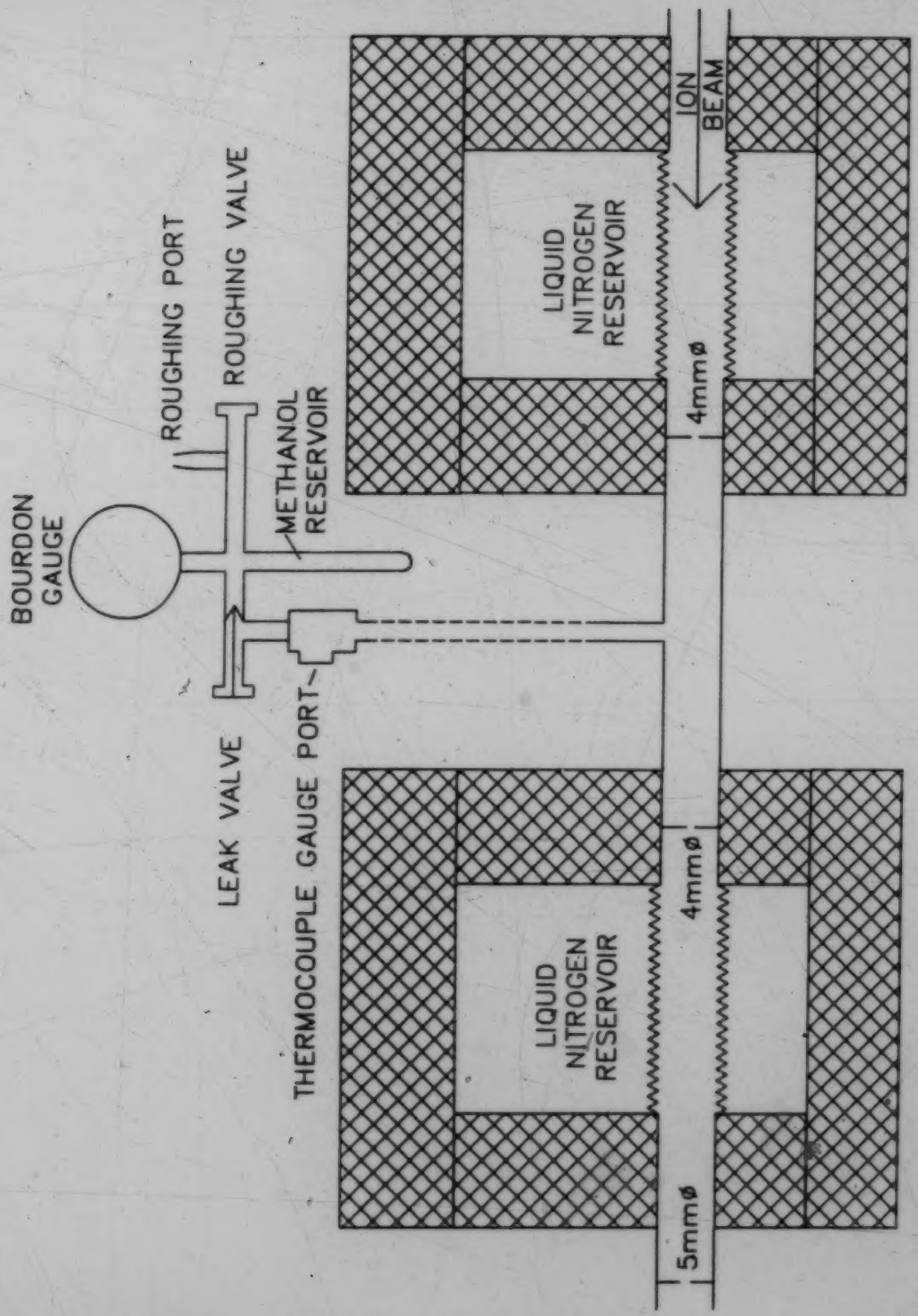

Fig. 4.1 Illustration of the gas cell used for the sodium experiment.

level that was to be populated by the gas cell. Thus the UBB could be used as a monitor of the efficiency of the gas cell. The operation of the gas cell caused a slight increase (< 20%) in the pressure in the target chamber and a larger increase (< 50%) at the diffusion pump before the gas cell. The effective beam current, i.e. number of atoms in the metastable level, produced by the gas cell was surprisingly stable, as shown by a small, linear decline in the UBB during each sweep. The gas cell occasionally became unstable with factor of two changes in the gas cell pressure for periods of five to ten minutes. Although these fluctuations did not seem to adversly affect the shape of the decay curves (due to the effectiveness of the UBB normalization), data taken during these periods were discarded.

4.4 Velocity Calibration

The actual quantity obtained directly from the decay curves is the decay length at the ion-beam energy at which the experiment was performed. No matter how accurately the decay length is measured, the accuracy to which the energy (velocity) is known sets an absolute limit on the accuracy of the lifetime itself. Although the "accelerating voltage" or "dial energy" can be set to $\pm 0.2keV$, the actual energy of the ions is only known to $\pm 1\%$. The conversion factor for converting dial energy into ion-beam energy is given by the upper calibration curve in Fig. 4.2.

The old calibration curve was inappropriate for these experiments for several reasons. First, during the course of some other (beam-foil) experiments, it appeared that foil thickening was having a significant effect on the observed lifetimes. Subsequent tests which monitored the increasing foil thickness with time using the Doppler shift technique [AP84], showed a doubling of the energy loss in the foil ($2.5\mu g$) over a one hour period. The old quantum beat measurements did not account for any possible thickening of the foil and thus probably underestimated the calibration factor.

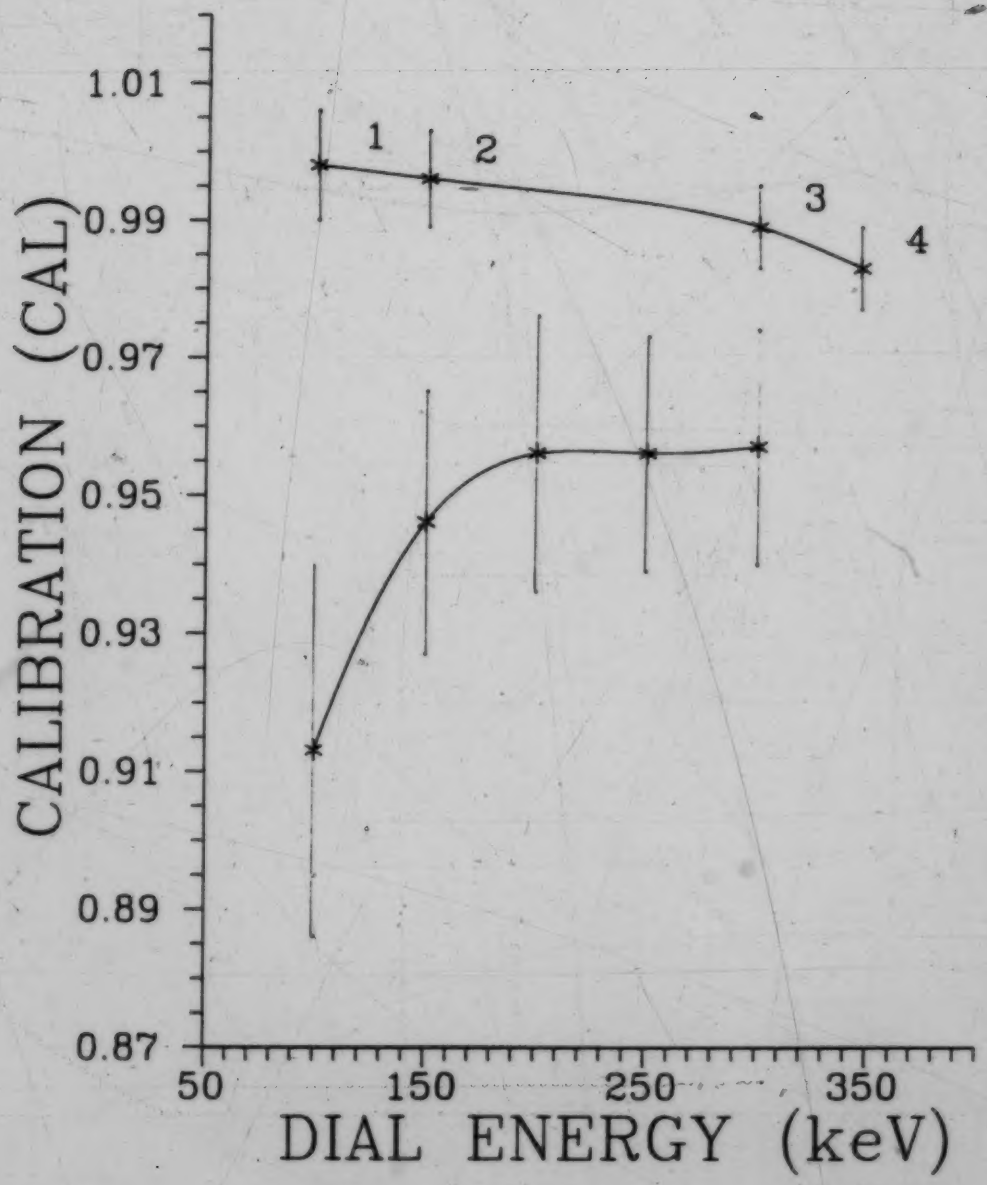

Fig. 4.2 Energy calibration curves for 350keV accelerator. The lower curve was done using quantum beats to obtain the ion-beam velocity. The upper curve was obtained using the Doppler shift method for points 1,2,3 and the nuclear resonance method for point 4.

Second, the old measurements were done with the accelerator in a different configuration than the present one. Formerly the dial voltage gave the nominal voltage on the accelerator column only, the total accelerating voltage being given by the dial voltage plus the extraction voltage. Presently, the accelerator is configured so that the dial voltage is the total accelerating voltage.

Third, the uncertainty of about $\pm 2\%$, giving an uncertainty in the velocity of 1%, was larger than what one should be able to obtain using the Doppler shift technique.

The Doppler shift measurements were then done (also using helium) and showed the expected increase in the calibration factor (closer to 1) as suggested by the foil thickening problem. However, although the difference between the two curves corresponds to a constant energy difference of about 8 or 9keV, the size of this difference is about four times larger than expected if thickening is independent of foil thickness and beam current. It is possible that the remaining difference can be attributed to the differing accelerator configurations and/or some systematic error in either set of measurements. In order to differentiate between these two possibilities, a third method was used to measure the energy at one particular energy.

The $(p, {}^{19}F)$ nuclear resonance reaction [Ma66] at 340.46keV provided a calibration point that indicated that the upper calibration curve was the correct one to use, at least with the accelerator in the present configuration.

CHAPTER FIVE

DATA COLLECTION AND ANALYSIS

5.1 Data Collection

The signal from the photomultiplier tube was amplified, digitized and stored in a TN-11 data processor that has been described previously [PG79]. Each data set was accumulated using the multi-scaling technique in which several successive sweeps are summed. Each decay curve contained a total of between twenty to thirty data points. The accumulation time for each point was typically between six and ten seconds, half of which is spent measuring the background signals present with the ion beam turned off. This process makes the data collection process more efficient since if any problems arise only one sweep rather than the whole data set is lost. In addition, multi-scaling also reduces the effect of any systematic time variations in the signal. Usually the decay curves were taken by moving downstream from the interaction region by 0.5 or $1mm$ steps. A few data sets were taken in which the data were taken in the opposite direction, *i.e.* start in the tail and step towards the interaction region. The "forward" and "backward" data sets showed no systematic differences in the lifetime obtained, at least at about the 1% level.

Although most of the data were taken as indicated above, a modified procedure was used for the last (IR) calcium data sets. Systematic variations with time can be essentially eliminated by recording data both in the "forwards" and "backwards" direction for each sweep, *i.e.* each decay curve would contain twice as many points and the forward and backward components analyzed separately and then summed and reanalyzed. This method also has the advantage of separating systematic time variations (*e.g.* declining beam current) from systematic variation with position (*e.g.* alignment problems).

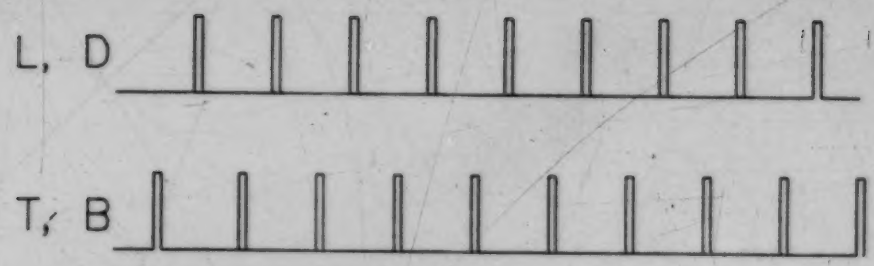

Fig. 5.1 Gating sequence of data accumulation.

5.1.1 Background Signals and Gating

A short gating pulse, synchronized with the laser pulse, was used to discriminate against detector dark counts, ion-beam background and fluorescent scattered laser light. The length of the gating pulse was made large enough to allow for time-jitter in the start of the laser pulse ($\pm 10ns$), decay curves of at least three mean-lifetimes long and the longest rise-time of the electronic components. In all cases the gating pulse was short enough so that the detector dark count rate was negligible ($< 2 \times 10^{-5} cpp$).

At each point of the decay curve the signal was accumulated for a fixed time (*i.e.* a fixed number of laser pulses) for each of the following conditions:

(T) laser beam on, ion beam on (Total signal),

(B) laser beam off, ion beam on (Beam background),

(L) laser beam on, ion beam off (Laser background),

(D) laser beam off, ion beam off (Dark counts).

Signals B and D were recorded between laser pulses and the ion beam was turned "off" with a mechanical chopper. The corresponding gating sequence is shown in Fig. 5.1. In addition to these data, either the integrated, digitized ion-beam current, or, the ungated ion-beam background was recorded during the same fixed time as T and B.

The statistical fluctuations in the decay signal caused by a large laser background can in principle be reduced by the technique of *delayed gating*. This

involves measuring the decay signal far enough downstream from the interaction region so that the "decay photons" arrive at the detector much later ($\geq 20ns$) than the photons due to laser scattered light. The gating pulse can then be suitably delayed so as to discriminate against the scattered light. This technique was used for one series of the calcium measurements. No improvement in the data was observed, however, because of irregularities in the firing of the laser, which rendered it impossible to determine accurately the exact number of laser pulses that were seen by the detection system. This number is needed to adjust the observed count rate to account for missed counts due to the fact that our apparatus could only record zero or one count for each laser pulse (see §5.2.1) The consequent uncertainty in this "pile-up correction" cancelled any gain in accuracy that would have resulted from the lower laser background. In order to take advantage of this technique of delayed gating it would be necessary to use another data channel to record the total scattered laser light as well as the "delayed" scattered laser light so as to determine the effective laser pulse rate (*cf.* discussion in §5.2.1 of a similar effect due to a high ion-beam background).

5.1.2 Normalization

The decay signal was normalized to account for variations in the (observed) population of the lower state of the excitation transition. This variation was principally due to fluctuations in the beam current. The beam current(I) or the ungated beam background(UBB $\geq$ 10,000 counts per second) was used to effect this normalization. The beam current method was used when the only significant source of population variation was due to fluctuations in the beam current. However, in the sodium experiment, variations in the gas cell conditions also caused fluctuations in the lower (metastable) level population and the UBB

method was used for normalization. It also provided the additional benefit of correcting for any optical system/ion-beam misalignment.

The magnitude of the needed correction was restricted by repeating the measurement for any data point where N changed by more than 10% from some preset value. The typical maximum change in the signal required by the normalization of the final decay curve was less than 5%.

5.2 Data Analysis

This section describes how the raw data is converted into the number of counts corresponding the the single-exponential fluorescence decay curve as well as the error in the number of counts. It also describes the fitting procedure used to obtain the decay length .

5.2.1 Single-Photon Counting Pile-up Correction

The electronics used to generate the TTL pulses (i.e. "counts") for input into the TN-11 scalars could only distinguish PMT pulses more than $600ns$ apart. Thus , if two (or more) such PMT pulses occurred due to one laser pulse, the system would register only one count.

This all or nothing counting clearly underestimates the actual number of PMT pulses which is what one actually wants to count. This effect was taken into account by using an commonly accepted procedure (as in [KKW78],[AIP85]) to calculate the number of missing counts. This correction can be obtained by considering the probability of arrival of more than one photon during the gate corresponding to one laser pulse. The observed number of counts per laser pulse (i.e. the count rate, r) is given by

$$r = \sum_{x=0}^{\infty} (\textit{no. of counts for } x \textit{ PMT pulses}) \times (\textit{probability of } x \textit{ PMT pulses}).$$

The PMT pulses follow the Poisson statistics of the source(s) of the radiation; fluorescence decay and/or laser background and/or ion-beam background, as long as the response of the PMT to the radiation is linear. Thus the probablility of the occurrence of x PMT pulses when the mean number is μ is given by the Poisson distribution:

$$P(x,\mu) = \frac{\mu^x}{x!}e^{-\mu}, \quad x = 0, 1, 2 \ldots \infty.$$

Thus if there is no pile-up one gets the expected result

$$r = \sum_{x=0}^{\infty} xp(x,\mu) = \mu.$$

However, with pile-up the number of counts observed for x PMT pulses is given by the unit step function

$$U(x) = \begin{cases} 0, & \text{for } x = 0, \\ 1, & \text{for } x \geq 1. \end{cases}$$

$$\text{Therefore} \quad r = \sum_{x=0}^{\infty} U(x)P(x,\mu) = \sum_{x=1}^{\infty} P(x,\mu) = 1 - e^{-\mu};$$

$$\text{or,} \quad \mu = -\ln(1-r). \tag{5.2.1}$$

A measurement of the count rate, r, requires observing the total counts, C, for a large number, P, of laser pulses. However, the actual PMT pulse rate, μ, is not constant while this measurement is done due to the unavoidable small fluctuations in the beam current. Thus eqn. 5.2.1 only applies to one particular laser pulse (or at least pulses done under identical experimental conditions, which cannot be provided). To make this explicit, eqn. 5.2.1 can be written as

$$\mu_i = -\ln(1-r_i).$$

The desired quantity, C', is the actual number of PMT pulses obtained from the P laser pulses:

$$C' = \sum_{i=1}^{P} \mu_i = -\sum_{i=1}^{P} \ln(1 - r_i) = -P\langle \ln(1 - r) \rangle. \tag{5.2.2}$$

However, one can only measure $\langle r \rangle = C/P$, where C is the number of counts recorded in P laser pulses. This leads to the usual pile-up correction:

$$C' \approx -P \ln(1 - \langle r \rangle) = -P \ln(1 - C/P). \tag{5.2.3}$$

How good an approximation eqn. 5.2.3 is to eqn. 5.2.2 can be determined by expanding the two logarithmic terms in a power series and comparing the resulting expression term by term.

$$\begin{aligned} C' = P\langle r + \frac{r^2}{2} + \frac{r^3}{3} + \ldots \rangle &= P\left[\langle r \rangle + \frac{\langle r^2 \rangle}{2} + \frac{\langle r^3 \rangle}{3} + \ldots\right] \\ &\approx P\left[\langle r \rangle + \frac{\langle r \rangle^2}{2} + \frac{\langle r \rangle^3}{3} + \ldots\right]. \end{aligned}$$

Since $\langle r^n \rangle$ is greater than $\langle r \rangle^n$ for any n, the approximation underestimates the actual correction required. The size of the discrepancy can be estimated by looking at the difference

$$\frac{P}{2}\left\{\langle r^2 \rangle - \langle r \rangle^2\right\} = \frac{1}{2P}\left\{\langle C^2 \rangle - \langle C \rangle^2\right\} < C/2P. \tag{5.2.4}$$

The last step uses the property of a Poisson distribution that $\langle C'^2 \rangle - \langle C' \rangle^2 = C'$. If the count rate is not too large, the observed number of counts C will almost be a Poisson distribution. Also, overestimating the difference of the left hand side in eqn. 5.3.4 by using $C/2P$ partially cancels the effect of leaving out the higher order terms of the expansion. Thus the the fractional difference between C' and the approximate value given by eqn. 5.2.3 is less than $1/2P$. The minimum P

used in any of the experiments for a single sweep was 600 pulses. This gives a maximum possible error in the pile-up correction of 0.08%. As an example, if the counts observed in 600 laser pulses is 200 (r=0.33) then the approximation gives

$$C' = -600 \ln(1 - 1/3) = 243.34.$$

The actual value is less than 0.17 larger. However, since this fractional error ($\sim 1/2P$) is approximately constant over the whole decay curve, there will be essentially no effect on the lifetime due to this error in the pile-up correction.

A much larger effect related to the pile-up correction is the *underestimate* of the pile-up correction due to the addition of sweeps done at different count rates without doing the pile-up correction before the sum (*i.e.pile-up non-linearity*). For example, it is quite possible for a given point of the decay curve to have been done with as much as a 20% difference in the beam current between sweeps if one allows the beam current to vary by ±10%. So, if for the first sweep (with $P = 600$) $C' = 200$ and for the second $C' = 160$, the observed counts would have been 170.1 and 140.4 respectively. Applying the pile-up correction to a total of 310.5 counts observed only gives $C' = 359.2$, which is 0.3% too low. Of course, the average over a large number of sweeps will result in a smaller discrepancy since the beam current will usually be closer to the mean value. This effect will produce about a 0.05% *increase* in the measured lifetime at this peak count rate and can be included as a source of error. It can be eliminated entirely by taking the data so that the information about the pile-up correction for each sweep is also stored.

Up to this point the effect on the pile-up correction of using a lower level discriminator to eliminate weak noise pulses (and, as a consequence, some signal pulses as well) has not been taken into account. The percentage of pulses rejected *decreases* with increasing count rate (r) due to the increased probability of two weak pulses summing to surmount the discriminator level.

One can set an upper limit on the magnitude of this effect. Less than 10% of the signal pulses were rejected by the discriminator. The probability of two (or more) of these pulses arriving during one "laser pulse" at $r = 10\%$ *of* 0.33 is about 1.7%. Therefore the number of pulses surmounting the discriminator level was no more than 0.2% of the total observed counts at $r = 0.33$. This *decreased* the apparent lifetime by less than 0.1% and was included as a source of error for the lifetime.

Another factor which affects the accuracy of the pile-up correction is the accuracy to which the number of laser pulses, P, is known. Although the laser rate can be nominally set to $\pm 0.1\%$, one cannot utilize fractions of a laser pulse so that the maximum uncertainty was $\pm 1 pulse$ out of $600 pulses$, or about $\pm 0.2\%$ overall. For $r = 0.33$ this corresponds to a $\pm 0.04\%$ uncertainty in the corrected number of counts. However, when averaged over a large number of sweeps this effect becomes much smaller. This random uncertainty should show up in the error estimate produced by the fitting procedure used to obtain the lifetime and there is no need to account for it as a separate source of error.

A much more important effect is the *system dead-time* produced in experiments where large ion-beam backgrounds are present. This dead-time has the effect of reducing the effective number of "laser pulses". The largest ungated beam background(UBB) observed was $30,000 cps$ in the sodium experiment. This gives a dead time of $30,000 \times 600 ns = 1.8 \times 10^{-2}$, or 1.8%. Obviously this only applies to measurements taken while the ion beam is "on", *i.e.* T and B, not L or D. As an illustration of this consider $T = 200$ for $P = 600$. Applying the pile-up correction gives $T' = 243.3$, but using $P = P - (1.8\%)P = 589.2$ one obtains $T' = 244.4$, a 0.4% difference. This effect *increased* the measured lifetime by about 0.1% and was included as one of the sources of error in the lifetime.

5.2.2 The Single-Exponential Decay Signal

The single-exponential decay signal was obtained by subtracting out the background signals and then normalizing the result. Due to the non-linearity of the pile-up correction, it was made *before* subtracting the backgrounds from the total signal:

$$T_i' = -P\ln(1 - T_i/P) \quad \text{total signal}$$

$$L_i' = -P\ln(1 - L_i/P) \quad \text{laser background}$$

$$B_i' = -P\ln(1 - B_i/P) \quad \text{beam background}$$

$$S_i = (T_i' - L_i' - B_i')\overline{N}/N_i \quad \text{decay signal.}$$

N_i is the normalization for the i^{th} data point and $\overline{N}$ is the mean value of the normalization signal.

The variance of S was estimated assuming that

1) there was no error in the normalization;
2) T', L' and B'' follow Poisson statistics and their random variations are not correlated; and,
3) the pile-up correction has negligible uncertainty.

$$var(S_i) = (T_i' + L_i' + B_i')(\overline{N}/N_i)^2.$$

5.2.3 Fitting the Decay Curve

The pure decay signal decays exponentially with increasing distance from the excitation region so that

$$S_i = Ae^{-\alpha(x_i - x_1)}, \quad \alpha = v\tau = \textit{decay length},$$

$$A = \textit{amplitude at } x_1.$$

The coefficients A and α and associated uncertainties δA and $\delta\alpha$ were determined using a standard least-squares fit [Be69] to the linear equation

$$Y_i = \ln S_i = (\ln A) - \alpha(x_i - x_1).$$

The fit was weighted according to the inverse of the variance of the Y_i:

$$var(Y_i) = var(\ln S_i) = \frac{var(S_i)}{S_i^2}.$$

In order to ensure that none of the points used in the fit was taken in the interaction region, points are truncated from the beginning of the decay curve to test for systematic variation of the lifetimes so obtained. Scatter-plots of the fits were also used to test for any systematic deviation of the actual data from the fitting function.

If the reduced chi-squared (χ^2_ν) of a fit was greater than about 1.5 or the scatter-plot showed systematic variations, the fit was considered unacceptable and rejected. The fit provides the purely statistical error in the lifetime,

$$\delta\tau_i = \tau_i(\delta\alpha_i/\alpha_i),$$

which reflects the random sources of error such as the Poisson distribution of the counts and random fluctuations in beam current.

The lifetime and error estimate from each individual run was used in a weighted average to obtain the mean lifetime ($\overline{\tau}$), the standard error of the mean ($\delta\overline{\tau}_{se}$) and the single-standard deviation width ($\delta\tau_{dm}$) of the distribution of the lifetimes about the weighted mean value:

$$\overline{\tau} = \frac{\sum \tau_i w_i}{\sum w_i} \quad \text{where} \quad w_i = (1/\delta\tau_i)^2,$$

$$\delta\tau_{se} = \left(\sum 1/\delta\tau_i^2\right)^{-1/2} \qquad \text{and} \qquad \delta\tau_{dm} = \frac{\sum w_i(\overline{\tau} - \tau_i)^2}{\sum w_i}.$$

If the runs were done under the same conditions the runs were also summed and reanalyzed. Systematic errors, most of which have already been discussed, must also be included in the error estimate of the lifetime. This is discussed in the next section.

5.3 Estimation of the Uncertainty in the Lifetime

There is often a great deal of confusion as to the exact meaning of quoted error estimates, especially when averaging the results of several runs. This occurs principally as a result of the abbreviation of both "standard deviation of the distribution" and "standard error of the mean" to "single standard deviation error". The first part of this section discusses the difference between the two "errors" and which of them is more appropriate as an error estimate. The second part deals with the contribution made by systematic sources of error to the final error estimate.

5.3.1 Random Sources of Error and the Estimated Error

The random fluctuations (during and between runs) due to the beam current, beam energy, Poisson distribution of counts, normalization signal *etc.* are reflected in the (weighted) width, $\delta\tau_{dm}$, of the distribution of lifetimes (τ distribution) obtained from the fits. This width should be independent of the number of runs, assuming each run is done under about the same conditions, *e.g.* beam current and accumulation time. Therefore, it is not an ideal measure of the estimated error of the mean, $\overline{\tau}$. As an extreme example of this, consider the twenty τ_i obtained from twenty runs done under the same conditions. Then, one expects $\delta\tau_{dm}$ to be about $\sqrt{20-1}$ times the $\delta\tau$ obtained by fitting the sum of the twenty runs to form one data set.

The usefulness of $\delta\tau_{dm}$ is that it is an indication of how well the errors and lifetimes of the individual fits match the the observed distribution of lifetimes. In fact, $\delta\tau_{dm}^2$ is proportional to the reduced chi-squared, χ_ν^2 of the distribution:

$$\delta\tau_{dm}^2 = \frac{\sum w_i(\overline{\tau}-\tau_i)^2}{\sum w_i} = \frac{\nu\chi_\nu^2}{\sum w_i} \qquad (\nu = no.\ of\ runs - 1)$$

$$\text{therefore,} \quad \delta\tau_{dm} \approx \sqrt{\nu}\delta\tau_{se} \qquad (if\ \chi_\nu^2 \approx 1)$$

The last step indicates that the quantity that gives the estimated error in the mean decreases as the square root of the number of runs as one might expect. This provides a useful test for the presence of *changes* in systematic error effects between runs and also for the validity of the fitting procedure as a whole. If $\delta\tau_{dm} \gg \sqrt{\nu}\,\delta\tau_{se}$, then using $\delta\tau_{se}$ as the error estimate is not justified and $\delta\tau_{dm}$ provides a better error estimate.

5.3.2 Systematic Sources of Error

Most of the systematic sources of error have already been discussed in this and the previous chapters. These sources are summarized in Table 5.1 along with two other sources of error: de-excitation by residual gas and the effect of systematic pressure variations when UBB normalization was used. Table 5.1 provides a summary of the maximum effect on the lifetime due to each source in any of these experiments. More detailed tables, particular to each experiment, are given in the next chapter.

Collisions between the residual gas in the target chamber and the ion beam result in an apparent reduction in the lifetime:

$$\tau_{eff} = \left(\frac{1}{\tau} + \frac{2}{T_c}\right)^{-1} \qquad T_c = (N\sigma\bar{v})^{-1}.$$

Taking $\sigma \simeq 10^{-15}cm^2$, $\bar{v} \simeq 1mm/ns$ and $N \leq 4 \times 10^{-11}cm^{-3}$, $(P \leq 10^{-5}torr)$, one obtains a 0.03% reduction for a lifetime of $4ns$.

The possibility of a systematic variation (*i.e.*decline) in the target chamber pressure was a potential source of systematic error when UBB was used for normalization of the decay curve. This was first observed during some of the IR-calcium experiments, which were done after all the other experiments. The UBB, as monitored on a separate counter/timer and not stored in the computer, was

Table 5.1 Maximum effects of systematic errors on the lifetime. Not all effects listed apply to each experiment and the "maximum" doesn't apply to each experiment.

SOURCE \ DIRECTION	DECREASE	INCREASE
Pile-up non-linearity		+0.1%
Discriminator	−0.1%	
Dead-time		+0.1%
Velocity	−0.5%	+0.5%
Quantum beats	−0.004%	
Residual gas de-excitation	−0.03%	
Pressure effects on UBB		+0.8%
Decline in laser power	−0.2%	

observed to increase by between 50 and 100% while the detection system returned from the downstream position at the end of each sweep. As the the beam current was fluctuating by no more than a few percent, the only reason for such a large increase was a corresponding increase in the target chamber pressure. This was presumably caused by a temporary leak through the drive-shaft "O"-ring over the about 8 seconds of continuous travel back to the start position of the decay curve. Although the UBB dropped to within 5% its "normal" value as soon as the motion stopped and was "normal" after the first data point, it was possible that the pressure continued to decline slowly during the subsequent decay curve aquisition. Thus the usual slow decrease in UBB due to declining beam current during a sweep may have also had a small component due to declining pressure. This would cause the measured lifetime to be *too long*. The effect can be reduced by taking decay curves in both directions of travel. It also can be essentially eliminated by normalizing according to integrated beam current and using the UBB (where needed, as in the sodium experiment) only as a monitor of alignment and/or gas cell stability.

Tests showed that there was no systematic pressure effect due to the "temporary leak" before the beginning of each sweep (*i.e.* when taking data in one direction of detector travel only). However, these tests did reveal a systematic drop in pressure of about $1.8 \pm 0.5\%$ over $14mm$ of travel. This was caused by the motion of the large, flat backdrop used to provide a constant viewing background for the detection system. The plate was only about $3cm$ above the aperture of the 4-inch diffusion pump and moving the detection system downstream caused an effective increase in the pumping speed. This required a correction of -0.6% for the sodium lifetime. Due to the size of this correction compared to the other sources of error, the uncertainty in making this correction was taken to be $\pm 0.6\%$.

The total error in the mean lifetime was estimated by taking all the applicable systematic errors in quadrature with the standard error of the mean (or the standard deviation if more appropriate):

$$\delta\tau_s^2 = \sum \delta\tau_{s_i}^2 \quad \text{and} \quad \delta\tau_{=} \begin{cases} \left(\delta\tau_{se}^2 + \delta\tau_s^2\right)^{1/2}, & \text{if } \delta\tau_{dm} <\sim \sqrt{\nu}\delta\tau_{se}; \\ \left(\delta\tau_{dm}^2 + \delta\tau_s^2\right)^{1/2}, & \text{otherwise.} \end{cases}$$

CHAPTER SIX
DISCUSSION OF RESULTS

6.1 The Titanium Experiment

In this experiment the individual runs made using a variety of beam currents and two different stepping patterns as indicated in Table 6.1. The difficulty in obtaining a stable ion-beam current in the 1–4μA range is reflected in the range of the peak counts for the five data sets. The runs usually had to be terminated sooner than desired due to a drop in the beam current below the tolerance ($\pm$10%) set for the normalization. If the current could not be increased to within the preset tolerance by simply increasing the temperature of the ion-source oven, the run was ended and a new one begun after making major readjustments of the ion source. This procedure ensured that all the sweeps of a given run were done under approximately the same conditions, although it resulted in two data sets having less than about 300 counts in the peak. Although the observed count rate was quite low, with about 3% of the laser pulses producing one observed count at the peak of the decay curve, the relatively low background levels provided a signal-to-noise ratio of about 10:1 at the peak. The typical intensity decay curve displayed in Fig. 1.5 shows the relative intensities of the various components of the total signal.

The five decay curves were started at positions that were sufficiently far (about 1 to 2mm) downstream from the interaction region that truncation of points from the beginning of the curve produced no significant effect on the lifetime obtained other than to increase the uncertainty. The lifetimes obtained from the five individual data sets are shown in Table 6.1. They fall well within the statistically expected range of values , as is indicated by the value of 0.86 obtained for the reduced chi-squared of the weighted mean.

Table 6.1 The lifetime of the $z\ ^4D^o_{5/2}$ level of Ti^+ as determined from individual runs.

RUN#	τ(ns)	χ^2_ν	~PEAK COUNTS$(n/r)^a$	I(μA)	STEPPING PATTERN
1	3.951± 0.087	1.00	1350(0.023)	2.9	$12 \times 0.5mm$
2	4.150± 0.136	1.14	650(0.031)	3.7	$+6 \times 1.0mm$
3	3.959± 0.092	0.97	750(0.053)	4.1	$+3 \times 2.0mm$
4	4.296± 0.230	1.09	200(0.028)	2.3	$15 \times 0.5mm$
5	3.941± 0.259	0.97	300(0.044)	2.4	$+6 \times 1.0mm$
	4.004 ± 0.054	0.86	-weighted mean		

$\overline{\tau} = 4.012 \pm 0.054$ -correction of *+0.19%* including all sources of error (see Table 6.2 below)

$\overline{\tau} = 4.01 \pm 0.06$ -round off

[a] n/r =(peak counts)/(number of laser pulses)

The systematic corrections for the titanium experiment are given in Table 6.2. The small pile-up correction leads to small errors due to the system dead-time and discriminator correction as well as the pile-up non-linearity itself. The uncertainty in the systematic correction was calculated by taking all the individual entries in Table 6.2 in quadrature. The resulting value is only a slight overestimate of the uncertainty since the uncertainty in the velocity overshadows all the other sources of error.

Combining all the above errors in quadrature and using the weighted mean (corrected for systematic errors) of all the runs, one obtains a lifetime of 4.01 ± 0.06ns(1.5%) for the $z\ ^4D^o_{5/2}$ level of Ti^+. The value of $5.2ns \pm 15\%$ quoted by Roberts *et. al.* in their 1973 paper [RAS73] is not in agreement with this result. However, it is interesting to note that the revised f-values obtained in their subsequent work [RVC75] (obtained without re-measuring any lifetimes) imply a lifetime of $4.5ns \pm < 15\%$, which is in accord with our value.

Table 6.2 Systematic effects on the observed titanium lifetime.

CAUSE\EFFECT	INCREASE	UNKNOWN	DECREASE
Quantum Beats		±0.004%	
Collisional De-excitation			-0.1%
Dead-time	+0.01%		
Pile-up Non-linearity	+0.01%		
Discriminator			-0.01%
Laser Power Fluctuations			-0.1%
Velocity Uncertainty		±0.5%	
Misalignment		±0.03%	
Totals	+0.02%		-0.21%

Net effect is a 0.19% *decrease* in the observed lifetime.
The uncertainty due to systematic effects is taken to be all the effects added in quadrature: ±0.56%.

Other estimates for this lifetime may be obtained from the works of Warner [Wa67], who combined Coulomb approximation calculations with emission measurements to obtain f-values leading to a lifetime of 3.6ns, and of Mendlowitz [Me68], whose semi-empirical, intermediate-coupling calculations may be similarly used to obtain a lifetime of 2.8ns. Finally, the ab initio calculations of Kaijser and Linderberg [KL75] suggest a value of 2.2ns or 3.1ns, depending on whether the dipole length or dipole velocity form is used.

6.2 The Calcium Experiments

The results of the [IR-Ca] experiments have uncertainties which are about a factor of three better than those obtained in the [Ca] experiments. This was caused by several factors. First, both the laser and ion-beam background signals are almost negligible in the IR-experiment (*cf.* Figs. 1.6 and 1.7). Second, the normalization (*i.e.* ion-beam current) in the IR-experiment was constant to within less than ±0.5%, whereas the normalization in the [Ca] experiment varied

systematically, usually declining by about 6–10% over three lifetimes. Third, the analyses of the [Ca] decay curves indicated that the curves departed somewhat from a strict single-exponential decay curve. This forced a large increase in the error estimates obtained in order to account for discrepancies between either the individual data sets or between the results using different analysis techniques (*e.g.* summing data subsets, weighted means, truncation of points).

The next section describes how these data sets were analyzed, more to illustrate how it was possible to extract an accurate, if not very precise lifetime from non-ideal data, and to point out the probable cause of the difficulties.

6.2.1 The [Ca] Experiment—$^2P_{1/2}$

As indicated in previous chapters, this experiment was done by observing the "direct" transition, *i.e.* the same transition as was excited by the laser beam. This combined with an ion-beam current of about $10\mu A$, enabled one to start the decay curve about $30mm$ downstream from the interaction region and allowed for the possibility of using the "delayed-gating" technique (see §5.1.1). This was done for the series of measurements of the $^2P_{1/2}$ level.

The analysis of the nine decay curves measured in this way resulted in a weighted mean lifetime of $6.940 \pm 0.036ns$ with a reduced chi-squared of 1.27, which is not unreasonable. However, this result could only be obtained by truncating anywhere from 0–7 data points from the from the beginning of the decay curves. The number of truncation points required was different for most of the data sets. With no truncation at all, most of the runs had unacceptably large values for their reduced chi-squared.

This raised some suspicion about the validity of the error estimate since no truncation at all should be necessary at such a large distance from the interaction region and if it is used, the same truncation of points from each run should

give the same lifetime (within the estimated error). To acccount for this, the error estimates from the fitting procedure were increased so as to produce $\chi^2_\nu = 1$ for the weighted mean. The resulting uncertainty in the mean was then combined in quadrature with the other sources of error. The result was then doubled to obtain a conservative error estimate given the anomalous truncation behaviour of the analysis. The lifetime of 6.95 ± 0.18 obtained from this series of measurements turned out to be substantially lower than the result obtained in the [IR-Ca] experiment (7.07 ± 0.07) done six months later. However the two results do agree to within their estimated errors.

The difficulties described above can be attributed to the delayed-gating technique used to make the measurements. As pointed out in §5.1.1 the laser background "removed" by delayed gating produces significant system dead-time which varies greatly because of the jitter and drift in the laser pulse arrival time with respect to the gating. The effect of this would be to produce erratic variations in the number of effective laser pulses that the detection system "sees", the effect being most pronounced at the beginning of the decay curve.

6.2.2 The [Ca] Experiment—$^2P_{3/2}$

This series of experiments was done using "normal" gating but did use the UBB-normalization technique in preparation for the [Na] experiment. Analysis of the nine runs using a simple single-exponential fit (2-fit) resulted in a weighted mean lifetime of 7.08 ± 0.035 with an unacceptably large reduced chi-squared of 2.3. Only two of the individual fits had unacceptable chi-squareds (~ 1.7), with the remainder ranging from 0.92–1.4. Further analysis was done by summing compatible data sets to produce two composite decay curves and also by doing a three-parameter fit (single-exponential plus a constant) on the individual and summed decay curves. The results are shown in Table 6.3.

Table 6.3 Comparison of the results of different fitting procedures for the [Ca] $^2P_{3/2}$ series of experiments.

DATA\METHOD	2-fits (χ^2_ν)	3-fits (χ^2_ν)
Weighted mean	7.08 ± 0.04 (2.3)	6.85 ± 0.09 (0.66)
Sum of 1–3	7.23 ± 0.06 (1.4)	6.85 ± 0.12 (0.98)
Sum of 4–9	7.02 ± 0.04 (0.82)	6.89 ± 0.14 (0.82)

The 3-fit renders all the data sets consistent with each other and gives acceptable values for the chi-squared. Using the weighted mean of the two summed data sets one obtains a value of 6.87 ± 0.09 for the lifetime. However the uncertainty was then doubled so as to account for the discrepancy between this result and the value obtained from the weighted mean of the individual 2-fits. Thus the published lifetime for this series of experiments was $6.87 \pm 0.18ns$ [GPA88]. By chance the lifetime obtained in the later [IR-Ca] experiment had the same value but a much smaller uncertainty: $6.87 \pm 0.06ns$.

The discrepancy between the results of the 2 and 3-fits can be attributed to an increase in the observed lifetime caused by the dead-time effect ($\sim 0.2\%$) and the UBB pressure effect (about 0.9%, *cf.* §5.3.2). This experience suggests that it would be wise to analyze all data with a 3-fit as a further check on the single-exponential character of the decay curves. This was done with the data from the other experiments presented in this thesis and in all cases the 3-fit obtained indicated that the data was best analyzed with a 2-fit.

6.2.3 The [IR-Ca] Experiments—$^2P_{1/2,3/2}$

As indicated above, this series of experiments was done with ideal conditions: very constant ion-beam current ($10\mu A$ for J=1/2 and $5\mu A$ for J=3/2) and low background signals (*cf.* Fig 1.7). The laser background was so low (less than

5 out of 15,000 laser pulses, or, about 0.1% of the peak signal) that the data collection technique was modified so as not to waste beam time accumulating almost no counts with the ion beam turned "off" and the laser beam "on". The laser background was measured for one sweep before and after each complete data set.

Table 6.4 Systematic effects on the observed calcium lifetime ([IR-Ca] series of experiments).

CAUSE\EFFECT	INCREASE	UNKNOWN	DECREASE
Quantum Beats		±0.004%	
Collisional De-excitation			-0.012%
Dead-time	+0.02%		
Pile-up Non-linearity	+0.005%		
Discriminator			-0.1%
Velocity Uncertainty		±0.5%	
Misalignment		±0.06%	
Totals	+0.025%		-0.112%

Net effect is a 0.087% *decrease* in the observed lifetime.
The uncertainty due to systematic effects is taken to be all the effects added in quadrature: ±0.52%.

Each data set consisted of from 16 to 20 sweeps giving a total of between 3000 and 5000 counts at the peak of the decay curve. Each sweep consisted of 25 data points spaced $1mm$ apart. In order to reduce *real*-time dependent effects (*cf.* §5.1.1), alternate sweeps were taken in opposite directions of travel. The forwards and backwards sweeps were analyzed separately and then together. No systematic differences were observed between the two. The start position for the sweeps (about $14mm$ for the $J = 1/2$ level and $5mm$ for the $J = 3/2$ level) were sufficiently far downstream from the interaction region that the laser background was constant over the whole decay curve. Helmholtz coils were used to essentially eliminate the earth's magnetic field, making the effect of quantum beats on the

Table 6.5 Lifetimes(ns) obtained from single-exponential fits for the [IR-Ca] experiments.

RUN/LEVEL	$^2P_{1/2}$ (χ^2_ν)	$^2P_{3/2}$ (χ^2_ν)
1	7.099 ± 0.056 (1.08)	6.784 ± 0.050 (0.38)
2	7.035 ± 0.061 (0.51)	6.897 ± 0.047 (0.73)
3	6.979 ± 0.061 (1.11)	6.859 ± 0.044 (0.68)
4	6.979 ± 0.062 (1.15)	6.862 ± 0.049 (1.18)
5		*6.882 ± 0.041 (1.13)
weighted mean	7.070 ± 0.030 (1.74) ± 0.040 (1.00)	6.860 ± 0.020 (0.61)
summed data (all)	7.067 ± 0.030 (0.90)	6.876 ± 0.020 (0.59)
summed data (1–4)		*6.857 ± 0.024 (0.42)
weighted mean of *		6.863 ± 0.021 (0.28)
average value	7.069 ± 0.040	6.861 ± 0.021
with corrections	7.075 ± 0.06	6.867 ± 0.05
round off	7.07 ± 0.07	6.87 ± 0.06

decay curve negligible. The only significant systematic source of error was the velocity as is shown in Table 6.4.

The results of the analysis of the individual runs and summed data sets are presented in Table 6.5. Truncation of points produced no significant variation in the lifetime obtained from the fit. The weighted mean for the J=1/2 level has a $\chi^2_\nu = 1.74$. The probablility that the reduced chi-squared is less than this is 85%. Essentially the same lifetime was obtained from the summed data with a more reasonable $\chi^2_\nu = 0.9$, indicating that it was probably just chance that produced such a large χ^2_ν for the weighted mean. However, to be sure of the error estimate, the value that would produce a $\chi^2_\nu = 1.0$ was used for the estimated error of the mean. This gives a final result for the lifetime of the J=1/2 level of $7.07 \pm 0.07ns$.

The sum of all the J=3/2 data sets results in a lifetime of $6.876 \pm 0.020ns$

Fig. 6.1 Lifetimes(ns) of the $Ca^+ 4p^2 P^o_{1/2,3/2}$ levels obtained from this work as well as previous measurements and theoretical estimates.

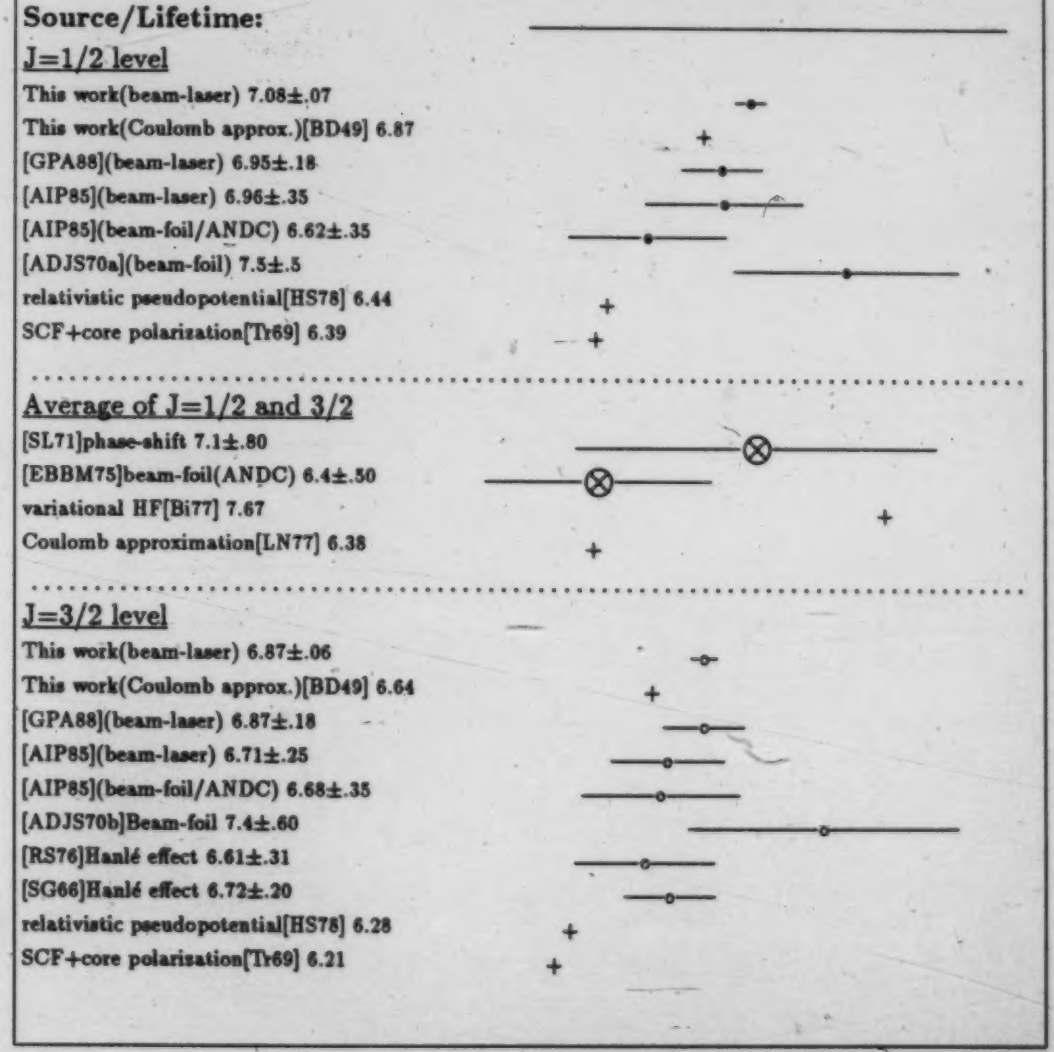

which is larger than that obtained from the weighted mean of the individual runs ($6.860 \pm 0.020 ns$). This is due to run #5 having about a 50% greater excitation

efficiency (*i.e.* peak signal/integrated beam current) than the rest of the runs. This increase in efficiency was caused by defocussing the ion beam at the defining aperture so as to decrease the Doppler width of the ion beam with respect to the laser beam. When set #5 is excluded from the sum one obtains essentially the same result as the weighted mean. This leads to a lifetime for the $^2P_{3/2}$ level of $6.87 \pm 0.06ns$.

Fig. 6.1 graphically presents the results obtained from this work as well as previous measurements and theoretical estimates. The experimental lifetimes for the calcium levels are in agreement within the estimated errors and are greater than all the theoretical results except for the variational Hartree-Fock result.

Table 6.6 Systematic effects on the observed sodium lifetime.

CAUSE\EFFECT	INCREASE	UNKNOWN	DECREASE
Quantum Beats(Hfs)		±0.02%	
Collisional De-excitation			-0.03%
Dead-time	+0.1%		
Pile-up Non-linearity	+0.1%		
Discriminator			-0.1%
Decline in laser power			-0.2%
UBB normalization	+0.6%		
Velocity Uncertainty		±0.5%	—
Misalignment		±0.03%	
Totals	+0.8%		-0.33%

Net effect is a 0.47% *increase* in the observed lifetime.
The uncertainty due to systematic effects is taken to be all the effects added in quadrature: ±0.83%.

6.3 The Sodium Experiment

Perhaps the most remarkable thing about the sodium experimental data is that there is little to remark about it, considering the potential problems with

the requirements of doing a two stage excitation as well as monitoring the "direct" transition. As mentioned in Chapter Four, the ion-beam current was very stable considering the possibility of additional fluctuations caused by pressure variations in the gas cell. Comparison of the relative efficiency of the gas cell excitation between individual runs suggest that this was constant to better than 7%. The gas cell was also more efficient (*cf.* §4.3) at populating the metastable level than had been anticipated. The only significant difference between the quality of these data and that of the [Ti] and [IR-Ca] experiments was due to the small systematic error in the UBB normalization caused by the systematic decline in pressure with distance from the interaction region. This correction of 0.6% in the measured lifetime was assumed to have an uncertainty equal to the magnitude of the correction itself. The systematic effects on the lifetime are shown in Table 6.6 and the lifetimes obtained from the analysis of individual runs and summed data sets are presented in Table 6.7.

Fig. 6.2 graphically presents the results obtained from this work as well as previous measurements and theoretical estimates. The lifetime of the sodium level obtained in this work ($4.81 \pm 0.06ns$) agrees with the previous beam-foil (ANDC) result obtained here at the University of Alberta, which was significantly smaller than earlier beam-foil results. This was not surprising, since early beam-foil lifetimes were frequently too large due to cascading from higher levels. This value is also in good agreement with the two theoretical results obtained using intermediate coupling.

6.4 CONCLUSIONS

The techniques described in this thesis have enabled measurements of lifetimes in the 4 to $10ns$ range to a precision of between 1–1.5%. This level of

Table 6.7 The lifetime of the $2p^5(^2P^o_{3/2})3p[5/2]_{J=3}$ level of Na^+ as determined from individual runs and summed data sets.

RUN#	τ(ns)	χ^2_ν	~PEAK COUNTS$(n/r)^a$	I(μA)	STEPPING PATTERN
1	4.805± 0.082	0.95	3200(0.13)	11	$25 \times 0.5mm$
2	4.796± 0.082	1.11	2550(0.15)	9	
3	4.966± 0.142	0.81	1400(0.11)	10	$20 \times 1mm$
4	4.737± 0.082	1.07	3200(0.11)	10	
5	4.990± 0.085	0.45	3100(0.10)	10	
6	4.777± 0.064	0.79	4300(0.14)	10	
7	4.966± 0.118	0.92	460(0.12)	11	
	*4.833 ± 0.033	1.15	–weighted mean		
	4.802± 0.058	0.77	–sum of 1–2		
	4.837± 0.039	0.77	–sum of 3–7		
	*4.826± 0.032	0.77	–weighted mean of sums		
	4.830± 0.0337		–average of *		

$\overline{\tau} = 4.807 \pm 0.052$ –correction of *-0.47%* including all sources of error (see Table 6.6 above)

$\overline{\tau} = 4.81 \pm 0.06$ –round off

[a] n/r =(peak counts)/(number of laser pulses)

Fig. 6.2 Lifetimes(ns) of the Na^+ $2p(^2P^o_{3/2})3p[5/2]_{J=3}$ level obtained from this work as well as previous measurements and theoretical estimates.

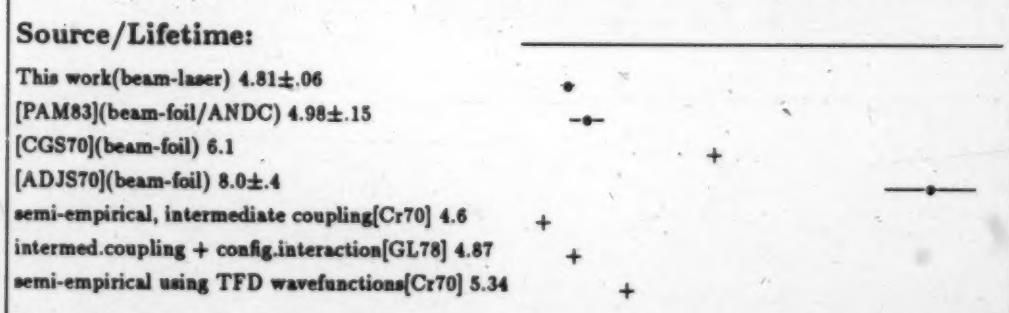

precision is adequate for placing relative f-values, most of which have an uncertainty greater than about 1%, on an absolute scale. The level of precision obtained is also far better than the corresponding spread in theoretical estimates, indicating the need for further calculations for these species.

The main problem preventing further improvements in the precision of the measurement is the uncertainty in the velocity (*i.e.* the energy calibration of the accelerator). However, in order to make the uncertainty in the velocity much smaller than at present, it would be necessary to measure the velocity of the ions during the course of the actual lifetime measurements. This is due to possible variation in the energy calibration of the accelerator with changing source conditions, including the possibility that the calibration is different for heavier ions than those (H and He) that have been used for the present calibration. This velocity measurement could be done using an electrostatic analyzer after the target chamber.

Systematic effects on the decay curve would become more important if higher levels of precision are desired. Slow, systematic variations with time could be significantly reduced by alternating forwards and backwards sweeps along the decay curve as was done in the [IR-Ca] series of experiments. It would also be useful to record both the integrated ion-beam current and the ungated beam-background(UBB) at each point of the decay curve. The former could be used for normalization of the decay signal and the latter as a monitor for possible systematic variations (*e.g.* pressure and/or misalignment effects).

The dye-laser used in these experiments is limited to wavelengths greater than about 350nm (in order to achieve the saturation of the transition required to ensure a negligible variation of the excited-state population with fluctuations in laser power). This severely limits the number of atomic levels that are accessable

using a single-stage excitation process. The success of the sodium experiment (*i.e.* two-step excitation using a gas cell) opens up the possibility of the measurement of levels other than the ones presented in this thesis.

A wider variety of levels can be attempted using frequency-doubling of the dye laser. Frequency-doubling would allow measurement of at least one multiplet for most of the singly-ionized members of the iron group, which is of particular interest to astrophysicists. However, it remains to be seen whether sufficient laser intensity to saturate the transitions can be achieved with the frequency-doubled beam.

REFERENCES

[ADJS70a] T. Andersen, J. Desesquelles, K.A. Jessen and G. Sørensen, *J. Quant. Spectrosc. Radiat. Transfer* **10** (1970) 1143.

[ADJS70b] T. Andersen, J. Desesquelles, K.A. Jessen and G. Sørensen, *Phys. Rev.* **A1** (1970) 1294.

[An76] H.J. Andrä in: *Beam Foil Spectroscopy, vol. II, eds. I.A. Sellin and D.J. Pegg (Plenum Press, 1976)* p. 835.

[AIP85] W. Ansbacher, A.S. Inamdar and E.H. Pinnington, *Phys. Lett.* **110A** (1985) 383.

[AP842] W. Ansbacher and E.H. Pinnington, *Nucl. Instr. and Meth.* **B4** (1984) 207.

[Be69] P.R. Bevington, "Data Reduction and Error Analysis for the Physical Sciences", McGraw-Hill, New York (1969).

[Bi77] E. Biémont, *Physica* **85C** (1977) 393.

[BD49] D.R. Bates and A. Damgaard, *Phil. Trans. Roy. Soc.* **A242** (1949) 101.

[BMP82] D.E. Blackwell, S.L.R. Menon and A.D. Petford, *Mon. Not. R. Astr. Soc.* **201** (1982) 603.

[BMPS82] D.E. Blackwell, S.L.R. Menon, A.D. Petford and M.J. Shallis, *Mon. Not. R. Astr. Soc.* **201** (1982) 611.

[CGS70] M. Carré, M.L. Gaillard and J.L. Subtil, *Nucl. Instr. and Meth.* **90** (1970) 217.

[Co77] A. Corney, "Atomic and Laser Spectroscopy", Clarendon Press, Oxford (1977).

[Cr70] M. Crance, *Compt. Rend. Acad. Sci. Paris* **271** (1970) 1089.

[DK80] K. Danzmann and M. Kock, *J. Phys. B: Atom. Molec. Phys.* **13** (1980) 2051.

[DS78] J.N. Dodd and G.W. Series in: "Progress in Atomic Spectroscopy–Part A", eds. W. Hanle and H. Kleinpoppen, Plenum Press, New York (1978) Chapter 14.

[EBBM75] B. Emmoth, M. Braun, J.Bromander and I.Martinson, *Phys. Scr.* **12** (1975) 75.

[Gi75] E. Giacobino, *J. Physique–Lett.* **36** (1975) L65.

[Gr84] N. Grevesse, *Phys. Scr.* **T8** (1984) 49.

[GKA82] A. Gaupp, P. Kuske and H.J. Andrä, *Phys. Rev. A* **26** (1982) 3351.

[GPA87] R.N. Gosselin, E.H. Pinnington and W. Ansbacher, *Phys. Lett.* **123A** (1987) 175.

[GPA88] R.N. Gosselin, E.H. Pinnington and W. Ansbacher, *Nucl.Instr.Meth. (in press)* (1988) .

[GL78] R.F. Gruzdev and A.V. Loginov, *Opt. Spectrosc.* **45** (1978) 846.

[HS78] P. Hafner and W.H.E. Schwarz, *J. Phys.* **B11** (1978) 2975.

[KKW78] P. Kuske, N Kirchner, W. Wittmann, H.J. Andrä and D. Kaiser, *Phys. Lett.* **64A** (1978) 377.

[KL75] P. Kaijser and J. Linderberg, *J. Phys. B* **6** (1973) 1975.

[KP75] R.L. Kurucz and E. Peytremann, *Smithsonian Astrophysical Observatory Special Report* **362** (1975).

[Lo83] R. Loudon, "The quantum theory of light"(2nd edition), Oxford University Press, New York (1983).

[LN77] A. Lindgard and S.E. Nielsen, *At. Data Nucl. Data Tables* **19** (1977) 533.

[Ma66] J.B. Marion, *Rev. Mod. Phys.* **38** (1966) 660.

[Me68] H. Mendlowitz, *Astrophys. J.* **154** (1968) 1099.

[PAM83] E.H. Pinnington, W. Ansbacher and P. Meenakshi Raja Rao, *Phys. Lett.* **97A** (1983) 337.

[PG79] E.H. Pinnington, R.N. Gosselin, J.A. O'Neill, J.A. Kernahan, K.E. Donnelly and R.L. Brooks, *Phys. Scr.* **20** (1979) 151.

[RS76] F.H.K. Rambow and L.D. Shearer, *Phys. Rev.* **A14** (1976) 1735.

[RAS73] J.R. Roberts, T. Andersen and G. Sørensen, *Astrophys. J.* **181** (1973) 567.

[RMBW59] M. Rotenberg, R. Bivins, N. Metropolis and J.K. Wooten, JR., "The 3-j and 6-j Symbols", The Technology Press(MIT), Cambridge(1959).

[RVC75] J.R. Roberts, P.A. Voigt and A Czernichowski, *Astrophys. J.* **197** (1975) 791.

[SG66] W.W. Smith and A. Gallagher, *Phys. Rev.* **145** (1966) 26.

[SL71] W.H. Smith and H.S. Liszt, *J. Opt. Soc. Am.* **61** (1971) 938.

[Tr69] E. Trefftz, quoted in: W.L. Wiese, M.W. Smith and R.M. Miles,*Atomic Transition Probabilities Vol. 2 NSRDS-NBS* **22** (Washington, 1969).

[Wa67] B. Warner, *Mem. R. Astr. Soc.* **70** (1967) 165.

[We78] M. Weissbluth, "Atoms and Molecules—Student Edition", Academic Press, New York (1978).

[Wo83] G.K. Woodgate, "Elementary Atomic Structure"(2nd edition), Oxford University Press, New York (1983).

APPENDIX I

QUANTUM BEAT CALCULATION

The purpose of this appendix is to provide a detailed calculation of the effect of Zeeman quantum beats on the lifetimes measured in the [Ca] series of experiments (*cf.* §2.5). It is also hoped that it will be useful in that it provides a sample *practical* calculation of the effect. The observation is done over a finite solid angle and the excitation and observation geometries are non-trivial, requiring the application of rotation transformations in completing the calculation. A useful introduction to the subject of quantum beats and coherent excitation can be found in Corney[Co77, Chapter 15].

As outlined in §2.5, "coherent" excitation of the upper levels can cause beat components at ω_L and $2\omega_L$ to be present in the decay curve (*cf.* eqn.2.5.1). One can estimate the effect on the lifetime obtained from a single-exponential fit by computing the relative intensities of the three components. This can be done without a detailed knowledge of the atomic wavefunctions by using the Wigner-Eckhart theorem (see below). Coherent excitation does not refer to the coherence of the laser, but to the *polarization* coherence of the incident radiation. A necessary condition for coherent excitation is that the dipole operator $\hat{\mathbf{e}} \cdot \mathbf{D}$ be able to cause a transition to the two (or more) upper levels from a single lower level. This is equivalent to saying that the off-diagonal elements of the excitation matrix ($\mathcal{F}$, see below) must be non-zero. In order to then observe quantum beats from the decay of these two states, they must decay to the same lower level via the observation operator $\hat{\mathbf{e}}' \cdot \mathbf{D}$; or, the off-diagonal elements of the observation matrix $\mathcal{G}$ must be non-zero. This latter condition and the dipole transition selection rules allow beats to occur only between states separated by $\Delta m = \pm 1$ or ± 2 (*i.e.* ω_L and $2\omega_L$).

A1.1 Quantum Beats — General

In what follows the m's denote the states excited by the incident light and the μ's denote the other (lower) levels. The excitation and observation matrices are given by

$$\mathcal{F}_{mm'} = \sum_{\mu} \langle m \mid \hat{\mathbf{e}} \cdot \mathbf{D} \mid \mu \rangle \langle \mu \mid \hat{\mathbf{e}}^* \cdot \mathbf{D} \mid m' \rangle.$$

$$\mathcal{G}_{m'm} = \sum_{\mu'} \langle m' \mid \hat{\mathbf{e}}' \cdot \mathbf{D} \mid \mu' \rangle \langle \mu' \mid \hat{\mathbf{e}}'^* \cdot \mathbf{D} \mid m \rangle.$$

From Corney [Co77, Chapter 15] the intensity of the emitted radiation is given by

$$\frac{dI}{d\Omega} = C' \sum_{m,m',\mu,\mu'} \mathcal{F}_{m,m'} \mathcal{G}_{m',m} \rho_{\mu\mu} \left[\exp\{(\Gamma + ix)(t_0 + \Delta t_0)\} - \exp\{(\Gamma + ix)t_0\}\right] \times$$
$$\times \frac{\exp\{-(\Gamma + ix)t\}}{(\Gamma + ix)};$$

$$C' = \frac{U(\omega)}{8\pi\epsilon_o^2} \left(\frac{\omega}{\hbar c}\right)^3 \quad x = (m - m')\omega_L \quad \text{and} \quad \Gamma = 1/\tau.$$

$U(\omega)$ is the energy density of the incident beam and ρ is the density matrix. For the case under consideration (*cf.* §2.5) this can be simplified by using:

$$t_o = \text{start time of excitation pulse} = 0,$$

$$\Delta t_o = \delta = \text{ duration of excitation pulse } \approx \tau = \Gamma^{-1},$$

and since $\Gamma \approx 1000\omega_L$ one obtains,

$$\frac{dI}{d\Omega} = Ce^{-t/\tau} \sum_{m,m',\mu,\mu'} \mathcal{F}_{m,m'} \mathcal{G}_{m',m} \rho_{\mu\mu} e^{-ixt}, \quad \text{with} \quad C = C'[e^{\delta/\tau} - 1]\tau. \quad A1.1.1$$

The (complex) polarization vector, $\hat{\mathbf{e}}$ can be expanded in terms of the spherical unit vectors

$$\hat{\mathbf{e}}_{\pm 1} = \mp \frac{1}{\sqrt{2}}(\hat{\mathbf{i}} + i\hat{\mathbf{j}}) \quad \text{and} \quad \hat{\mathbf{e}}_o = \hat{\mathbf{k}}: \quad \hat{\mathbf{e}} = \sum_{q=-1}^{1} (-1)^q \hat{\mathbf{e}}_q \mathcal{E}_{-q}.$$

All the elements of $\mathcal{F}$ and $\mathcal{G}$ are calculated from products of terms of the form

$$\langle jm \mid \hat{\mathbf{e}} \cdot \mathbf{D} \mid j'm' \rangle = \langle jm \mid \mathcal{E}_0 D_o - \mathcal{E}_{-1} D_{+1} - \mathcal{E}_{+1} D_{-1} \mid j'm' \rangle =$$

$$= \mathcal{E}_0 \langle jm \mid D_o \mid j'm' \rangle - \mathcal{E}_{-1} \langle jm \mid D_{+1} \mid j'm' \rangle - \mathcal{E}_{+1} \langle jm \mid D_{-1} \mid j'm' \rangle.$$

Using the Wigner-Eckhart theorem (for example see §6.3 of Weissbluth [We78]) one can factor out the reduced matrix element from each term:

$$\langle jm \mid D_q \mid j'm' \rangle = (-1)^{j-m} \begin{pmatrix} j & 1 & j' \\ -m & q & m' \end{pmatrix} \langle j \parallel \mathbf{D} \parallel j' \rangle. \qquad A1.1.2$$

For linearly polarized light the components can be expressed as

$$\mathcal{E}_{\pm 1} = \mp \frac{1}{\sqrt{2}} (\cos\theta \cos\alpha \pm i \sin\alpha) e^{\pm i\phi} \quad \text{and} \quad \mathcal{E}_0 = -\sin\theta \cos\alpha. \qquad A1.1.3$$

The angles θ and ϕ specify the incoming position of the incident beam in the coordinate system with the quantization axis ($\hat{\mathbf{z}}$) parallel to the magnetic field. The angle α is the angle between $\hat{\theta}$ and $\hat{\mathbf{e}}$ measured in the counter-clocwise sense when looking along the direction of travel of the incident beam. The expressions for the emitted radiation are identical and will be denoted by primes on all the quantities.

At this point it is worthwhile noting that one always obtains zero off-diagonal matrix elements for the observation matrix if observing along the direction of the magnetic field (*i.e.* quantization axis). This occurs because the dipole transition selection rules only allow off-diagonal terms of the form $\mathcal{E}_0 \mathcal{E}^*_{\pm 1}$, $\mathcal{E}^*_0 \mathcal{E}_{\mp 1}$ or $\mathcal{E}_{\pm 1} \mathcal{E}^*_{\mp 1}$. Integrating these symmetrically about the quantization axis ($\int_0^{2\pi} [\,] d\phi$) gives zero.

A1.2 Quantum Beats — J=1/2 Level

It is more convenient when calculating $\mathcal{F}$ and $\mathcal{G}$ to write them in the form

$$\mathcal{F}_{mm'} = \sum_{\mu} \langle m \mid \hat{\mathbf{e}} \cdot \mathbf{D} \mid \mu \rangle \langle m' \mid \hat{\mathbf{e}} \cdot \mathbf{D} \mid \mu \rangle^*.$$

$$\mathcal{G}_{m'm} = \sum_{\mu'} \langle m' \mid \hat{\mathbf{e}} \cdot \mathbf{D} \mid \mu' \rangle \langle m \mid \hat{\mathbf{e}} \cdot \mathbf{D} \mid \mu' \rangle^*.$$

Evaluating these expressions using equations A1.1 and omitting the common factor of the reduced matrix element, one obtains:

$$\langle \tfrac{1}{2}, \tfrac{1}{2} \mid \mathcal{E}_0 D_0 \mid \tfrac{1}{2}, \tfrac{1}{2} \rangle \Rightarrow (-1)^{\frac{1}{2}-\frac{1}{2}} \begin{pmatrix} \frac{1}{2} & 1 & \frac{1}{2} \\ -\frac{1}{2} & 0 & \frac{1}{2} \end{pmatrix} \mathcal{E}_0 = +\mathcal{E}_0/\sqrt{6}.$$

$$\langle \tfrac{1}{2}, -\tfrac{1}{2} \mid \mathcal{E}_0 D_0 \mid \tfrac{1}{2}, -\tfrac{1}{2} \rangle \Rightarrow (-1)^{\frac{1}{2}--\frac{1}{2}} \begin{pmatrix} \frac{1}{2} & 1 & \frac{1}{2} \\ --\frac{1}{2} & 0 & -\frac{1}{2} \end{pmatrix} \mathcal{E}_0 = -\mathcal{E}_0/\sqrt{6}.$$

$$\langle \tfrac{1}{2}, \tfrac{1}{2} \mid -\mathcal{E}_{-1} D_{+1} \mid \tfrac{1}{2}, -\tfrac{1}{2} \rangle \Rightarrow -(-1)^{\frac{1}{2}-\frac{1}{2}} \begin{pmatrix} \frac{1}{2} & 1 & \frac{1}{2} \\ -\frac{1}{2} & +1 & -\frac{1}{2} \end{pmatrix} \mathcal{E}_{-1} = +\mathcal{E}_{-1}/\sqrt{3}.$$

$$\langle \tfrac{1}{2}, -\tfrac{1}{2} \mid -\mathcal{E}_{+1} D_{-1} \mid \tfrac{1}{2}, \tfrac{1}{2} \rangle \Rightarrow -(-1)^{\frac{1}{2}--\frac{1}{2}} \begin{pmatrix} \frac{1}{2} & 1 & \frac{1}{2} \\ --\frac{1}{2} & -1 & \frac{1}{2} \end{pmatrix} \mathcal{E}_{+1} = -\mathcal{E}_{+1}/\sqrt{3}.$$

Using the above equations one obtains the $\mathcal{F}$ matrix

$$\mathcal{F} = \frac{1}{3} \begin{pmatrix} \frac{1}{2}\mathcal{E}_0^2 + \mathcal{E}_{-1}\mathcal{E}_{-1}^* & -\frac{1}{\sqrt{2}}\mathcal{E}_0(\mathcal{E}_{+1}^* + \mathcal{E}_{-1}) \\ -\frac{1}{\sqrt{2}}(\mathcal{E}_{+1} + \mathcal{E}_{-1}^*) & \frac{1}{2}\mathcal{E}_0^2 + \mathcal{E}_{+1}\mathcal{E}_{+1}^* \end{pmatrix}$$

$$(\text{using } \mathcal{E}_{\pm 1} = -\mathcal{E}_{\mp 1}^*) \quad = \frac{1}{3} \begin{pmatrix} \frac{1}{2}\mathcal{E}_0^2 + \mathcal{E}_{-1}\mathcal{E}_{-1}^* & 0 \\ 0 & \frac{1}{2}\mathcal{E}_0^2 + \mathcal{E}_{+1}\mathcal{E}_{+1}^* \end{pmatrix}.$$

The $\mathcal{G}$ matrix is the same with primes on all the elements. Thus there is no possibility of quantum beats for the $^2P_{1/2}$ measurement for linearly polarized light.

A1.3 Quantum Beats — J=3/2 Level

Using the equations from §A1.1 one obtains

$$\langle \tfrac{3}{2},\tfrac{1}{2} \mid \mathcal{E}_0 D_0 \mid \tfrac{1}{2},\tfrac{1}{2}\rangle \Rightarrow (-1)^{\frac{3}{2}-\frac{1}{2}} \begin{pmatrix} \frac{3}{2} & 1 & \frac{1}{2} \\ -\frac{1}{2} & 0 & \frac{1}{2} \end{pmatrix} \mathcal{E}_0 = +\mathcal{E}_0/\sqrt{6}.$$

$$\langle \tfrac{3}{2},-\tfrac{1}{2} \mid \mathcal{E}_0 D_0 \mid \tfrac{1}{2},-\tfrac{1}{2}\rangle \Rightarrow (-1)^{\frac{3}{2}--\frac{1}{2}} \begin{pmatrix} \frac{3}{2} & 1 & \frac{1}{2} \\ --\frac{1}{2} & 0 & -\frac{1}{2} \end{pmatrix} \mathcal{E}_0 = \mathcal{E}_0/\sqrt{6}.$$

$$\langle \tfrac{3}{2},\tfrac{1}{2} \mid -\mathcal{E}_{-1} D_{+1} \mid \tfrac{1}{2},-\tfrac{1}{2}\rangle \Rightarrow -(-1)^{\frac{3}{2}-\frac{1}{2}} \begin{pmatrix} \frac{3}{2} & 1 & \frac{1}{2} \\ -\frac{1}{2} & +1 & -\frac{1}{2} \end{pmatrix} \mathcal{E}_{-1} = -\mathcal{E}_{-1}/2\sqrt{3}.$$

$$\langle \tfrac{3}{2},\tfrac{3}{2} \mid -\mathcal{E}_{-1} D_{+1} \mid \tfrac{1}{2},\tfrac{1}{2}\rangle \Rightarrow -(-1)^{\frac{3}{2}-\frac{3}{2}} \begin{pmatrix} \frac{3}{2} & 1 & \frac{1}{2} \\ -\frac{3}{2} & +1 & \frac{1}{2} \end{pmatrix} \mathcal{E}_{-1} = -\mathcal{E}_{-1}/2.$$

$$\langle \tfrac{3}{2},-\tfrac{1}{2} \mid -\mathcal{E}_{+1} D_{-1} \mid \tfrac{1}{2},\tfrac{1}{2}\rangle \Rightarrow -(-1)^{\frac{3}{2}--\frac{1}{2}} \begin{pmatrix} \frac{3}{2} & 1 & \frac{1}{2} \\ --\frac{1}{2} & -1 & \frac{1}{2} \end{pmatrix} \mathcal{E}_{+1} = -\mathcal{E}_{+1}/2\sqrt{3}.$$

$$\langle \tfrac{3}{2},-\tfrac{3}{2} \mid -\mathcal{E}_{+1} D_{-1} \mid \tfrac{1}{2},-\tfrac{1}{2}\rangle \Rightarrow -(-1)^{\frac{3}{2}--\frac{3}{2}} \begin{pmatrix} \frac{3}{2} & 1 & \frac{1}{2} \\ --\frac{3}{2} & -1 & -\frac{1}{2} \end{pmatrix} \mathcal{E}_{+1} = -\mathcal{E}_{+1}/\sqrt{2}.$$

$$\mathcal{F} = \begin{pmatrix} \frac{\mathcal{E}_{-1}\mathcal{E}^*_{-1}}{4} & \frac{\mathcal{E}_{-1}\mathcal{E}^*_0}{2\sqrt{6}} & \frac{\mathcal{E}_{-1}\mathcal{E}^*_{+1}}{4\sqrt{3}} & 0 \\ * & \frac{(\mathcal{E}_0\mathcal{E}^*_0+\mathcal{E}_{-1}\mathcal{E}^*_{-1}/2)}{6} & \frac{-(\mathcal{E}_0\mathcal{E}^*_{+1}+\mathcal{E}_{-1}\mathcal{E}^*_0)}{6\sqrt{2}} & \frac{\mathcal{E}_{-1}\mathcal{E}^*_{+1}}{4\sqrt{3}} \\ * & * & \frac{(\mathcal{E}_0\mathcal{E}^*_0+\mathcal{E}_{+1}\mathcal{E}^*_{+1}/2)}{6} & \frac{-\mathcal{E}_0\mathcal{E}^*_{+1}}{2\sqrt{6}} \\ 0 & * & * & \frac{\mathcal{E}_{+1}\mathcal{E}^*_{+1}}{4} \end{pmatrix}.$$

The * represent the complex conjugate of the element in the transposed position (*i.e.* $\mathcal{F}_{mm'} = \mathcal{F}^*_{m'm}$). Again using $\mathcal{E}_{\pm 1} = -\mathcal{E}^*_{\mp 1}$ and the fact that $\mathcal{E}_0$ is real for linearly polarized light one obtains:

$$\mathcal{F} = \begin{pmatrix} \frac{\mathcal{E}_{-1}\mathcal{E}^*_{-1}}{4} & \frac{\mathcal{E}_{-1}\mathcal{E}_0}{2\sqrt{6}} & \frac{-\mathcal{E}^2_{-1}}{4\sqrt{3}} & 0 \\ * & \frac{(\mathcal{E}_0\mathcal{E}^*_0+\mathcal{E}_{-1}\mathcal{E}^*_{-1}/2)}{6} & 0 & \frac{-\mathcal{E}^2_{-1}}{4\sqrt{3}} \\ * & 0 & \frac{(\mathcal{E}_0\mathcal{E}^*_0+\mathcal{E}_{-1}\mathcal{E}^*_{-1}/2)}{6} & \frac{\mathcal{E}_0\mathcal{E}_{-1}}{2\sqrt{6}} \\ 0 & * & * & \frac{\mathcal{E}_{-1}\mathcal{E}^*_{-1}}{4} \end{pmatrix}.$$

For the [Ca] experiment the incident laser radiation made an angle of 135° with respect to the (horizontal) ion-beam direction. The direction of the residual magnetic field and the ion beam formed a vertical plane so that the rotation matrix to convert from the "lab frame of reference (X, Y, Z) or (R, Θ, Φ)" to the "quantization axis frame of reference (x, y, z) or (r, θ, ϕ)" is equivalent to a 2-D transformation in the Y–Z plane:

$$\begin{pmatrix} X \\ Y \\ Z \end{pmatrix} = \begin{pmatrix} 1 & 0 & 0 \\ 0 & \cos\beta & -\sin\beta \\ 0 & \sin\beta & \cos\beta \end{pmatrix} \begin{pmatrix} x \\ y \\ z \end{pmatrix}$$

The angle, β, between $\hat{\mathbf{Z}}$ (*i.e.* straight down) and the magnetic field direction ($\hat{\mathbf{z}}$) was about 10°.

The position on the unit sphere of the incident radiation was

$$\mathbf{L} = (-1/\sqrt{2}, 1/\sqrt{2}, 0)_{XYZ} = (-1/\sqrt{2}, 0.6964, -0.1228)_{xyz} \quad \text{or}$$

$$\phi = 135.4° \quad \text{and} \quad \theta = 97.05°.$$

The angle α can be determined from $\sin\theta = (\hat{\theta} \times \hat{\mathbf{e}}) \cdot \hat{\mathbf{r}}$, where

$$\hat{\theta} = \cos\theta\cos\phi\hat{\mathbf{x}} + \cos\theta\sin\phi\hat{\mathbf{y}} - \sin\theta\hat{\mathbf{z}}.$$

The dye laser beam has a unit polarization vector $\hat{\mathbf{e}} = (0, 0, -1)_{XYZ}$ or $\hat{\mathbf{e}} = (0, -0.1736, -0.9848)_{xyz}$ giving $\alpha = 7.107°$.

Using equations A1.1 this gives the following numbers for the expressions in $\mathcal{F}$:

$$\mathcal{E}_0 = -\sin\theta\cos\alpha = -0.9848, \qquad \mathcal{E}_{-1}\mathcal{E}_{-1}^* = \frac{1 - \mathcal{E}_0^2}{2} = 0.01506,$$

$$\mathcal{E}_{-1} = \frac{1}{\sqrt{2}}(\cos\theta\cos\alpha - i\sin\alpha)e^{-i\phi} = -6.097 \times 10^{-6} + i0.1228 \quad \text{and}$$

$$\mathcal{E}^2_{-1} = 0.01508 - i1.497 \times 10^{-6}.$$

The $\mathcal{G}$ matrix has the same form as $\mathcal{F}$ if observations are made through a linear polarizer. The matrix for observation without any polarizer can be found by adding the corresponding matrix at $\alpha' + \pi/2$:

$$\mathcal{G} \leftarrow \mathcal{G}(\alpha') + \mathcal{G}(\alpha' + \pi/2).$$

Since the $\mathcal{F}$ and $\mathcal{G}$ matrices are independent of each other, the primes for the "observation" quantities will be dropped from this point on. Whether one is dealing with the excitation or observation parameters will be understood by the context in which they are used. The terms required to evaluate $\mathcal{G}$ then become

$$\mathcal{E}_{-1}\mathcal{E}^*_{-1}(\alpha) + \mathcal{E}_{-1}\mathcal{E}^*_{-1}(\alpha + \pi/2) = \frac{1}{2}(1 + \cos^2\theta),$$

$$\mathcal{E}_0\mathcal{E}^*_{-1}(\alpha) + \mathcal{E}_0\mathcal{E}^*_{-1}(\alpha + \pi/2) = -\frac{\sin 2\theta}{2\sqrt{2}}e^{-i\phi},$$

$$\mathcal{E}^2_{-1}(\alpha) + \mathcal{E}^2_{-1}(\alpha + \pi/2) = \frac{1}{2}(\cos^2\theta - 1)e^{-2i\phi},$$

$$\mathcal{E}^2_0(\alpha) + \mathcal{E}^2_0(\alpha + \pi/2) = \sin^2\theta.$$

$$\mathcal{G} = \begin{pmatrix} \frac{(1+\cos^2\theta)}{8} & -\frac{\sin 2\theta}{8\sqrt{3}}e^{-i\phi} & \frac{1-\cos^2\theta}{8\sqrt{3}}e^{-2i\phi} & 0 \\ * & \frac{(5+3\cos^2\theta)}{24} & 0 & -\frac{1-\cos^2\theta}{8\sqrt{3}}e^{-2i\phi} \\ * & 0 & \frac{(5+3\cos^2\theta)}{24} & -\frac{\sin 2\theta}{8\sqrt{3}}e^{-i\phi} \\ 0 & * & * & \frac{(1+\cos^2\theta)}{8} \end{pmatrix}.$$

The density matrix for the initial state is equivalent to multiplying by a constant:

$$\rho_{\mu\mu} = \begin{pmatrix} \frac{1}{2} & 0 \\ 0 & \frac{1}{2} \end{pmatrix} = \frac{1}{2}\begin{pmatrix} 1 & 0 \\ 0 & 1 \end{pmatrix}.$$

Since we are only interested in the relative sizes of the three components of the signal, the observed intensity can be written in the form

$$I(t) = \frac{1}{2}C\exp(-t/\tau)\ |\langle J = \frac{1}{2} \parallel \mathbf{D} \parallel J = \frac{3}{2}\rangle|^2\ \{I_{\Delta m=0} + I_{\Delta m=1} + I_{\Delta m=2}\}.$$

In order to integrate $\frac{dI}{d\Omega}$ over the detector solid angle ($15° = .26rad$), one must make use of the rotation matrix again to obtain the following relationships between the angles in the two coordinate systems:

$$\cos\theta = -\sin\beta\sin\Theta\sin\Phi + \cos\beta\cos\Theta,$$

$$\sin\theta\cos\phi = \sin\Theta\cos\Phi$$

$$\sin\theta\sin\phi = \cos\beta\sin\Theta\sin\Phi + \sin\beta\cos\Theta$$

In the following calculations implicit use will be made of the fact that integrating an odd function of Φ over 2π equals zero.

The next sections perform the sum over m, m' indicated in eqn. A1.1.1. The calculation can be simplified by using the fact that each of the terms in A1.1.1 is equal to the complex conjugate of the element with m and m' interchanged (*e.g.* $\mathcal{F}_{m,m'} = \mathcal{F}^*_{m',m}$) and the matrices are symmetric about their anti-diagonal. For example,

$$I_{\Delta m=1} = 2[\mathcal{F}_{\frac{3}{2},\frac{1}{2}}\mathcal{G}_{\frac{1}{2},\frac{3}{2}}e^{i\omega_L t} + \mathcal{F}_{\frac{1}{2},\frac{3}{2}}\mathcal{G}_{\frac{3}{2},\frac{1}{2}}e^{-i\omega_L t}]$$
$$= 4Re[\mathcal{F}_{\frac{3}{2},\frac{1}{2}}\mathcal{G}_{\frac{1}{2},\frac{3}{2}}e^{i\omega_L t}].$$

A1.3.1 The $I_{\Delta m=0}$ Component

From the results of the previous sections:

$$I_{\Delta m=0} = \int_{\Theta=0}^{0.26}\int_{\Phi=0}^{2\pi}(0.6882 + 0.04167\cos^2\theta)\sin\Theta d\Theta d\Phi.$$

$$\int_0^{2\pi}\cos^2\theta d\Phi = \int_0^{2\pi}\left\{\sin^2\beta\sin^2\Theta\sin^2\Phi + \cos^2\beta\cos^2\Theta\right\}d\Phi$$
$$= \pi\left\{\sin^2\beta\sin^2\Theta + 2\cos^2\beta\right\}.$$

$$I_{\Delta m=0} = \int_{\Theta=0}^{0.26}(1.3764 + 0.04167(2\cos^2\beta + \sin^2\beta\sin^2\Theta)\sin\Theta d\Theta = \pi(0.0497).$$

A1.3.2 The $I_{\Delta m=1}$ Component

$$I_{\Delta m=1} = \frac{1}{6\sqrt{2}} \int_{\Theta=0}^{0.26} \int_{\Phi=0}^{2\pi} Re\left\{e^{-i\omega_L t}\mathcal{E}_0\mathcal{E}_{-1} \sin\theta\cos\theta e^{i\phi}\right\} \sin\Theta d\Theta d\Phi.$$

$$[\sin\theta\cos\theta e^{i\phi}] = (\sin\theta\cos\phi + i\sin\theta\sin\phi)\cos\theta =$$

$$= (\sin\Theta\cos\Phi + i\cos\beta\sin\Theta\sin\Phi + i\sin\beta\cos\Theta)(-\sin\beta\sin\Theta\sin\Phi + \cos\beta\cos\Theta).$$

$$\int_0^{2\pi} [\,] d\Phi = \pi\left\{i\sin\beta\cos\beta\sin^2\Theta + i\sin 2\beta\cos^2\Theta\right\} -$$

$$= \pi i \sin 2\beta\left\{1/2\sin^2\Theta + \cos^2\Theta\right\} = \frac{\pi i \sin 2\beta}{2}(1 + \cos^2\Theta).$$

$$I_{\Delta m=1} = \frac{\pi\sin 2\beta}{6\sqrt{2}} Re\left\{e^{-i\omega_L t}\mathcal{E}_0\mathcal{E}_{-1} i \int_{\Theta=0}^{0.26} (1+\cos^2\Theta)\sin\Theta d\Theta\right\}$$

$$= \pi(3.282\times 10^{-4}\ \cos\omega_L t) \qquad (0.66\%\ \text{ of }\ I_0).$$

Considering the small change (1.8%) in this cosine term over the length of the decay curve, this corresponds to a 0.004% decrease in the observed lifetime.

A1.3.3 The $I_{\Delta m=2}$ Component

$$I_{\Delta m=2} = \frac{1}{24} Re\left\{e^{-i2\omega_L t}\mathcal{E}_{-1}^2 \int_{\Theta=0}^{0.26}\int_{\Phi=0}^{2\pi} (\cos^2\theta - 1)e^{i2\phi}\sin\Theta d\Theta d\Phi\right\}.$$

$$\int_0^{2\pi} -\sin^2\theta(\cos^2\phi - \sin^2\phi + 2i\cos\phi\sin\phi)d\Phi =$$

$$= \int[-\sin^2\Theta\cos^2\Phi + (\cos\beta\sin\Theta\sin\Phi + \sin\beta\cos\Theta)^2 +$$

$$-2i\sin\Theta\cos\Phi(\cos\beta\sin\Theta\sin\Phi + \sin\beta\cos\Theta)]d\Phi =$$

$$= \pi[-\sin^2\Theta + \cos^2\beta\sin^2\Theta + 2\sin^2\beta\cos^2\Theta]$$

$$= \pi\sin^2\beta[-\sin^2\Theta + 2\cos^2\Theta].$$

$$I_{\Delta m=2} = \frac{\pi \sin^2 \beta}{24} Re \left\{ e^{-i2\omega_L t} \mathcal{E}_{-1}^2 \int_{\Theta=0}^{0.26} [3\cos^2 \Theta - 1] \sin \Theta d\Theta \right\}$$
$$= -\pi(1.2 \times 10^{-6} \cos 2\omega_L t) \qquad (0.002\% \quad \text{of} \quad I_0).$$

This is clearly negligible compared to the I_1 contribution so that the overall effect of the quantum beat is a 0.004% decrease in the observed lifetime.

APPENDIX II

LENS ALIGNMENT PROCEDURE

The following was the procedure used to align the interior and exterior lens systems. The alignment between the interior and exterior systems along the direction of travel (*i.e.* the ion beam direction) can be adjusted by decoupling the external drive screw connecting rod and moving the interior assembly with respect to the now stationary exterior assembly. Note that the decoupling of the external assembly is done by loosening the pair of connecting-rod set screws nearest the stepping motor, not the solitary set screw which is on a flat on the connecting rod.

The alignment of the system in the horizontal plane transverse to the ion-beam path cannot be easily adjusted. There should be no need as it was machined and set up to be as closely aligned as possible.

The following procedure was used to perform the initial interior-exterior alignment and to *check* the transverse alignment (see Fig. A2.1). When the target chamber lid is removed for alignment of the optics, the ion beam path can be defined with the aid of two aluminum blocks which bolt onto the lid. These have 1mm diameter holes drilled to correspond to the position of the ion beam.

1) Remove lenses, filter and PMT.
2) Decouple external drive screw from the drive shaft.
3) Define ion-beam path using a HeNe laser and alignment blocks.
4) Use small flat mirrors to define right angle to beam path (as shown in Fig. A2.1)., sending beam back to source. Remove upper flat mirror
5) Set up centered cross-hairs on inner lens holder and outer cart lens aperture.
6) Position upper assembly (taking up drive screw backlash) so spot is centered on the cross-hairs.

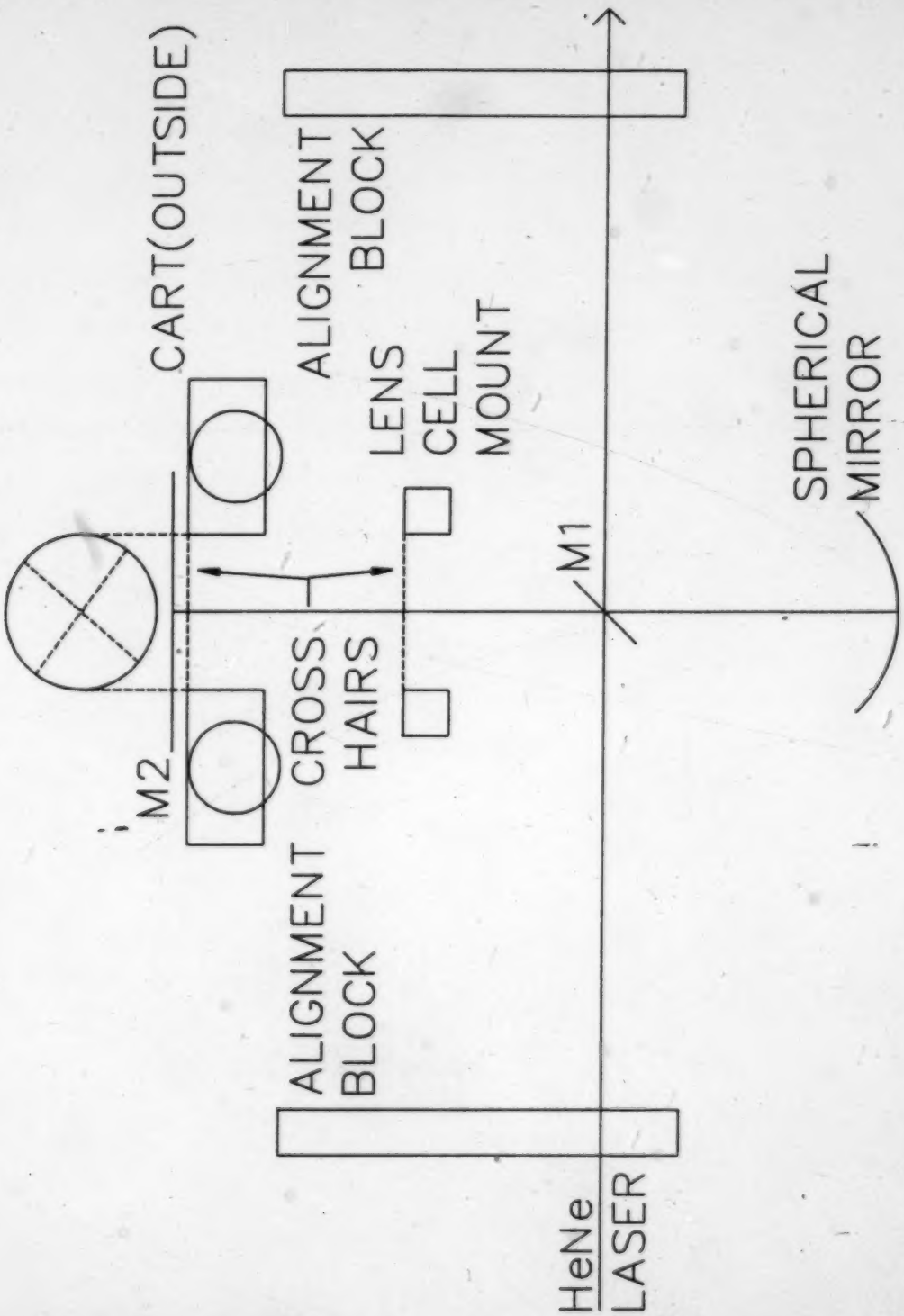

Fig. A2.1 Schematic for alignment of the interior and exterior optical systems.

7) Position lower assembly (again taking up the backlash) so that its cross-hairs are also centered on the laser spot.

8) Carefully, *i.e.* without turning the drive screw, recouple the upper drive by tightening the two set screws.

If the spherical mirror is to be used its alignment can now be adjusted by replacing the lower flat mirror with a thin half-silvered mirror. With the spot lined up on the cross-hairs, adjust the mirror's three screws until the reflected laser spot is centered on the hole in the alignment block.

The observed transverse alignment was tested at various positions along the range of travel of the detection system. There was no obsevable misalignment to better than $\pm 0.5mm$. However, due to the possibility of error in the placement of the cross-hairs, as well as the error in the position of the alignment holes (both about $\pm 0.5mm$), one obtains a total possible uncertainty in the measured alignment of about $\pm 1mm$.

APPENDIX III

ZERO-FIELD QUANTUM BEATS

Quantum beats can affect a decay curve even in the absence of an external magnetic field. This can occur if the homogeneously broadened linewidth of the exciting radiation is greater than the hyperfine splitting between levels. Of the ionic species studied in this thesis, only the sodium atom ($^{23}Na^{+}$) has hyperfine structure and can exhibit zero-field quantum beats. As will be seen in what follows, the hyperfine structure in sodium is much larger than the Zeeman splitting due to the earth's magnetic field so that this external magnetic field can be neglected in the analysis. The hyperfine structure of the sodium level studied in this work has not been measured. An order of magnitude estimate of the hyperfine splitting can be obtained by scaling the values for the corresponding (iso-electronic) neutral neon level.

Table A3.1 Hyperfine structure of $2p$ levels of ^{21}Ne (from [Gi75]).

LEVEL			
Paschen	$j-K$ *coupling*	a (MHz)	b (MHz)
$2p_4$	$3p'[\frac{1}{2}]2$	-309.5 ± 1.1	$+49.1 \pm 0.6$
$2p_5$	$3p'[\frac{3}{2}]1$	-437.0 ± 2.2	$+41.8 \pm 0.6$
$2p_6$	$3p\ [\frac{3}{2}]2$	-185.7 ± 0.8	-68.8 ± 0.6
$2p_7$	$3p\ [\frac{3}{2}]1$	-421.9 ± 1.0	-49.1 ± 0.6
$2p_8$	$3p\ [\frac{5}{2}]2$	-232.2 ± 1.1	-90.0 ± 0.6
$2p_9$	$3p\ [\frac{5}{2}]3$	?	?

Although the hyperfine structure parameter, $a(J)$, for the $2p_9$, $J = 3$ level has not been measured, the values shown in Table A3.1 indicate that a value of about $100MHz$ or greater is to be expected. Scaling this value along the iso-electronic sequence to Na^{+} $a\,\alpha(\mu_I/I)Z_i Z_o^2$ (*e.g.* see [Wo83], Chapter 9), where

$Z_o = 1$ for neutral, *etc.*. and $Z_i = Z - 4$ for p-electrons. The nuclear spins are the same ($I = \frac{3}{2}$) for both ^{21}Ne and ^{23}Na and their magnetic moments are -0.662 and +1.746 nuclear magnetons respectively. Therefore, for the $2p_n$ levels, $a(Na^+) \simeq 10a(Ne) \simeq 1GHz$. The effects (*i.e.* the b values) of the quadrupole moment of the nucleus are small enough that they can be neglected in an order of magnitude calculation and so the hyperfine splitting between levels follows the interval rule:

$$\Delta E(F) - \Delta E(F-1) = aF.$$

Fig. A3.1 shows the hyperfine structure of the $2p_9$ level in Na^+ for the cases where $a = 1GHz$ and $a = 0.2GHz$.

Fig. A3.1 Hyperfine structure of the $2p_9$ level in Na^+ for the cases where $a = 1GHz$ and $a = 0.2GHz$.

F	a=1.0GHz	a=0.2GHz
9/2		
	$4.5GHz$	$0.9GHz$
7/2		
	$3.5GHz$	$0.7GHz$
5/2		
	$2.5GHz$	$0.5GHz$
3/2		

The time resolution along the ion beam needed to observe quantum beats if $a = 1GHz$ is about $0.2ns$ which is about 1/3 the time resolution of the [Na] experiment ($v \sim 1.5mm/ns$). The three-lifetime-long decay curve ($\sim 15ns$) averages out the beats over at least 30 periods, significantly reducing any possible systematic effect on the lifetime. Also, since the interaction region is greater than $2.5ns$ long, the amplitude of any quantum beats will be further reduced. Thus,

since the depth of the modulation is not expected to be larger than about 5% (see below), quantum beats are not expected to have any measurable effect on the observed lifetime.

In order to provide an upper bound on the uncertainty in the measured lifetime caused by the presence of these zero-field quantum beats, a very conservative value of $a = 0.2GHz$ was used in a detailed calculation of the expected decay curve.

Assuming a negligible external magnetic field, the intensity of the decay curve is given by (see [DS78] pp. 656-58):

$$\begin{aligned} I(t,t_o) = G\,|\langle J_e \parallel \mathbf{D} \parallel J_g\rangle|^2 \times |\langle J_e \parallel \mathbf{D} \parallel J_f\rangle|^2 \\ \times \sum_{\substack{k,q \\ F_e,F_e'}} (-1)^{F_e'-F_e+q} E_q^k U_{-q}^k A^k(F_e,F_e') B^k(F_e',F_e) \\ \times \exp[-i\omega(F_e,F_e') - \Gamma](t-t_o). \end{aligned} \tag{A3.1}$$

where $\omega(F_e,F_e') = [E(F_e) - E(F_e')]/\hbar$, and

$$\begin{aligned} A^k(F_e,F_e') = (-1)^{3I+2J_g-J_e-F_e} \times [(2F_e+1)(2F_e'+1)(2J_e+1)(2J_g+1)]^{1/2} \\ \times \begin{Bmatrix} J_e & J_e & k \\ F_e & F_e' & I \end{Bmatrix} \begin{Bmatrix} J_e & J_e & k \\ 1 & 1 & J_g \end{Bmatrix}. \end{aligned} \tag{A3.2}$$

The B^k are the same as the A^k with J_g replaced by J_f; $e \equiv$excited state; $g \equiv$ground state and $f \equiv$final state (final is the same as ground in our case). The E and U are the spherical tensors corresponding to the incident and observed radiation:

$$E_q^k = \sqrt{2k+1} \sum_{\mu,\mu'} \begin{pmatrix} 1 & 1 & k \\ -\mu & -\mu & q \end{pmatrix} \quad \text{with} \quad e_0 = e_z,\ e_{\pm 1} = \mp(e_x \pm i e_y)/\sqrt{2}.$$

The $\hat{\mathbf{e}}$ and $\hat{\mathbf{u}}$ are the unit polarization vectors for the incident and emitted radiation.

The properties of the 6-j symbols[RMBW59] are such that a non-zero result is only obtained for $\mid F_e - F_e' \mid \leq k$. Also the sum over F_e and F_e' can be expressed as twice the real part of the sum over $F_e \geq F_e'$ since for each (F_e, F_e') in eqn. A3.1 one obtains the complex conjugate for (F_e', F_e).

For the sodium experiment both the incident and emitted radiation can be treated as unpolarized light; that is, as the intensity of the emitted light can be calculated by summing the results for two linearly polarized input beams with their polarization vectors at ninety degrees and two linearly polarized emitted beams with polarization vectors at ninety degrees. In the case of linearly polarized light, the only non-zero contribution to eqn. A3.1 comes from

$$E_0^k U_0^k = (2k+1)\begin{pmatrix} 1 & 1 & k \\ 0 & 0 & 0 \end{pmatrix}^2 P_k(\cos\theta), \qquad (A3.3)$$

where θ is the angle between $\hat{\mathbf{e}}$ and $\hat{\mathbf{u}}$. Since the 3-j symbol in eqn. A3.3 is zero for $k = 1$, only $k = 0$ and $k = 2$ need be considered:

$$P_0(\cos\theta) = 1 \quad \text{and} \quad P_2(\cos\theta) = \frac{1}{2}(3\cos^2\theta - 1).$$

For the particular case under consideration $J_g = J_f = 2$ and $J_e = 3$. Absorbing all the constant terms into a single constant C one can write the intensity as

$$I(t,t_0) = C \times Re\Big[\sum_{\substack{k=0,2 \\ F_e \geq F_e'}} (-1)^{F_e - F_e'}(2k+1)\begin{pmatrix} 1 & 1 & k \\ 0 & 0 & 0 \end{pmatrix}^2 P_k(\cos\theta)$$
$$\times [(2F_e+1)(2F_e'+1)] \times \begin{Bmatrix} 3 & 3 & k \\ F_e & F_e' & \frac{3}{2} \end{Bmatrix}^2 \begin{Bmatrix} 3 & 3 & k \\ 1 & 1 & 2 \end{Bmatrix}^2$$
$$\times \exp\left[-i\omega(F_e, F_e') - \Gamma](t - t_o)\right]. \qquad (A3.4)$$

It is convenient to separate the sum into terms with $k = 0$ and $k = 2$. Denoting these two terms by I_0 and I_2 one obtains:

$$I_0 = \sum_{F_e}(-1/\sqrt{3})^2[2F_e+1]^2 \begin{Bmatrix} 3 & 3 & 0 \\ F_e & F_e & \frac{3}{2} \end{Bmatrix}^2 \begin{Bmatrix} 3 & 3 & 0 \\ 1 & 1 & 2 \end{Bmatrix}^2$$

$$= (1/3)\ \ [16]\ \ \{1/28\}\ \ \{1/21\}+$$

$$+ (1/3)\ \ [36]\ \ \{1/42\}\ \ \{1/21\}+$$

$$+ (1/3)\ \ [64]\ \ \{1/56\}\ \ \{1/21\}+$$

$$+ (1/3)\ \ [100]\ \ \{1/70\}\ \ \{1/21\}$$

$$= 4/63.$$

$$I_2 = (3\cos^2\theta - 1) \times 10^{-3}[1.2 - 2.4\cos\omega_{\frac{9}{2}\frac{7}{2}}t - 2.6\cos\omega_{\frac{7}{2}\frac{5}{2}}t - 2\cos\omega_{\frac{5}{2}\frac{3}{2}}t$$

$$+ 0.19\cos\omega_{\frac{9}{2}\frac{5}{2}}t + 0.25\cos\omega_{\frac{7}{2}\frac{3}{2}}t].$$

Scaling the intensity so that the principal component is 100 one obtains for the intensity decay curve

$$I = \{100 + (3\cos^2\theta - 1)[1.8 - 3.7\cos\omega_{\frac{9}{2}\frac{7}{2}}t - 4.1\cos\omega_{\frac{7}{2}\frac{5}{2}}t - 3.2\cos\omega_{\frac{5}{2}\frac{3}{2}}t$$

$$+ 0.3\cos\omega_{\frac{9}{2}\frac{5}{2}}t + 0.4\cos\omega_{\frac{7}{2}\frac{3}{2}}t]\}e^{-t/\tau}.$$

Summing the $(3\cos^2\theta - 1)$ term over all four polarization combinations (*i.e.* θ=0, 90, 90 and 90 degrees) yields a factor of -1/4. Fitting this function (with $\tau = 4.800ns$, $a = 0.2GHz$ and assuming no statistical fluctuations in the data) to a single exponential yields a lifetime of $4.7992ns$, a less than 0.02% deviation. The actual deviation will be less than this since in practice the beats are also averaged out over the slit width and the interaction region and masked by statistical fluctuations. Thus the expected contribution of zero-field quantum beats to the uncertainty in the sodium lifetime must be less than 0.02%.